University of Cape Town

Computational modelling of hydrogel therapies

Author:
Sadman Sakib Ahmed

Student Number:
AHMSAD003

Supervisor:
Prof. M Ngoepe

Co-Supervisor:
Assoc. Prof. WH Ho

Thesis presented for the Degree of

MSc in Engineering specialising in Mechanical Engineering

In the Department of Mechanical Engineering

June 6, 2025

University of Cape Town

The copyright of this thesis vests in the author. No quotation from it or information derived from it is to be published without full acknowledgement of the source. The thesis is to be used for private study or non-commercial research purposes only.

Published by the University of Cape Town (UCT) in terms of the non-exclusive license granted to UCT by the author.

University of Cape Town

Declaration

I, **Sadman Sakib Ahmed**, hereby declare that this thesis is based on my original work except which is properly acknowledged. I know the meaning of plagiarism and declare that all the work in the document, save for that which is properly acknowledged, is my own. This thesis has been submitted to the Turnitin module and I confirm that my supervisor has seen my report and any concerns revealed by such have been resolved with my supervisor. I understand that neither the whole work nor part of has been, is being or will be submitted for another degree. I confirm I have the consent of my supervisor to submit this thesis as any concerns that might arise have been resolved.

I have applied the IEEE referencing style in this thesis. I give the university the right to reproduce the whole or part of this thesis for research.

Signature: Signed by candidate Date: June 6, 2025

Abstract

Myocardial infarctions (heart attacks) are a type of cardiovascular disease that affects a large population of people around the world. In 2019, ischaemic heart disease was the cause of approximately 3 million deaths worldwide. Myocardial infarctions lead to the death of heart tissue, which is eventually replaced by scar tissue in a non-reversible process. Scar tissue does not behave like normal heart tissue (myocardium), and this leads to a decrease in heart function and eventually, heart failure. Current areas of research related to treatment of this disease look at using injectable biomaterials to provide mechanical support to existing scar tissue. This has been shown to improve heart function in different animal models. A popular biomaterial of choice is polyethylene glycol (PEG), chosen for its biocompatibility, biodegradability, and corresponding mechanical properties. PEG undergoes a gelation process, where it changes from a liquid to a gel via a chemical reaction. This is useful as it can be injected during its liquid state and can then solidify into a gel, over a certain period, at a location of interest. Previous in situ studies have noted that the gel that is injected in the myocardium is found in other parts of the body, such as the liver and kidneys. This is undesirable as this may lead to adverse side effects if the gel solidifies elsewhere in the body. The hypothesis for the gel ending elsewhere in the body is that it gets lost during the post-injection state, where it undergoes gelation. This is likely to happen as a result of the pulsating of the heart muscle which "squeezes" the gel out. This research aims to answer the hypothesis by developing a computational framework that investigates the flow behaviour of PEG present in rat myocardium as it undergoes gelation.

A methodology is presented for characterizing the gelation of PEG from existing rheology data. A material model is developed for gelation by using a time-dependent viscosity model that is implemented numerically in Ansys Polyflow. A second methodology is presented for modelling the flow of PEG out of a domain of interest using existing FSI (fluid-structure interaction) results. This methodology utilizes a traction boundary condition, which, when applied to a domain of interest, results in outflows out of all orifices. 2D computational studies are carried out to characterize the impact of applied traction on observed flow rate. The studies are done across the range of viscosities for which the liquid gel exists and explore the use of a time-dependent viscosity. This is done using an idealized, microfluidic geometry that is derived from literature. The results from the 2D study are used to build a 3D model that uses realistic geometry of PEG contained in rat myocardium. 3D computational studies are conducted to explore the aforementioned hypothesis. The observations from the studies show the gel exists at its lowest viscosity for a relatively long period of time, during which it incurs significant losses out of the myocardium. The findings also show that between the rate of loss of

the gel and the rate of viscosity increase, there is a linear relationship in the higher viscosity gradient (i.e. later stages of gelation). This is as opposed to the non-linear relationship between the two parameters in the earlier stages of gelation. The work presented can be used to support the development of PEG for future studies and gives insight into optimizing the procedure for injecting PEG into myocardium. Furthermore, the framework can be used to investigate the flow behaviour of PEG when injected into different parts of the heart.

Acknowledgements

I wish to express my gratitude to the almighty Allah for bestowing upon me the knowledge and ability to undertake and complete this research project. This project was a test of my engineering ability and would not have been possible without the support of many people. I extend my sincere appreciation to both my supervisors, Prof M. Ngoepe and A/Prof W.H. Ho. I am deeply grateful for their guidance, support, and insightful feedback throughout the project. Taking on this project was a challenge, and I appreciate their mentorship and patience at every stage. To Prof. Ngoepe, thank you for providing me with this opportunity. Your expertise in this field was evident throughout the project and I am grateful for the opportunity to learn under your supervision. To Prof. Ho, I wish to express my gratitude for your wisdom throughout the project. You inspired me to aim for the best and perfect my work at every stage.

This multidisciplinary project required me to engage with many talented people in various fields. I am grateful to Benjamin Alheit for his time and insight during our many discussions at CERECAM. I extend my appreciation to Absalom Maluleke for his time and expertise in understanding his FSI model and its application in this project. I am thankful to Dodzi Motchon for his guidance in using the biventricular model in Abaqus. I appreciate the support of Qudus Jimoh-Taiwo and Vincent Punabantu to master Ansys and for addressing my numerous queries. I would like to thank James Dicks for his insights regarding the gelling behaviour of PEG.

I am grateful to all my fellow students and researchers at CERECAM for fostering a pleasant atmosphere in the office. This includes Dr. Grieshaber, Daniel, Emma, Jonathan, Sunday, Tinashe, Abdul, and many others. A special mention goes out to Delta, Emma's charming Swiss Shepherd. I would like to express my appreciation to Denise Botha for always managing all administrative tasks. I extend my gratitude to the University of Cape Town's ICTS High-Performance Computing team for granting me access to their facilities for computational work. A special mention goes out to Timothy Carr for helping me acclimatise to the infrastructure and for his availability whenever I encountered issues.

I am grateful to all my fellow postgraduate friends with whom I undertook this master's journey. It was refreshing to take a break from my work and talk about other interesting research. I would like to specifically acknowledge Saad Naveed, Joshua Malan, Lia Carstens, and Shalom Abiodun. Lastly, I would like to thank my family for their unwavering love and support. I deeply thank my mother for her love and care, and my father for his wisdom and guidance. I appreciate my brother, Shihab Ahmed, for keeping me grounded and reminding me to turn to Allah regardless of my struggles and successes.

Contents

1 Introduction **1**
1.1 Background . . . 1
1.2 Hypothesis, Aims, and Objectives . . . 3
1.2.1 Hypothesis . . . 3
1.2.2 Research Aim . . . 3
1.2.3 Objectives . . . 3
1.3 Scope and Limitations . . . 3
1.3.1 Scope . . . 3
1.3.2 Limitations . . . 4
1.4 Thesis structure . . . 5

2 Literature Review **6**
2.1 Myocardial Infarction . . . 6
2.1.1 Cause . . . 7
2.1.2 Effects . . . 7
2.2 Hydrogels . . . 9
2.2.1 Polyethylene glycol (PEG) . . . 10
2.2.2 Comparison of Newtonian and Non-Newtonian property assumptions . . . 11
2.3 Tissue Engineering Scaffolds . . . 11
2.3.1 Infusion Delivery . . . 12
2.3.2 Intramyocardial injection . . . 13
2.3.3 Material Considerations . . . 14
2.3.4 Biomaterials for scaffolds . . . 14
2.4 Gelation . . . 16
2.4.1 Mechanisms . . . 16
2.4.2 Cross-linking . . . 16
2.5 Existing computational models of non-Newtonian fluids . . . 17
2.5.1 Rheology . . . 17
2.5.2 Computational model of lemon juice gel . . . 19
2.5.3 Computational model of Pluronic F127 in a coaxial extrusion process . . . 21
2.6 Injectable hydrogel treatment . . . 22
2.6.1 Existing cases of treatment . . . 23
2.6.2 Existing computational models . . . 25

3 Methodology **30**
3.1 Governing equations . . . 30
3.1.1 Strong form . . . 32

3.2 Numerical methods . . . 32
3.2.1 Introduction to numerical modelling . . . 32
3.2.2 Overview of the CFD modelling procedure . . . 33
3.3 Computational geometries . . . 34
3.3.1 2D geometry . . . 34
3.3.2 3D geometry . . . 35
3.4 Overview of the ANSYS Polyflow modelling process . . . 37
3.4.1 Boundary Conditions . . . 38
3.5 Rheological behaviour of PEG during gelation . . . 39
3.5.1 Background . . . 39
3.5.2 Rheology . . . 40
3.5.3 Material model . . . 41
3.5.4 Time-dependent viscosity curve fitting . . . 44
3.6 Parametric analysis of a 2D idealised microfluidic geometry . . . 48
3.6.1 Grid independence study (CV-grid-ind) . . . 49
3.6.2 Preliminary analysis using the traction boundary condition . . . 51
3.6.3 Paramteric study on the effect of varying viscosity (Param-visc) 53
3.6.4 Paramteric study on the effect of varying traction (CV-param-trac, CV-lin-ver) . . . 53
3.6.5 Proof of concept simulation (RV-POC-cons) . . . 53
3.7 Application to realistic 3D tissue structure . . . 54
3.7.1 Analysis of relevant FSI results for input into 3D model . . . 56
3.8 Modelling the traction boundary condition . . . 59
3.8.1 Traction boundary condition 1 . . . 59
3.8.2 Traction boundary condition 2 . . . 62
3.8.3 Traction boundary condition 3 . . . 63
3.8.4 Scaling procedure . . . 65
3.9 Analysis of a 3D microstructural domain . . . 67
3.9.1 Grid independence study (3D-grid-ind) . . . 69
3.9.2 Validation of microfluidic domain (3D-domn-vald) . . . 73
3.9.3 Parametric studies . . . 73
3.9.4 Time step independence (Gel-timstp-ind) . . . 74
3.10 Case Studies . . . 76
3.10.1 Flow behaviour of PEG during gelation (Gel-full-model) . . . 76
3.10.2 Flow behaviour of PEG in a simpler geometry (Gel-simple-model) . . . 76

4 Results and Discussion **77**
4.1 Results of the analysis of the 2D microfluidic geometry . . . 77
4.1.1 Grid independence study results . . . 77
4.1.2 Traction BC preliminary analysis results . . . 81

4.1.3 Varying viscosity parametric study results 83
4.1.4 Varying traction parametric study results 84
4.1.5 Proof of concept simulation results 85
4.2 Results of the analysis of the 3D microfluidic geometry 86
4.2.1 Grid independence study 86
4.2.2 Domain validation results 88
4.2.3 Parametric study results 90
4.2.4 Timestep independence study 93
4.3 Case Study results 95
4.3.1 Gelling results for all BCs 95
4.3.2 Gelling results for a simple 3D geometry 100

5 Conclusion and Recommendations 103
5.1 PEG gelling behaviour within the myocardium 103
5.2 Gel development and administration methods 104
5.3 Future modelling recommendations 104

References 106

Appendices 114

A Methodology for using viable periodic functions to generate results for unusable periodic functions 115

B Supporting calculations for proof of concept simulation 118

C Gelation done in Fluent 121

D Further comparison of solutions computed in Polyflow and Fluent (RV-POC-ramp, RV-POC-per) 122

E Traction BC functions 126
E.1 Traction BC1 126
E.2 Traction BC2 126
E.3 Traction BC3 127

F Traction boundary condition curve fitting 129
F.1 Traction BC1 129
F.2 Traction BC2 130
F.3 Traction BC3 131

G Supplementary Analysis using the Grid Convergence Index 132

G.1 Grid Independence Study 132
G.2 Time Step Independence Study 133

H Validation studies 135
H.1 Investigation of the fluid domain during the cardiac cycle (3D-card-cycl) 135
H.2 Rigid CFD results 138
H.3 Constant viscosity assumption (Gel-const-visc) 140
H.4 Constant viscosity assumption results 141
H.5 Strategy for simulating a large time domain (Gel-splt-domn) 143
H.6 Supporting results for simulating a large time domain 144
H.7 Solver convergence over multiple cycles during gelation (Gel-solv-convg, 3D-solv-convg) 145
H.8 Solver convergence for gelation results 145

I Solver performance (Gel-solve-perfm) 147

J Instability in BC3 flow rate solution 149

K Simplified 3D geometry 150

L Curve fitting for the volume lost per cycle behaviour 152

List of Figures

1 An illustration of the heart showing how an artery can be blocked by different substances. . . . 6
2 An illustration of the heart showing how scar tissue is formed and the extent to which the heart tissue is damaged. . . . 8
3 Various graphs that show the duration of each process during the healing process. . . . 9
4 Plots of stress against shear rate for a type of hydrogel. . . . 10
5 Molecular structure of PEG 11
6 An illustration to highlight the different infusion delivery modes as well as the intramyocardial injection method. . . . 12
7 An illustration to show the two delivery methods. . . . 13
8 Reaction of PEG tetra-thiol with different types of PEG. . . . 17
9 A rheometer and the operating principles of each type of rheometer. . 18
10 Different geometries for testing fluids/solids, arranged in order based on the viscosity of the fluid being measured. . . . 19
11 A plot of the data obtained from a typical stress/strain sweep which shows how the linear viscoelastic region is determined. . . . 20
12 A stress-strain plot highlighting how a Herschel-Bulkley fluid varies based on the flow behaviour index. . . . 22
13 Scar thickness in rabbit myocardium injected with saline and hydrogel. 23
14 Echocardiogram showing the difference in LV shape between a treated and untreated sheep heart. . . . 24
15 Graphical representation of diastolic and systolic volumes and the ejection fraction in pig hearts. . . . 25
16 Fibre stress distribution between a treated and untreated left ventricle during diastole and systole. . . . 26
17 A 3D mesh of the heart which shows the hydrogel layered in between the infarct tissue on the left 27
18 Biventricular geometry of a rat heart developed from micro-CT imaging showing the dispersion of gel within the infarcted tissue. . . . 28
19 Confocal microscopy image of left ventricular tissue 29
20 Illustration of the 2D microfluidic domain. . . . 34
21 Confocal microscopy image of left ventricular tissue and reconstructed geometry in Simpleware. . . . 35
22 Region of interest before post-processing (left). Region of interest after post-processing (right). . . . 36
23 Visualization of the 3D fluid domain (top left), the outer surface (top right), the two outlets along the z-axis (bottom left), and the two outlets along the x-axis (bottom right). . . . 36

24 Plot showing the cross-over between loss and storage moduli as well as the variation of complex viscosity over time as gelation occurs. . . 41
25 Plot showing the variation of phase angle against time while the fluid is in the liquid phase. 42
26 Plot showing the recoverable shear against time while the mixture is in the liquid phase. 44
27 Plot showing the variation of viscosity against time for all experimental runs. 45
28 Plot showing the comparison of the 6th order polynomial against all experimental runs 46
29 Plot showing the comparison of the exponential fit against all experimental runs 47
30 Illustration of the refined edge mesh. 50
31 Plots of periodic traction functions over time. 52
32 Illustration of myocardial tissue squeezing gel out of its interstitial spaces. 54
33 Plot of recoverable shear over time for multiple experimental runs. . . 55
34 Velocity contours of the fluid domain showing the difference in the flow field between the FSI simulation (right) and the Polyflow model (left). 56
35 Meshes for the solid and fluid domain used for the FSI simulation . . 57
36 Plot of strain over time for the tissue block during the FSI simulation 57
37 Plots of flow rate and strain over time for multiple cardiac cycles. The flow rate is scaled for visualisation purposes. 58
38 Mesh of the biventricular model analysed with the gel shown in red. . 59
39 Meshes of the gel in the biventricular model showing the regions (in red) analysed at the top and bottom. 60
40 Plot of stress over time for both regions described in figure 39. 60
41 Normal stress vectors for the tissue block in a specific direction showing the variability in the stress vectors. 61
42 Plots of volumetric flow rate comparing the FSI result to the result obtained by using traction BC1. 62
43 Plots of volumetric flow rate comparing the FSI result to the result obtained by using traction BC2. 63
44 Visual comparison of the strain during the last cycle with its absolute gradient. The original FSI result is also included. 64
45 Plots of volumetric flow rate comparing the FSI result to the result obtained by using traction BC3. 64
46 Plot of traction over time with the scaled flow rate response and ratio of the two parameters during the simulation. 66

47 Velocity contours for all outlets of the fluid domain. The top row shows contours for $Z_{positive}$ and $Z_{negative}$ respectively. The bottom row shows contours for $X_{positive}$ and $X_{negative}$ respectively. 70
48 Mesh of the fluid domain without any mesh refinement. 71
49 Point cloud created over the relevant face used for the grid independence analysis. 71
50 Mesh of the fluid domain highlighting the regions chosen for mesh refinement. 72
51 Mesh of the fluid region with mesh refinement. 73
52 Plot of viscosity over time for the gelling material model used. 75
53 Velocity contour of the simulation where normal traction is applied to a fluid domain. In this instance, the shear velocity at the boundary is set to 0. The velocity observed at the wall (right) is perpendicular to the surface. 78
54 Velocity profiles for different meshes without special refinement. . . . 78
55 Percentage differences between different meshes as you move further away from the axis of symmetry. It is important to highlight the large difference observed closer to the edge. 79
56 Velocity profiles for different meshes with the outlets refined. 80
57 Percentage differences between different meshes as you move further away from the axis of symmetry. 80
58 Velocity contour plots due to using different traction BCs. The top contour is for the case where the shear velocity is set to 0 m/s. The bottom contour is for the case where the shear traction is set to 0 Pa. 81
59 Plot of average velocity over time as a constant traction is applied on the boundary with a gelling material. 82
60 Plots of average velocity over time for different periodic tractions applied with a gelling material. 83
61 Plot of average velocity against viscosity for the same traction applied which shows an inverse relationship. 83
62 Plot of average velocity against normal traction. 84
63 Plot of average velocity against time with the traction function scaled for visualisation purposes. The ratio between the two parameters is also plotted to show a perfectly linear relationship. 84
64 Plot of average pressure against time for a gelling material for analytical and numerical solutions. 85
65 Relative differences between the analytical solution and each numerical solution. 86
66 Relative differences between velocity results extrapolated on the point cloud. This is between two meshes that do not have outlet refinement. 87

67 Relative differences between velocity results extrapolated on the point cloud. This is between two meshes that have outlet refinement. 88
68 Velocity contours showing the lines (in black) along the faces where the velocity results are extrapolated. 89
69 Plot of velocity along all lines described in Figure 68 above. 89
70 Plot of observed flow rate against viscosity set for a constant traction applied. 90
71 Plots of observed flow rate against applied traction for different viscosities. 91
72 Plot of traction variation gradient against viscosity used. 91
73 Shear rate contour of the fluid domain showing the variation in shear rate at an outlet. 92
74 Plot of flow rates obtained using BC1 with increasing time step refinement. The number of time steps required for each solution is also noted. 93
75 Plot of flow rates obtained using BC2 with increasing time step refinement. The number of time steps required for each solution is also noted. 94
76 Plot of flow rates obtained using BC3 with increasing time step refinement. The number of time steps required for each solution is also noted. 94
77 Plots of volumetric flow rate over time for BC1 and BC2 during the latter stages of gelation. 95
78 Plot of volume lost per cycle overlayed with the viscosity change over time using all BCs. 96
79 Plot of loss as a percentage of the domain volume over time using the BC1 solution. 98
80 Plot of volume loss per cycle and viscosity over time. 98
81 Plots of the viscosity gradient and the volume loss gradient per cycle over time. 99
82 Plot of volume loss gradient against viscosity gradient showing the time at which the maximum occurs. 100
83 Plot of volume lost per cycle and viscosity change over time using BC1 and the simple geometry. 101
84 Plot of viscosity gradient and the volume loss gradient per cycle over time for the simpler geometry. 101
85 Plot of volume loss gradient against viscosity gradient for both geometries. The times at which the maximum occurs for both are also highlighted. 102

86 Plots of average velocity with an overlay of the ratio between the two periodic functions that were used to generate the results. 115
87 Plots of average velocity comparing the original solution and the scaled solution. 116
88 Plot of a scaled average velocity result for a periodic function that causes solver instability. Includes an overlay of the periodic function. 117
89 The line at which the average pressure is calculated. It can be seen that the flow is fully developed at this point. 119
90 Plot of average pressure between the inlet and outlet, calculated in Polyflow. 120
91 Plot of average pressure against time for a gelling material for analytical and numerical solutions. Here the velocity is increased linearly. 123
92 Relative differences between the analytical solution and each numerical solution. Here the inlet velocity increases linearly. 123
93 Plot of average pressure against time for a gelling material for analytical and numerical solutions. Here the velocity is varied periodically.125
94 Relative differences between the analytical solution and each numerical solution. Here the inlet velocity varies periodically. 125
95 Curve fitting for traction BC1. 129
96 Curve fitting for traction BC2. 130
97 Curve fitting for traction BC3. 131
98 Visual comparison of the flow rate of PEG with the strain response of the tissue block. The flow rate response is scaled for visual purposes.135
99 Visualization of the changing shape of the fluid domain during the cardiac cycle. The changes can be noticed easily in two locations. The left-most outlets can be seen to change orientation. The center outlet in the front-facing outlets can be seen to change shape. 136
100 Plot of flow rate over time using traction BC2 with the distinctive peak highlighted. The area under this peak is used as the measure for the analysis. 141
101 Plot of flow rate against time for a solution that is run using one solver and for another solution that is run using two solvers. 144
102 Plot of flow rates over time for all three studies conducted. The constant viscosity study results are shifted in the x-axis to visually compare the different results. 146
103 Plot of volumetric flow rate against time using BC3. Each cardiac cycle is highlighted in a different colour. 149
104 Simple 3D microstructural domain developed for the second case study.150
105 Final mesh of the simple geometry showing the finely refined outlets. 151
106 Curve fitting for the volume lost per cycle behaviour. 152

List of Tables

1 Summary of parameters that can be calculated based on the measured parameters from using a Rheometer. 18
2 Comparison between the 6th-order polynomial and the experimental runs 45
3 Comparison between the exponential fit and the experimental runs . 47
4 Summary of all 2D computational studies done. 48
5 Time step paramters for all 2D transient studies. 49
6 Preliminary mesh information. 50
7 Refined mesh information. 50
8 Volume lost per cycle in the FSI simulation. 58
9 Summary of all 3D computational studies done using different viscosities 67
10 Summary of all 3D computational studies done using the gelation model developed. 68
11 Preliminary mesh refinement information. 70
12 Subsequent mesh refinement 72
13 Timestep settings for all simulations 75
14 Flow rate results for each mesh with their relative differences calculated with respect to the solution obtained using the 2,200 $\times 10^3$ element mesh. 87
15 Flow rate results for each mesh with their relative differences calculated with respect to the solution obtained using the 2,000 $\times 10^3$ element mesh. 87
16 Run times for each boundary condition with increasing time step refinement. 93
17 Volume lost in each region of the viscosity change for all solutions. . . 97
18 Simulation Parameters for the study that validates a time-dependent viscosity model for a velocity that is increased linearly. 122
19 Simulation Parameters for the study that validates a time-dependent viscosity for a velocity that is varied periodically. 124
20 Timestep settings for periodic velocity for both solvers for both cases 124
21 Grid independence study results taken from Table 15. 133
22 Time step independence results for traction BC1 taken from Section 4.2.4. 133
23 Respective areas of all relevant boundaries during the cardiac cycle. The areas are in mm^2. The relevant parameters for the final mesh used in this project are also included for further discussion. 137
24 Relative percentage differences of the areas when compared with the areas taken at diastole. 137

25 Flow rate and average velocity results during the cardiac cycle (final mesh included for further discussion). 139
26 Relative differences between average velocity and flow rate when compared with the values taken at diastole. 139
27 Results of the analysis which shows the time domains simulated, the area under the distinctive peak representing volume, and the relative difference between the volumes when compared to the first cycle. . . . 142
28 Similar results to Table 27 with different regions analysed. Here, the relative differences are calculated with respect to the volume obtained from 190-191 s. 142
29 Simulation Parameters for the study that investigates solver performance. 147
30 Run times using a workstation with increasing number of cores used for the setup. 148
31 Run times using the HPC with increasing number of cores used for the setup. 148
32 Run times using the HPC with increasingly refined meshes with a 4-core setup. 148

Nomenclature

Anterior wall	Refers to the front-facing surface of the left and right ventricles.
Cardiogenic shock	A condition in which your heart suddenly cannot pump enough blood to meet your body's needs.
Cardiomyocyte	The cell responsible for the contraction of the heart.
CFD	Computational Fluid Dynamics
FEA	Finite Element Analysis
Femoral	Refers to the femur, which is the thigh bone, and structures that are associated with or located in the thigh region.
Fibrinogen	A protein found in the blood which is a crucial component of blood-clotting.
Hydrophilic	Capable of interacting with water through hydrogen bonding.
In silico	Experiments conducted using a computer simulation software.
In situ	Situated in the original place.
In vitro	Experiments conducted using biological materials that have been isolated from their usual biological surroundings.
In vivo	Experiments conducted on a living organism.
Ischemia	A condition in which blood flow (and thus oxygen) is restricted or reduced in a part of the body.
Ischemic zone	Inadequate blood supply (circulation) to a local area due to blockage of the blood vessels supplying the area.
MINOCA	A heart attack in which no blockages are seen in the main coronary arteries. MINOCA stands for myocardial infarction with non-obstructive coronary arteries.
Myocardium	The muscular layer of the heart.
Myofibroblast	An activated form of fibroblast that is capable of contraction due to the presence of cytoskeletal proteins that are normally found in smooth-muscle cells. These cells participate in wound repair by contracting the edges of the wound.

Necrosis	The death of body tissue.
NHS	National Health Service
NSTEMI	A heart attack where a coronary artery is narrowed enough to greatly reduce blood flow but is not totally blocked.
PCI	A non-surgical procedure which uses a catheter to place a stent in a blood vessel.
Proximal	Refers to a location that is situated close to a point of reference.
Sarcomere length	This is a unit of measurement that defines the length of a muscle fiber from one end to the other.
Scar tissue	A collection of cells and collagen that covers the site of the injury.
STEMI	A heart attack where a coronary artery is completely blocked.
Systole	This is when the heart muscle contracts. When the heart contracts, it pushes the blood out of the heart and into the large blood vessels of the circulatory system.
Thrombin	An enzyme that plays an important role during blood clotting.

1 Introduction

This chapter provides background information on heart attacks and the impact they have globally and locally in South Africa. It then considers the current developments in regenerative medicine to mitigate the effects of heart attacks. This provides the basis for the computational modelling work that is being done in this area of research. Finally, the chapter looks at the aims and objectives laid out, outlines the scope, and discusses the limitations.

1.1 Background

A myocardial infarction (MI), commonly known as a heart attack, is a condition in which blood flow is restricted to a part of the heart. Restrictions usually occur due to a blockage in the vessels of the heart caused by a build-up of substances such as plaque or blood clots [1]. This deprives the heart muscles of oxygen, causing damage that often leads to tissue death. The tissue, also known as myocardium, has a limited ability to regenerate. As it is not metabolically active, scar tissue replaces it once it dies [2]. Scar tissue is incompatible with the original tissue, inducing additional stress on the heart's ability to function normally. This continued stress leads to dysfunctions in the heart, which eventually result in heart failure and death [2].

According to a report by the World Heart Federation [3], cardiovascular diseases accounted for **a third** of global deaths in 2021. A similar trend was observed in 2019, with one third of **9.1 million** deaths attributed to ischaemic heart disease [3]. Stroke resulted in 6.6 million deaths, and these two conditions account for 85% of all cardiovascular deaths [3]. The health data for South Africa, captured by the World Health Organisation in 2021 [4], reported that per 100,000 deaths:

- 59.6 deaths are due to ischaemic heart disease, making it the seventh leading cause of death in men.
- 37.3 deaths are due to the same reason, making it the seventh leading cause of death in women.

For a population of approximately 61,500,000 in 2021, this corresponds to an estimated **30,000** deaths in that year due to ischaemic heart disease [4]. These statistics show the impact of heart attacks around the world and in South Africa; therefore, it is increasingly important to develop treatments and mitigate the effects of the disease. In developing countries, including South Africa, young individuals are affected by heart attacks, resulting in significant socioeconomic impact.

Current interventions for myocardial infarctions primarily extend the time to heart

failure. Current treatment / management of patients can be described in the following way [5]: based on the classification of myocardial infarction, reperfusion therapy is administered to restore perfusion through blocked arteries. The effectiveness depends on the speed with which the patient is admitted. Subsequently, a percutaneous coronary intervention (PCI) is performed, which involves placing a stent in the occluded vessel. Patients are also treated with antiplatelet agents that inhibit the formation of blood clots. In cases of advanced heart failure, left ventricular assist devices are used to provide mechanical support to the heart, facilitating blood circulation throughout the body. Ultimately, no treatment allows the recovery of dead heart tissue, and a patient is required to be under constant supervision.

This highlights the significance of regenerative medicine and its potential for treating MI. Stem cell therapy can treat the affected tissue by placing stem cells in the injured region of the heart. There are different ways to access the injured part, and this is covered in the next chapter. One specific type of therapy uses a tissue engineering scaffold injected with stem cells. This helps by suspending stem cells close to the site of injury without significant loss due to the vigorous action of the heart. Moreover, injectable scaffolds alone have been shown to support the healing process after infarction [6] and improve cardiac function [7]. This treatment is of particular interest in the context of this project.

The biomaterial of interest for the scaffold is a hydrogel known as polyethylene glycol (PEG). It can be customised for a specific purpose and is biocompatible, making it attractive for MI therapy. The hydrogel is prepared in solution and combined with a cross-linker. This mixture is then injected into the myocardium and undergoes gelation over time in situ. Investigating this therapy involves using animal models to understand the mechanisms that govern PEG distribution and retention within the myocardium [8]. The treatment has also been tested in humans with other biomaterials and has shown positive results [9].

To better understand the effect of PEG within the myocardium, computational models have been developed. Most of these models examine the biomaterial in either its gelled or liquid state. However, none investigate the phase transition from liquid to gel. In situ studies exploring the therapy have indicated that the gel is present in other regions of the body ([10], [11]). This observation substantiates the occurrence of losses during therapy. It has been hypothesised that the greatest losses occur while the biomaterial is in its liquid phase; therefore, there is a keen interest to further understand the mechanisms of loss.

1.2 Hypothesis, Aims, and Objectives

1.2.1 Hypothesis

It is hypothesised that the most significant losses of PEG occur during the gelation phase following its injection.

1.2.2 Research Aim

This project aims to model the behaviour of PEG present in myocardial tissue as it undergoes a phase change due to gelation. The model will answer the hypothesis and quantify the losses, if any.

1.2.3 Objectives

The primary objectives of this project are as follows.

- Review literature on the effect of myocardial infarctions on the myocardium, PEG rheology, tissue engineering scaffolds, gelation, and existing computational models of non-Newtonian fluids and PEG in the myocardium.
- Use available rheology data for PEG to characterise the fluid properties of degradable PEG. The data focus on the changes that occur during the gelation process. This is used to build a material model for PEG to be used in silico as it undergoes gelation.
- Simulate the flow of PEG in microfluidic channel geometries.
- Implement a computational framework using CAD data from reconstructed myocardial tissue. This framework will be used to explore the hypothesis mentioned above. The results of idealised models will also be presented.

1.3 Scope and Limitations

1.3.1 Scope

The overall scope of the project is to develop a FEM model that simulates the gelation of the hydrogel within the myocardium as it undergoes the vigorous motion of the heart. The boundary conditions prescribed and the established fluid behaviour can be used to perform numerical simulations on any commercial FEM/CFD software packages that can solve for laminar flow. It should be emphasised that ANSYS Polyflow (ANSYS, Pennsylvania, USA) is used because it has a specialised fluid flow solver that focusses on polymer flows. It is a FEM-based CFD solver.

ANSYS Meshing (ANSYS, Pennsylvania, USA) and Simpleware ScanIP (Synopsys, Mountain View, USA) are used for any finite element meshing required, ANSYS Polyflow is used as the numerical solver for all FEM simulations, and ANSYS CFD-Post (ANSYS, Pennsylvania, USA) is used for all post-processing. The product versions for all of these are **2024 R2**. Python 3.9 is used for all the data processing required. CAD data of myocardial tissue is acquired using confocal microscopy images, which are reconstructed in Simpleware ScanIP [12]. The data used in this project is derived from the existing literature and a thesis previously conducted that investigated the gelation of various types of hydrogels [13].

1.3.2 Limitations

The existing literature on PEG indicates that it can differ between a Newtonian or non-Newtonian material model depending on the shear rates it experiences. Furthermore, the behaviour can also vary depending on the scale, and PEG shows non-Newtonian behaviour on the microscale [12]. The gelation data of PEG show that the dynamic viscosity changes over time at the same shear rate. However, there is a lack of gelation data for PEG, particularly across varying shear rates. One may require gelation data for PEG over various shear rates to model it as a non-Newtonian fluid with time-dependent viscosity. Due to the absence of extensive gelation data at different shear rates in literature, PEG was simplified to a Newtonian fluid with a time-dependent viscosity. This approach adequately represents the viscosity variations occurring during the gelation phase. The existing literature also highlights the impact of temperature on viscosity; however, additional data is necessary to incorporate this variable into a simulation. Therefore, the full model is simplified to an isothermal model. Further discussion of this behaviour of PEG is provided in Section 2.2.1.

The computational model used is a rigid CFD model developed in Polyflow. It uses a traction boundary condition to simulate the contraction of the heart muscles that causes outflow. This was done to replicate the results of an FSI model that investigates the displacement of biomaterial due to ventricular motion. Polyflow has limited FSI modelling capabilities and cannot model complex material models needed to model the myocardium. However, it can model time-dependent viscosity and capture complex fluid behaviour to a high degree of accuracy, which is of importance in this project.

The data for PEG used is not the original form used in intramyocardial injections where it is mixed with stem cells. Instead, it is a modified form of PEG that is used with a cross-linker to produce a degradable gel. The motivation for this comes from a requirement discussed in Section 2.3.2. The modelling is done at the scale of a mouse/rat because initial optimisation studies are performed in animals before being

trialled in humans. Ultimately, the therapy is being developed for use in humans.

1.4 Thesis structure

The remainder of the thesis is structured as follows. Chapter 2 reviews the existing literature on heart attacks, hydrogels, tissue engineering scaffolds, gelation, and existing computational models of non-Newtonian fluids and PEG in the myocardium. Subsequently, Chapter 3 addresses the methodology applied to address the research question. This includes characterising the behaviour of PEG and establishing the full setup of the numerical model. Chapter 4 presents the results obtained from the grid independence studies, parametric studies, method verification, and the final results of the full model. Finally, conclusions and recommendations are provided in Chapter 5.

2 Literature Review

This chapter begins by introducing heart attacks, what causes them, and the physiological changes that follow. After that, hydrogels are discussed, looking at their uses and physical behaviour. PEG is introduced and its fluid behaviour is mentioned. Afterward, tissue engineering scaffolds are reviewed, looking at the delivery methods used to transport them, material considerations, and available materials. A discussion of gelation looks at the types of gelation and the mechanism of interest. The chapter then introduces rheometers and explores existing computational models of non-Newtonian fluids. Finally, the chapter ends with a discussion of the injectable hydrogel treatment explored in this project. The discussion looks at existing treatment cases and the attempts made to model them computationally.

2.1 Myocardial Infarction

Myocardial infarction is the medical term for a heart attack, which is a non-infectious disease. These occur due to a blockage of blood flow to the heart muscles [1]. The obstruction inhibits the flow of oxygen and nutrients to muscle tissues, which can lead to damage or death of the tissues [2]. This obstruction can be visualised below in Figure 1.

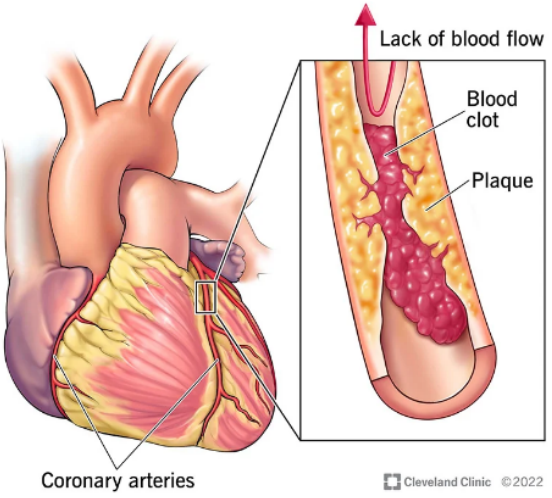

Figure 1: An illustration of the heart showing how an artery can be blocked by different substances [1].

There are different types of heart attacks. STEMI (ST segment elevation myocardial infarction) describes a heart attack in which the coronary artery is completely blocked. NSTEMI (Non-ST segment elevation myocardial infarction) occurs when the artery narrows enough to reduce blood flow. MINOCA (Myocardial infarction

without obstruction of the coronary arteries) is an attack in which there are no blockages in the main coronary arteries [14].

2.1.1 Cause

Harrison's Principles of Internal Medicine [15] mentions that coronary artery disease (CAD) is the predominant cause of heart failure. Heart failure patients [HF] can be broadly categorised into two groups: HF with reduced ejection fraction [EF] and HF with preserved EF [15]. CAD is a condition where fatty substances build up in the coronary arteries. This build-up can lead to a myocardial infarction. It should be emphasised that myocardial infarctions can lead to HF with a preserved and reduced ejection fraction. It is important to note that in Africa, the main causes of HF are non-ischemic [16].

Several factors put one at risk for an attack. Factors such as age and family history are uncontrollable factors. Ageing of the vasculature results in increased arterial thickening and stiffening [17]. North et al. [17] also mention changes in the heart, which cause it to become less efficient with age. A cohort study by Ranthe et al. [18] showed unequivocally that the more heart attacks family members have experienced and the closer the degree of kinship, the greater the individual's risk of an attack.

There are other risk factors that a person can control. The NHS [19] mentions some of these factors, such as smoking, lack of exercise, high cholesterol, and high blood pressure. The chemicals in cigarette smoke cause the cells that line the blood vessels to become swollen and inflamed [20]. It also causes the blood to thicken and form clots [20]. In certain cases, inactivity may lead to the accumulation of fatty materials in the arteries, leading to a heart attack [21]. High cholesterol, often due to poor diets and chronic diseases, may lead to a build-up of fatty materials. High blood pressure damages the arteries by making them less elastic [22], which has a similar effect to that caused by ageing [23].

2.1.2 Effects

Ischemia of the heart tissue leads to necrosis of the cardiomyocytes. Ischemia describes a condition in which blood flow reduces in a part of the body. Necrosis describes the death of tissue. For human adults, the myocardium has a limited ability to regenerate [2]. The dead myocardium does not remain metabolically active and is replaced by scar tissue. This is known as ventricular remodelling and takes place over 2-3 weeks. This scar tissue does not have the same function as the native myocardium. It cannot contract rhythmically and is not an efficient conductor of electrical signals [2]. This causes the heart to work harder to fulfil its role, thereby placing significant stress on it. These alterations lead to left ventricular (LV) dys-

function, potentially progressing to heart failure and death [2]. Scar tissue can be visualised below in Figure 2.

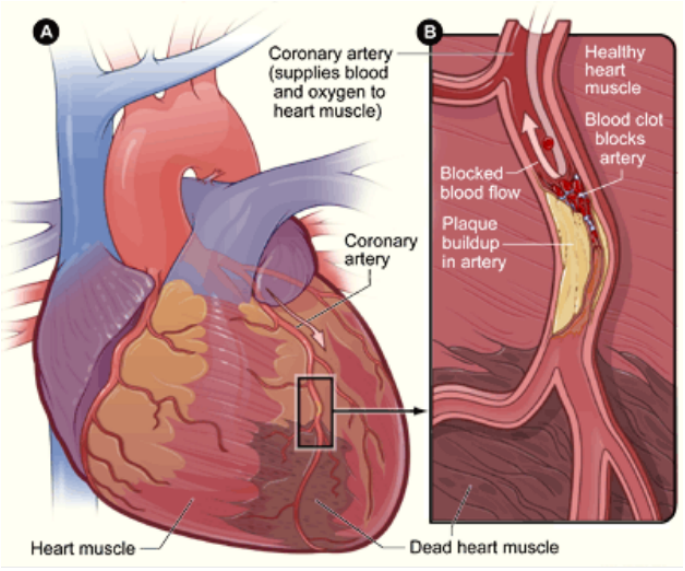

Figure 2: An illustration of the heart showing how scar tissue is formed and the extent to which the heart tissue is damaged [24].

The change from dead myocardium to scar tissue can be described in three steps [25]:

2.1.2.1 Inflammatory phase

Within hours of injury, a variety of inflammatory cells invade the ischemic zone. This phase occurs during the first week of healing. Cells such as neutrophils, macrophages, and lymphocytes play a central role in the healing process. The biological processes that take place during this stage are not relevant for the discussion here but allow for the transition into the next phase.

2.1.2.2 Fibrotic phase

The fibrotic phase typically lasts several weeks and is categorised by the behaviour of myofibroblasts. These are the most abundant cell types in the heart, and their concentration increases in the infarct area. Entering from the surrounding tissue, they help repair the heart but also cause scarring. There is an increase in collagen content and matricellular proteins and this helps to form scar tissue.

2.1.2.3 Remodelling phase

The remodelling phase lasts for months as the collagen content stabilises. Scar tissue matures due to collagen cross-linking. Figure 3 below describes the three phases and their durations.

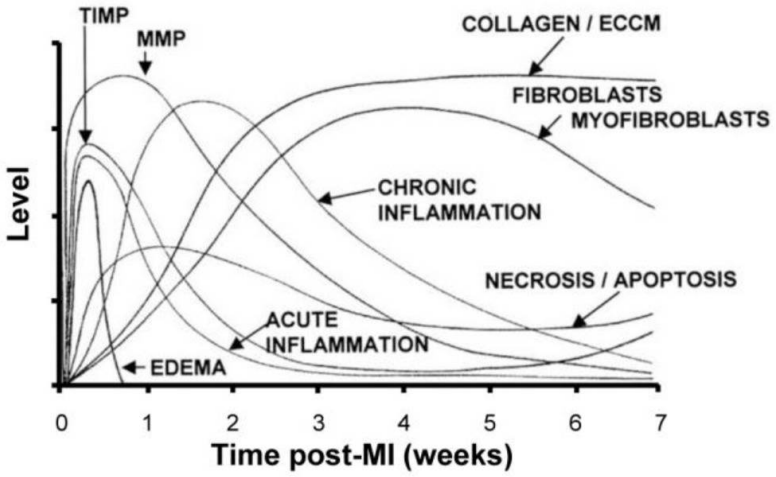

Figure 3: Various graphs that show the duration of each process during the healing process. The acute inflammation graph illustrates the inflammatory phase. The myofibroblast graph illustrates the fibrotic phase. The collagen graph illustrates the remodelling phase [25].

There are different mechanical implications of scar tissue, and the relevant ones are discussed. The size, geometry, and location of scar tissue affect healing tissues and their interaction with existing tissue. For example, during systole, scar tissue stretches and bulges outward, reducing the efficiency of the heart. The larger the scar tissue, the higher the risk of cardiogenic shock [26]. Cardiogenic shock occurs when the heart suddenly cannot pump enough blood to meet the body's requirements. Another example involves the location where scar tissue may develop in the anterior wall of the left ventricle, which affects functionality and may increase the chance of heart failure [27].

2.2 Hydrogels

Hydrogels are polymeric materials that hold large amounts of water in their structure. This is because their polymer chains are hydrophilic, and they can associate with large quantities of water without dissolving [28]. This property makes them biocompatible, allowing their use in different medical settings. They have been

adopted for use as catheter coatings, wound dressings, and drug delivery. More recently, there has been an effort to use them for tissue engineering scaffolds, which are discussed later.

The large fraction of water in the hydrogel structure results in mechanical characteristics that differ from those of classic engineering materials. Hydrogels possess a relatively low elastic modulus (10 Pa to 100 kPa) [29] and exhibit non-Newtonian behaviour [30]. Non-Newtonian behaviour can be briefly explained as a material that does not follow the linear relationship between stress and strain. This complicates understanding the mechanical behaviour of hydrogels. Figure 4 below shows how the stress response varies for a typical hydrogel with increasing shear rate.

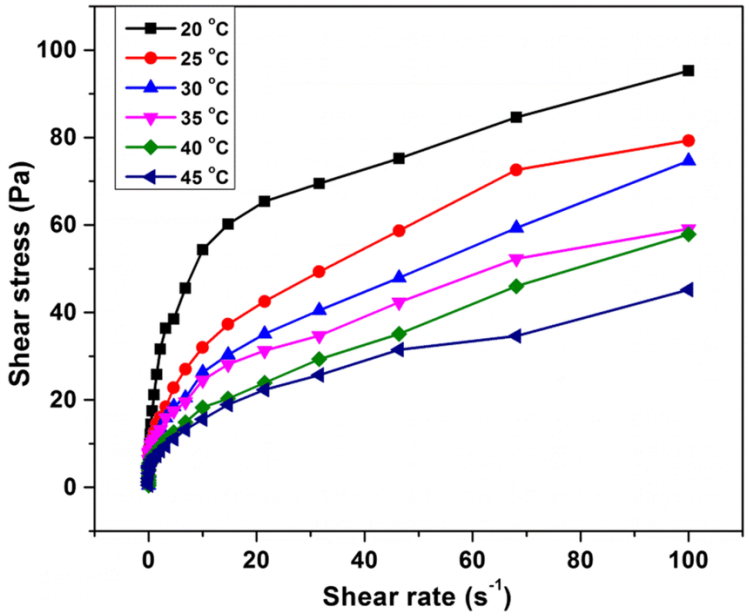

Figure 4: Plots of stress against shear rate for a type of hydrogel. The curves are indicative of shear-thinning behaviour. This specific graph looks at how the behaviour varies across temperatures [31].

2.2.1 Polyethylene glycol (PEG)

Polyethylene glycol is the hydrogel of interest in the scope of this project. It is modified and used as an injectable for heart attack therapies. These are ethylene oxide polymers that can be generalised as HO- (CH 2-CH 2-O) -H, where n indicates the average number of oxyethylene groups [32]. The substance's generic name denotes its molecular weight, with the structure shown in Figure 5 below.

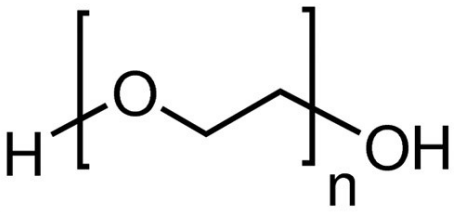

Figure 5: Molecular structure of PEG [33].

2.2.2 Comparison of Newtonian and Non-Newtonian property assumptions

Even though hydrogels exhibit non-Newtonian behaviour, they can be classified as Newtonian within a certain shear rate range. The preliminary computational investigation of PEG conducted by Ngoepe et al. [12] summarises the rheological properties of PEG for different conditions. A study using PEG 8000 showed that the hydrogel was **Newtonian up to a shear rate of 100** s^{-1} [34]. Another study using 4 kDa PEG showed that **viscosity is constant until a shear rate of 1000** s^{-1} [30]. After the specified range, the hydrogel exhibits **shear-thinning behaviour** (decreasing viscosity with increasing shear rate). There is an interesting property to note according to a study by Baldursdottir et al. [35]. Viscosity has a slight dependence on temperature changes, where it decreases within 1 $°C$ of the change in temperature and then stabilises [35]. The value at which it stabilises depends on the molecular weight of the PEG used.

2.3 Tissue Engineering Scaffolds

Tissue engineering scaffolds are structures that are put in place to support an affected organ. They are used in therapies that involve suspending isolated stem cells close to the site of injury, which promotes the formation of new tissue. The scaffold also provides mechanical support and maintains the structural integrity of the recovering organ [36]. There are different instances in which scaffolds can be used, such as for skeletal tissue, vascularised tissue, and myocardial patches. The focus of this project is the use of scaffolds in the heart.

The cardiac muscles remain active throughout life. The average number of cardiac cycles expected by the heart is roughly $3{\times}10^9$ [37]. This requires muscles with robust mechanical properties to ensure long-lasting performance. Therefore, the scaffolds used for the heart also need to meet a similar standard. The structural and mechanical properties must align with those of the native myocardium.

It is important to note the method by which a scaffold is placed in the heart. This

can be described as the "delivery mode" of the scaffold. The scaffold starts as a liquid mixture and gels upon delivery. Delivery modes can be categorised into two broad categories. A review by Davies et al. [38] summarises the categories in the following two subsections.

2.3.1 Infusion Delivery

Infusion delivery is a mode of delivery in which the liquid mixture is delivered to the heart through the coronary vasculature. The preferred method is **intracoronary infusion**, where the proximal aorta is reached by the femoral artery. The catheter is pressurised with a balloon to ensure that the backflow is limited and that the mixture is exposed to the infarcted area for longer. This route is preferred, given the familiarity of this procedure among cardiologists. This method is minimally invasive, making it suitable for high-risk patients. The downside of this method is that it can lead to pulmonary embolisms if larger stem cells are used. Figure 6 below visualises the different infusion delivery modes.

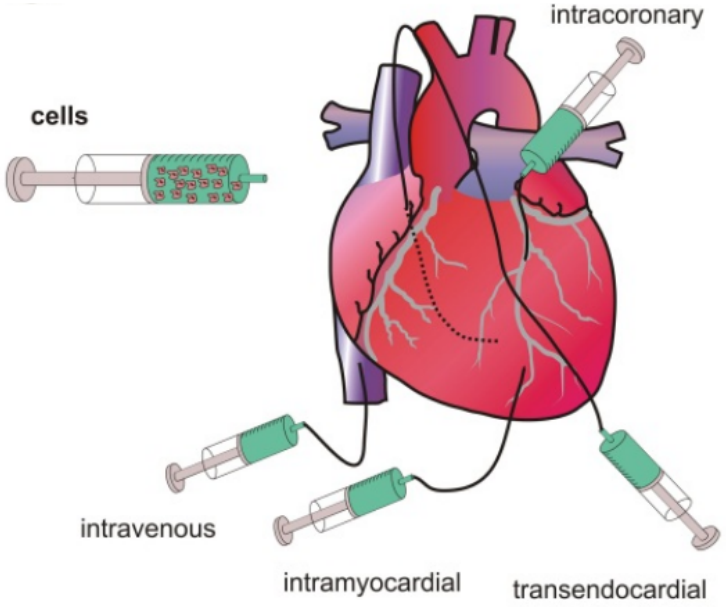

Figure 6: An illustration to highlight the different infusion delivery modes as well as the intramyocardial injection method [39].

Intravenous infusion is another method that uses a vein to access the heart. It is a straightforward and non-invasive method of administration. The downside of this is that the liquid mixture would need to be circulated multiple times before it comes into contact with the infarcted area. This is calculated based on the blood

flow rate, and the multiple circulations allow for exposure to other organs, therefore diluting the mixture.

2.3.2 Intramyocardial injection

Intramyocardial injection is a mode of administration in which the mixture is injected directly into the heart using a catheter. It can be done epicardially (the outermost layer of the heart) or endocardially (the innermost layer of the heart).

Epicardial delivery is performed by surgical exposure. This method enables precise delivery of cells to the infarcted area and permits the use of larger cells due to the reduced risk of embolism. Given the invasive nature of this method, not every patient can undergo treatment using this approach because of the risks associated with open heart surgery.

Endocardial delivery uses a catheter inserted into the heart through a blood vessel, typically in the arm. The catheter is guided using imaging techniques, and the mixture is injected perpendicular to the surface. This allows for precise cell delivery with the added benefit of a minimally invasive procedure. Figure 7 visualises the difference between epicardial and endocardial delivery modes.

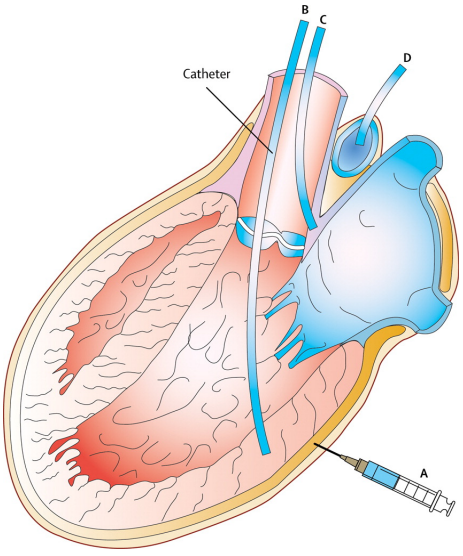

Figure 7: An illustration to show the two delivery methods. A is direct intramyocardial through the epicardium. B is direct intramyocardial via the endocardium [40].

2.3.3 Material Considerations

Subsequently, one also needs to consider the material used for the scaffold. There are many requirements for a scaffold, as outlined by Fergal J. O'Brien [41], and these are described as follows:

1. **Biocompatibility** – It is crucial to ensure that there are no immune reactions that could lead to inflammation. This can further lead to reduced healing or even complete rejection by the body.
2. **Biodegradability** – This is important because scaffolds are intended to last only for the duration of the healing process. After the healing process, there is no need for a surgical procedure to remove it and it breaks down by itself. This allows cells to produce their extracellular matrix (a complex network of macromolecules). It is important that the degradation products be non-toxic, as their accumulation can cause negative side effects, such as inflammation.
3. **Corresponding mechanical properties** – This should be taken into account to ensure that the scaffold does not affect the function of native tissue. If it is stiffer than the native tissue, it can restrict movement and cause damage. Softer scaffolds provide insufficient support and can collapse during movement. Moreover, this requirement affects the porosity requirement of a scaffold. These two requirements can be described as inversely related, as increasing the porosity usually means a decrease in the mechanical strength, and vice versa.
4. **Scaffold architecture** – This looks at the porosity of the scaffold and the interconnected pore structure. The interconnected pore structure is the network of pores that are connected. Porosity is the amount of empty space available within the scaffold to allow the movement of particles through it. The pores allow for the diffusion of nutrients to the cells within the scaffold and the diffusion of waste products out.
5. **Manufacturing technology** – For a scaffold to be clinically available, it needs to be cost-effective and be able to be made in bulk. Furthermore, it must be made accessible to the clinician in a suitable manner, which determines how it will be stored. There are two classes of materials that can be used to construct the scaffold: biological and synthetic materials.

2.3.4 Biomaterials for scaffolds

In this particular context, a biomaterial can be defined as a material designed to interact with a biological system for treatment. They can be classified into two

groups: natural/biological and synthetic. It is worth highlighting that these biomaterials should be injectable, as this method of delivery is relevant.

2.3.4.1 Natural/biological materials

Natural materials are obtained from biological sources, often in polymer form. They are typically biocompatible and meet most of the requirements outlined in Section 2.3.3. They also have the added benefit of possessing a structure similar to that of native tissue. There are different types, and some of these are summarised by Arnal-Pastor et al. [39] as follows:

Fibrin is a natural biopolymer and can be obtained by using a solution of fibrinogen and thrombin. Fibrinogen can be obtained from commercially available preparation methods or extracted autologously (from the patient's own blood).

Collagen supports the growth and survival of cardiomyocytes in vitro. It is usually obtained from bovine skin and tendons, as well as porcine skins. It has been shown to improve cardiac function and geometry in animal models when used alone.

Alginate is a linear copolymer that is obtained from seaweed. It has been shown to increase scar thickness and limit systole and diastole dysfunction in rat infarctions.

2.3.4.2 Synthetic materials

Synthetic materials are artificial materials that are designed in a specific way to match native tissue. In addition to matching the properties of native tissue to a high degree, these materials can be produced in large volumes with little to no variation between batches. There are different types of these synthetics, and Arnal-Pastor et al. [39] summarises them as follows:

Polyethylene glycol (PEG) is a hydrogel that can be used in different ways as an injectable. One way is to use a non-biodegradable type of PEG to provide permanent support; however, this induces an inflammatory response. Another way is to use a combination of gel and stem cells. A month post-injection, vessel growth increases and the gel is absorbed, which limits ventricular dilation and enhances ejection fraction. This hydrogel undergoes gelation through a cross-linking method, which will be discussed later.

Self-assembling peptides (SAP) are hydrogels that undergo gelation via a change in pH (physiological pH). These have been proven to be useful for maintaining the cells at the site of interest.

Thermosensitive hydrogels undergo gelation at a specific temperature. This is useful because they can be designed to gel at body temperature. They are typically

non-biodegradable but can be made biodegradable by copolymerising with degradable polymers. When injected in vivo in rats, it has been shown to preserve the left ventricular cavity and its contractility.

2.4 Gelation

Gelation can be simply described as a solidification process in which a polymer solution is transformed into a gel. The polymer solution in this context would be a liquid with a particular viscosity, which can flow when a force is applied to it. The gel can be represented as a system with infinite viscosity that does not flow when a force is applied, thus beginning to behave like a solid.

At the molecular level, the process can be described as follows: cross-linking long polymer chains forms a three-dimensional continuous network that traps the liquid within it to create a rigid structure resistant to flow [42]. This is a form of chemical gelation and is not the only mechanism by which gelation occurs. Gelation can be categorised into two groups, physical and chemical. The classification depends on the type of link between the polymer chains. A review by Gulrez et al. [43] summarises the mechanisms in the following subsections.

2.4.1 Mechanisms

Physical gelation can be subcategorised between "strong" gels and "weak" gels. Strong gels form due to permanent links between polymer chains, and they maintain this state under any experimental condition. Examples of these include **glassy nodules** and **lamellar microcrystals**. Weak gels form because of reversible links, which have finite lifetimes. The links break down and reform continuously, often depending on physical conditions such as temperature and pH. Examples include **hydrogen bonds** and **block copolymer micelles**.

Chemical gelation results in the formation of gels analogous to strong physical gels. The formation of covalent bonds between polymer chains results in strong gels. Examples include **condensation** and **addition** polymerisation, and **crosslinking**. This project uses cross-linking as the gelation method for PEG.

2.4.2 Cross-linking

A cross-linking agent enables different polymer chains to join. This agent is required in cases where the polymer chains do not react with each other or react very slowly. In the context of this project, where 20PEG8Ac is analysed, the acrylate groups can react with one another to cross-link the chains. The downside is that the conditions required for this are specific and cannot occur at any temperature or pH, especially

within the body. A cross-linking agent accelerates the reaction [44], allowing it to occur over a broader range of temperatures and pH levels.

The cross-linking agent of interest is PEG tetra-thiol (10PEG4SH). The thiol (-SH) groups in the agent are electron-deficient, while the acrylate group in the original PEG is electron-rich. This disparity causes the reaction, which can be classified as a thiol-ene reaction. This reaction can be visualised below in Figure 8.

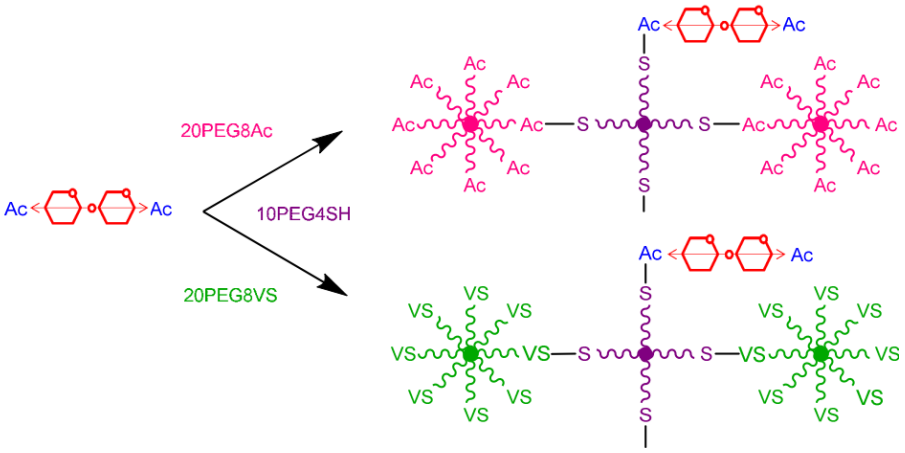

Figure 8: Reaction of PEG tetra-thiol with different types of PEG [13].

2.5 Existing computational models of non-Newtonian fluids

Given that the fluid being modelled is a non-Newtonian fluid, this section examines existing models of pseudoplastic fluids. More specifically, it examines CFD models, as this is the framework within which the hydrogel will be modelled. As seen in Figure 4 earlier, a pseudoplastic fluid demonstrates a decreasing viscosity with increased shear rate (shear thinning).

One area that has many similarities with this project is 3D food printing. The process prints food that behaves as pseudoplastic before gelation and as viscoelastic after. These include processed cheese, pectin gel, mashed potatoes, fish surimi gels, fruit-based snacks, and chocolate [45].

2.5.1 Rheology

To model a non-Newtonian fluid, it is imperative to know its dynamic viscoelastic properties. A rheometer, as seen in Figure 9 below, is a device that is used to obtain rheological measurements of fluid samples. The process can be explained simply as follows:

1. A fluid is placed between two plates and a torque is applied. Fundamentally, a rotational rheometer will apply/measure torque, angular displacement, and angular velocity.

2. From the parameters measured above, it can then calculate useful data. These can be summarised in Table 1 below.

Measured parameter	Calculated parameter	Related equations
Torque	Shear stress	$\sigma = M \cdot K_\sigma$
Angular displacement	Strain	$\gamma = \theta \cdot K_\gamma$
Angular velocity	Shear rate	$\dot{\gamma} = \Omega \cdot K_\gamma$

Table 1: Summary of parameters that can be calculated based on the measured parameters. M is the applied torque, θ is the angular displacement, Ω is the angular displacement, and K is the constant for each case [46]. K is dependent on measurement geometry or initial sample dimensions.

(a) A typical dual head rheometer.

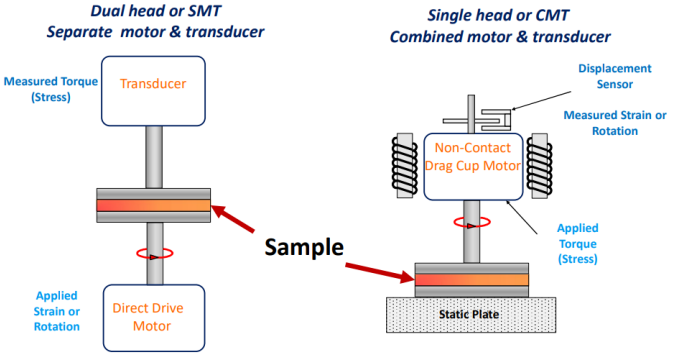

(b) Operating principles for both single head and dual head.

Figure 9: A rheometer and the operating principles of each type of rheometer [46].

Given that non-Newtonian fluids behave differently based on temperature and velocity, the rheological measurement is made based on the operating conditions of the fluid. Measurements can be made as follows:

1. Flow test – This is when a controlled shear stress is applied to the fluid and the resulting flow rate is measured. This test helps to determine the viscosity of the fluid.

2. Oscillatory test – This is when a sinusoidal strain is applied to the sample and the stress response of the sample is measured. Typically, for viscoelastic fluids,

there is a phase shift between input stress and output strain, which is used to calculate the loss and storage moduli.

Even within the rheometer itself, there are different geometries for the plates, and these can be seen below in Figure 10. These are chosen based on the viscosity of the fluid, which ranges from low to high viscosity.

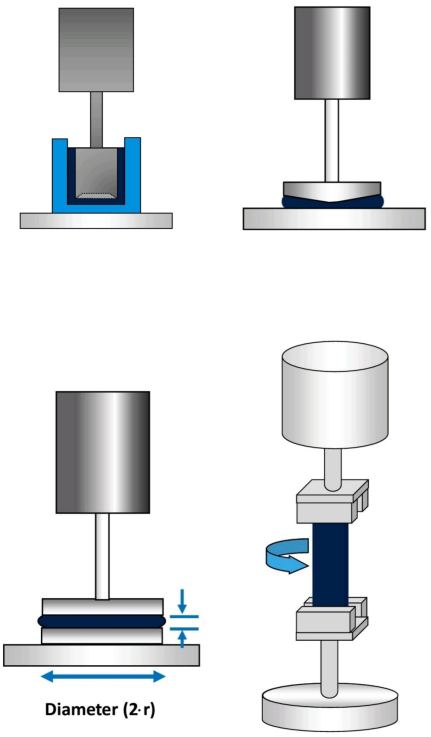

Figure 10: Different geometries for testing fluids/solids, arranged in order based on the viscosity of the fluid being measured [46]. Top row - Concentric cylinder geometry, Cone and plate geometry. Bottom row - Parallel plate geometry, torsional test.

2.5.2 Computational model of lemon juice gel

In a study by Yang et al. [45], the rheological properties of lemon juice gels were investigated after mixing lemon juice with different starches (wheat starch, corn-starch, etc.). This information is then used to simulate the effect of various process parameters (flow rate, nozzle diameters, etc.) on the velocity and shear fields. The gel is used in a syringe-based extrusion 3D printing process. This is akin to pipe flow and can be modelled using FEM.

To begin with, lemon juice gel samples were formed using raw materials and kept under controlled conditions. A rheometer, equipped with parallel plate geometry, took rheological measurements of the samples. All measurements were made within the linear viscoelastic region (LVR) to prevent structural breakdown (yielding). This can be determined by conducting a stress-strain sweep. Measurements are taken by keeping the frequency constant and increasing the stress/strain until there is structural breakdown. After determining the LVR, the viscosity parameters can be obtained by varying the shear rate within this region. Figure 11 below shows how the storage modulus varies during the stress sweep and how that is used to determine the LVR.

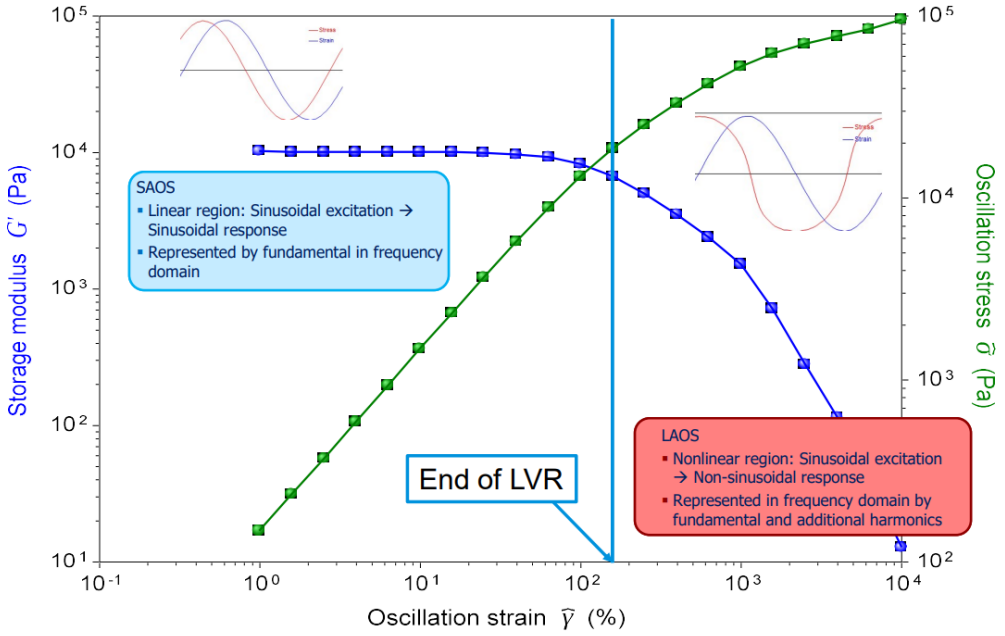

Figure 11: A plot of the data obtained from a typical stress/strain sweep which shows how the linear viscoelastic region is determined [46].

Because of the complexity of the flow of such materials, some assumptions are made to simplify it:

1. The material is described as **incompressible**, **highly viscous**, and **non-Newtonian**.
2. The material is **fully filled** in the flow channel. It is **an isothermal, steady, and laminar flow**.
3. **Inertia and gravity are negligible** relative to viscous forces because of the high viscosity mentioned above in assumption 1.

4. **No-slip condition** between the material and the channel wall.

With all of these taken into consideration, the fluid is modelled using the Carreau model [47] as follows:

$$\eta = \eta_\infty + (\eta_0 - \eta_\infty)[1 + (\Gamma\dot{\gamma})^2]^{\frac{n-1}{2}}, \tag{1}$$

where η_0 is the zero shear rate viscosity, η_∞ is the infinite shear rate viscosity, Γ is a material time constant (relaxation time), $\dot{\gamma}$ is the shear rate, and n is the rheological index. This can accurately describe the rheological curve at low-to-moderate shear rates. The simulations were carried out and the effect of the flow rate and diameter of the nozzle on the flow parameters were determined. The flow parameters are velocity, shear rate, and pressure. The parameters were found to be stable within most of the flow channel and varied significantly within the inlet (a nozzle in this case). The material flow rate determined the velocity and shear rate fields. The pressure in the flow channel increased with:

- Increasing material viscosity and flow rate.
- Decreasing relaxation time and nozzle (inlet) diameter.

2.5.3 Computational model of Pluronic F127 in a coaxial extrusion process

Pluronic F127 (PF127) is a typical non-Newtonian material used in the study by Yu et al. [48] simply because it is readily available and its behaviour can be easily tailored to specific needs. The purpose of the study was to determine the effect of viscosity and flow rate ratio on the stability of the extrusion process. The powdered form of PF127 was used to create different fluids by varying the weight percentage of PF127. One of these was used as the constant extrudate alongside which other fluids were extruded.

To obtain rheological measurements, a rheometer was used with different geometries. They utilised a cone geometry for the lower viscosities and a parallel plate geometry for the higher viscosities. The tests involved applying a flow ramp function, with the shear rate increasing from 0.1 1/s to 1000 1/s. To fit the data, the Herschel-Bulkley model was used. The model is used as follows:

$$\tau = \tau_0 + k\dot{\gamma}^n, \tag{2}$$

where τ is the shear stress, τ_0 is the yield stress, k is the consistency index, and n is the flow behaviour index. This is a type of fluid that can sustain a certain

amount of shear until it begins to flow. After that, it flows either like a shear-thinning or shear-thickening fluid, depending on the flow behaviour index. This can be illustrated below in Figure 12:

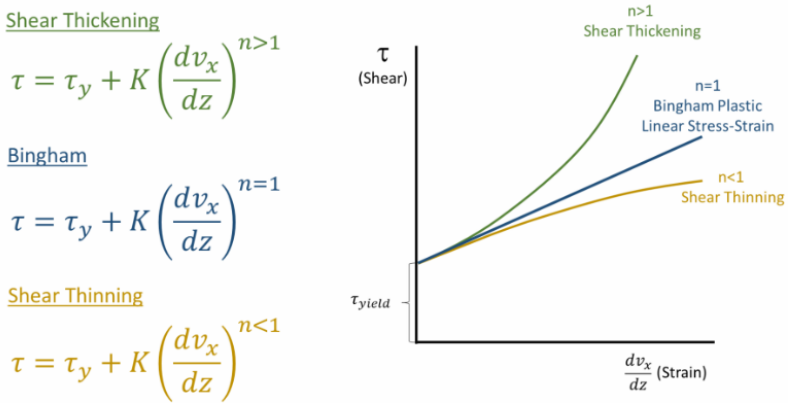

Figure 12: A stress-strain plot highlighting how a Herschel-Bulkley fluid varies based on the flow behaviour index [49].

The boundary conditions specified for the computational study were defined as follows:

1. The incoming flow is **fully developed**.
2. **No-slip condition** at the boundary
3. **Pressure is zero at the outlet** to compensate for hydrostatic pressure.
4. Backflow was suppressed at the outlet.

The discussion in this study focused more on the coaxial extrusion process concerning the ratios of the fluid parameters (flow rate and viscosities). Therefore, they are not mentioned as they do not affect the considerations made for this project.

2.6 Injectable hydrogel treatment

In Section 1.1 it is briefly mentioned that the treatment of interest is the injection of a scaffold alone into the affected area. The purpose of this is to provide mechanical support to the affected area. This section seeks to expand on this treatment by explaining the reasons why researchers use it and existing cases where they have found success with the treatment. Following this, existing computational models of the hydrogel present in the myocardium are explored.

Looking back at Section 2.1.2, alterations in the myocardium after MI result in left ventricle (LV) dysfunction. These include a reduced ejection fraction and an increase in diameters relating to end-diastole and end-systole. Diastole refers to the relaxation of the heart as it fills with blood, while systole refers to the contraction of the heart as it pumps blood out. An increase in the diameter of the left ventricle at the end of each step indicates reduced pumping efficiency. The ejection fraction is the percentage of blood that leaves the heart after each contraction. A reduced ejection fraction shows that a heart cannot work to meet the requirements of the body. Injecting hydrogels into the infarcted tissue can counteract the effects of LV dysfunction.

2.6.1 Existing cases of treatment

The treatment has been tested widely on different animal models ranging from rats to pigs. In addition to this, treatment has also been investigated in humans. The smaller animal models that have been used include rats and rabbits. A study by Dobner et al. [50] used male Wistar rats and non-degradable PEG. The study showed that the treatment resulted in a reduced left ventricular end-diastolic diameter (LVEDD) and a reduced left ventricular end-systolic diameter (LVESD). In addition to this, there was reduced wall thinning, which improves heart function. A study by Jiang et al. [51] used male rabbits and a PEG-based hydrogel. Their study showed that treatment resulted in an increased ejection fraction, a decrease in LVEDD and LVESD, an increase in scar thickness, and a decrease in infarct size. Figure 13 below shows the difference in scar thickness between a control group and a treated group. The image was obtained by Masson's trichrome staining.

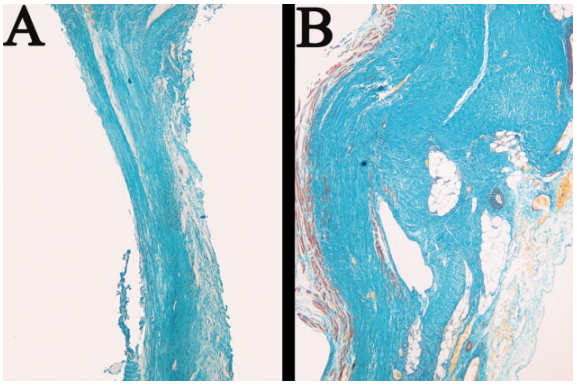

Figure 13: Scar thickness in rabbit myocardium injected with saline (image A) and hydrogel (image B). Image B shows an increased scar thickness as compared to the control [51].

The larger animal models that have been used include sheep and pigs. A study by Morita et al. [52] used adult male sheep and a reactive tissue filler. Their results indicated that after treatment, the infarct became thicker and stiffer, which is beneficial. The results also indicated that the injectate improved the overall function of the LV and reduced LV remodelling. Figure 14 below shows the difference in LV shape between a treated and an untreated heart.

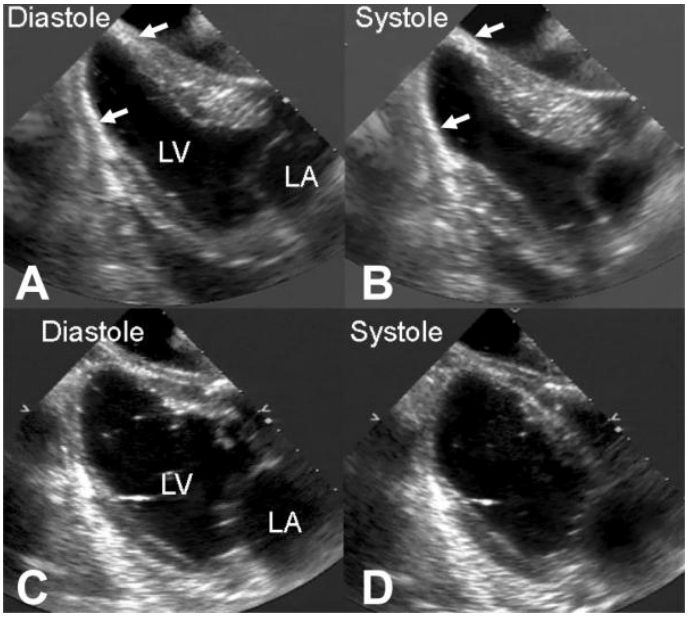

Figure 14: Echocardiogram showing the difference in LV shape between a treated and untreated sheep heart. Images A and B show the reduced LVEDD and LVESD of a treated heart compared to Images C and D [52].

Another study by Dorsey et al. [7] used Yorkshire male swine and a hydrogel based on hyaluronic acid. Their results are consistent with those obtained by Morita et al. [52] using sheep heart models. The study showed an overall improvement in the structure and function of the LV, with a preserved thickness of the infarct and a reduced dilation of the infarct. Figure 15 below shows a graphical representation of the different LV parameters between control groups, treated groups, and pre-MI groups. These studies demonstrate the potential of the treatment to treat MI and provide the basis for its introduction into humans.

A study by Frey et al. [9] tested the treatment in human patients with moderate to large ST-segment elevation myocardial infarctions. The injectable scaffold consisted of sodium alginate and calcium gluconate. The results of this study proved that the treatment was feasible and did not cause any adverse reaction. In addition,

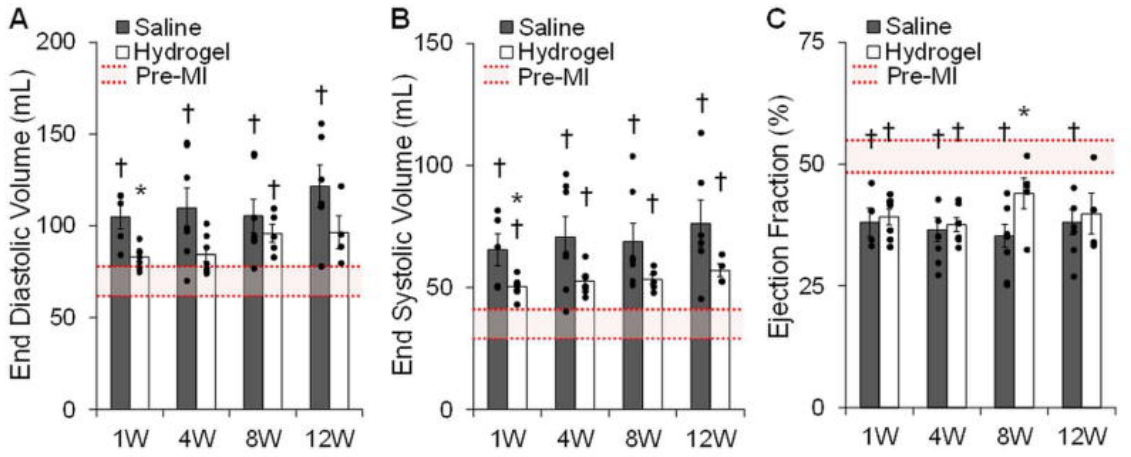

Figure 15: Graphical representation of diastolic and systolic volumes and the ejection fraction in pig hearts. The saline represents the control group which undergoes MI and is injected with saline. The x-axis represents the weeks within which the measurements are taken and shows the effect of the treatment over time [7].

the study showed that the injection did not compromise microvascular blood flow. The results of the study showed minimal dilation of the LV cavity and a preserved ejection fraction. There are limitations to this study, one of which is the lack of a control group. However, the study proves the safety and efficacy of the treatment in humans, which motivates further studies.

2.6.2 Existing computational models

Previous studies have attempted to model the gel within the myocardium computationally. This approach allows for the development of the treatment without the need for an in vivo study, thereby reducing the overall cost of research and development. To do this accurately, some considerations must be made, and the cardiac mechanics must be characterised. The myocardium is a viscoelastic and anisotropic material that behaves differently during contraction and relaxation. It comprises muscle fibres (myofibres) whose orientation affects cardiac mechanics and, therefore, must be assigned appropriately. Infarct tissue does not behave like healthy tissue, and it needs to be characterised when modelling with healthy tissue. Lastly, the geometry of the heart with infarct tissue and gel affects the results, and this should be taken into account when setting up a model.

A study by Wenk et al. [53] used one domain to define the entire geometry. The material response was assumed to be incompressible, transversely isotropic, and hyperelastic. They used the constitutive models for active contraction and passive

filling, and they applied the boundary conditions as described in their paper [53]. The effect of infarct tissue was modelled by removing active contraction in the specified area. The effect of the gel on the infarct tissue was modelled by adjusting the passive filling model. Passive stiffness parameters were adjusted until the radial component of strain was close to 0. This behaviour was observed in a previous study [54]. The FE results of this study showed reduced stress in the treated regions and improved ejection fraction. Figure 16 below shows a stress contour plot between a treated and an untreated infarct.

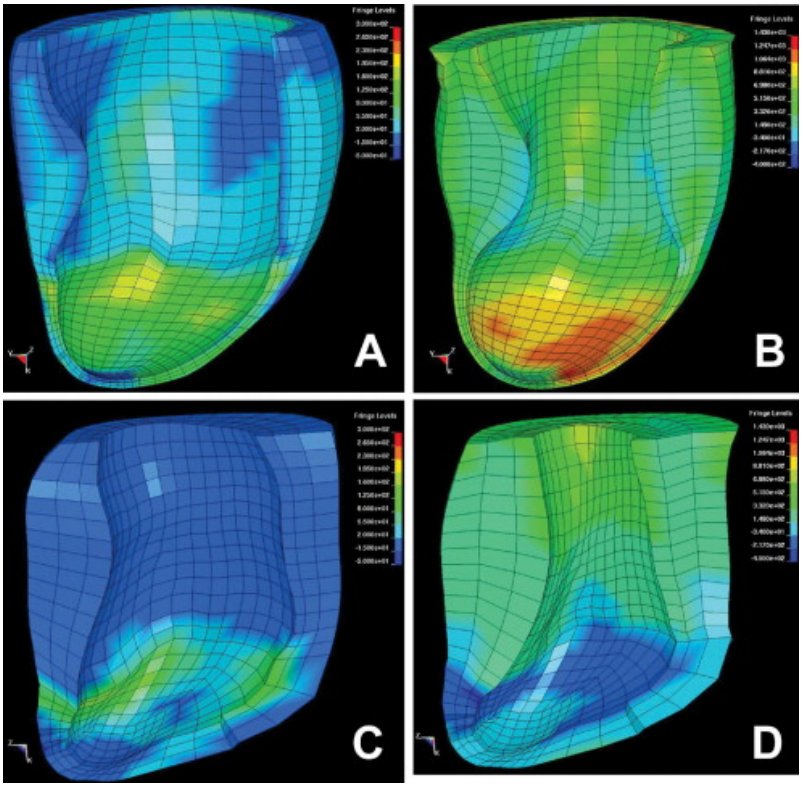

Figure 16: Fibre stress distribution between a treated (C and D) and untreated (A and B) left ventricle during diastole (left column) and systole (right column) [53].

A study by Kortsmit et al. [55] used multiple subdomains to define the geometry of the heart and the gel. This provides a good representation of the gel distributed within the myocardium and the effect that distribution has on the stress response. Figure 17 below shows how the gel domain was layered in between the tissue domain. This layered distribution approximates what previous studies observed [50]. The details of their constitutive models and boundary conditions can be found in their paper [55].

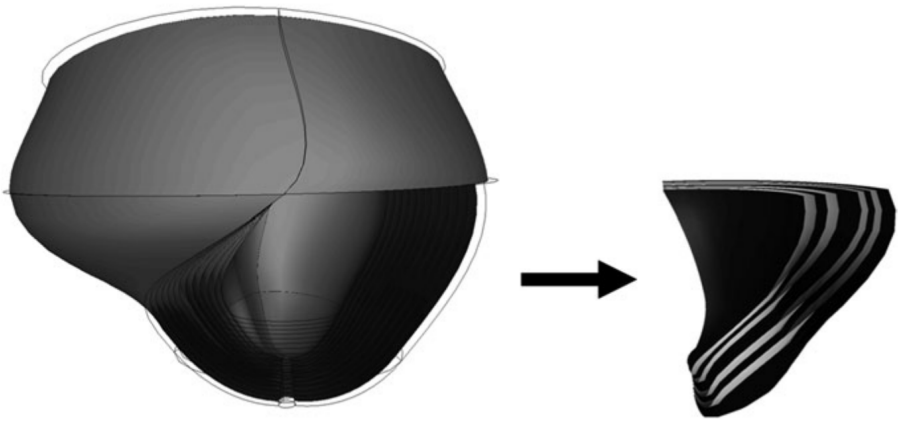

Figure 17: A 3D mesh of the heart (right) which shows the hydrogel (in white) layered in between the infarct tissue on the left [55].

The difference between this and the previous study is that the gel is modelled in the myocardium with its own subdomain. The gel is modelled as an isotropic material that behaves in the same way as passive myocardium without active contraction. An earlier study [50] showed that the gel has half the stiffness of healthy tissue. This provided the basis for altering the stress scaling coefficients in the constitutive model appropriately. Additionally, the passive behaviour of the infarcted tissue is captured by decreasing the passive mechanical properties in the constitutive model. FE results demonstrated lower myofibre stresses, improved contractility, and improved ejection fractions.

Another study by Motchon et al. [56] used a realistic geometric representation of the gel in the myocardium. The geometry was obtained by using microcomputer tomography images. In this study, the passive-filling behaviour is described using a hyperelastic anisotropic law. Active contraction is implemented with a time-varying elastance approach. The model includes a health parameter that represents the pathological stage of the myocardium. Compared with the previous study by Kortsmit et al., this study modelled the gel as a hyperelastic isotropic incompressible material with a separate constitutive model. The details of their material models and boundary conditions can be found in their paper [56]. Figure 18 below shows the gel distribution within the myocardium. The study conducted a parametric study in which the stiffness of the gel was varied in the FE model. The results showed that a stiffer gel results in reduced myofibre stress in both diastole and systole.

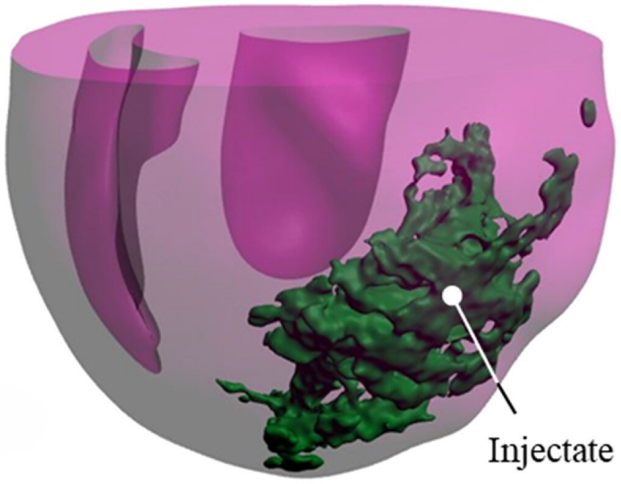

Figure 18: Biventricular geometry of a rat heart developed from micro-CT imaging showing the dispersion of gel within the infarcted tissue [56].

Typically, studies investigating the effect of PEG in the myocardium model PEG as a solid. Some research has also been conducted where PEG has been modelled as a liquid prior to gelation. In a study by Ngoepe et al. [12], PEG is modelled as a non-Newtonian incompressible fluid with a power law model for viscosity. Although PEG may behave as a Newtonian fluid as seen in the literature discussed earlier in Section 2.2.2, its behaviour deviates on the microscale. The study also investigated the flow of PEG in a microchannel that is representative of the gaps in the myocardium. Their in vitro study showed that PEG exhibited shear-thinning behaviour at that scale. The parameters for the power law model are obtained and used for their in silico study.

The purpose of the in silico study [12] was to investigate whether the flow region has a significant impact on gel transport. Different myocardial flow regions were selected from the existing geometry of left ventricular tissue, as depicted in Figure 19 below. The same mass flow rate was specified at the inlet of each region, and the velocity and shear rate were analysed for each region. The results show that the flow region affects the flow behaviour of PEG. In addition, per region, a large variation in shear rate was observed. This emphasised the need to account for PEG's shear thinning properties, as varying shear rates affect its viscosity in different regions of the myocardium.

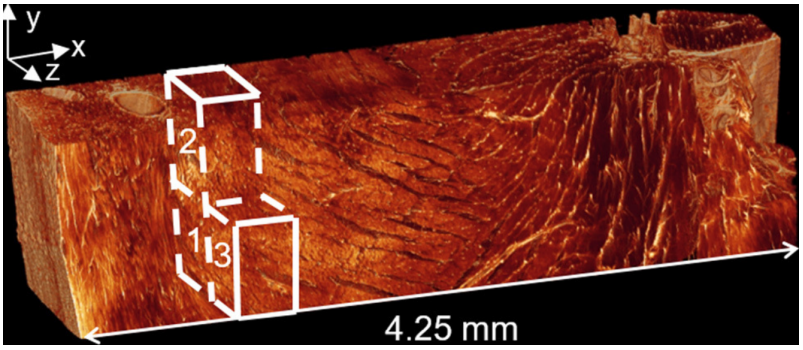

Figure 19: Confocal microscopy image of left ventricular tissue [12].

The studies discussed primarily model PEG as a solid or liquid, revealing a gap in the literature. None of the studies account for the dynamic change in viscosity over time as PEG undergoes gelation. To address this, this study aims to model PEG as a gelling material to provide a more accurate representation of its behaviour.

3 Methodology

This chapter presents the methodology used to provide a solution that meets the research aim. It begins by detailing the governing equations for solving fluid flows and presents a strong form of a generalised fluid flow problem. The chapter continues to provide a summary for the use of numerical methods to solve fluid flows. The computational geometries used for the analyses are presented with their respective details. A brief overview of the modelling process done using Ansys Polyflow is presented. Subsequently, a methodology is presented to obtain a gelation material model from existing rheology data. The 2D geometry is then used to explore the use of a traction boundary in Polyflow, with some studies including the effect of gelling. A problem breakdown is presented, and using the results of the 2D studies, a modelling approach is presented. The 3D geometry is then used to carry out studies to build the computational framework to be used to provide a final solution. The final model is then used to carry out case studies to answer the hypothesis.

3.1 Governing equations

Looking back at the limitations outlined in 1.3.2, the PEG being modelled is classified as a Newtonian fluid. The existing literature also models it as incompressible [12]. The governing equations can then be stated using these two conditions. These are taken according to the ANSYS Polyflow user guide [57] as Polyflow is the solver of preference. The primary equation is the differential equation governing linear momentum for fluids, expressed as:

$$-\nabla p + \nabla \cdot \mathbf{T} + \mathbf{f} = \rho \mathbf{a} \,, \tag{3a}$$

where p is pressure, $\boldsymbol{T}$ is the viscous stress tensor, $\boldsymbol{f}$ is the volume force, ρ is the density, and $\boldsymbol{a}$ is the material description of the acceleration. The second equation is the incompressibility equation (mass continuity equation) which is:

$$\nabla \cdot \mathbf{v} = 0 \,, \tag{3b}$$

where $\boldsymbol{v}$ is the velocity.

The momentum equation can be further simplified using the incompressibility equation. Expanding the term that takes the divergence of the viscous stress tensor, one can write this in indicial notation as:

$$T'_{ij} = \lambda \Delta \delta_{ij} + 2\mu D_{ij} \,, \tag{4a}$$

where λ is a constant related to bulk viscosity, μ is the viscosity, Δ is the rate of change of volume, and D_{ij} is the rate of deformation tensor. Due to incompressibility, $\Delta = 0$. D_{ij} can be further expanded and written in indicial notation as:

$$D_{ij} = \frac{1}{2}\left(\frac{\partial v_i}{\partial x_j} + \frac{\partial v_j}{\partial x_i}\right) . \tag{4b}$$

Now, the divergence can be taken of the simplified viscous stress tensor which results in:

$$\frac{\partial T'_{ij}}{\partial x_j} = 2\mu\frac{\partial D_{ij}}{\partial x_j} = \mu\frac{\partial^2 v_i}{\partial x_j \partial x_j} + \mu\frac{\partial^2 v_j}{\partial x_j \partial x_i} . \tag{4c}$$

For the second term, the order of differentiation can be interchanged and rewritten. This change can only be made under the condition that the derivatives (second and prior) are continuous (Mixed Derivative Theorem). The change is made as follows:

$$\frac{\partial^2 v_j}{\partial x_j \partial x_i} = \frac{\partial}{\partial x_i}\left(\frac{\partial v_j}{\partial x_j}\right) . \tag{4d}$$

The term in brackets is the indicial form of the incompressibility equation and is therefore equal to 0. Finally:

$$\frac{\partial T'_{ij}}{\partial x_j} = \mu\frac{\partial^2 v_i}{\partial x_j \partial x_j} = \mu\nabla^2\mathbf{v} . \tag{4e}$$

Lastly, the acceleration can be expressed as a material derivative as follows:

$$\mathbf{a} = \frac{D\mathbf{v}}{Dt} = \frac{\partial \mathbf{v}}{\partial t} + (\nabla\mathbf{v})\mathbf{v} . \tag{4f}$$

Using all of these simplifications, the momentum balance in equation 3a can be rewritten as:

$$-\nabla p + \mu\nabla^2\mathbf{v} + \mathbf{f} = \rho\left(\frac{\partial \mathbf{v}}{\partial t} + (\nabla\mathbf{v})\mathbf{v}\right) . \tag{5}$$

Keeping in mind that the volume force, $\mathbf{f} = \rho\mathbf{B}$, where $\mathbf{B}$ is the body force per unit mass, equation 5 is the invariant form of the Navier-Stokes equations of motion for incompressible fluids.

3.1.1 Strong form

In the finite element method, one defines the strong form of a problem before solving it numerically. This takes into account the governing equations, boundary conditions, and initial conditions. In the case of the Navier-Stokes equations, the strong form can be defined as follows:

Find the velocity field, $\mathbf{v}(\mathbf{x}, t)$, that satisfies the following equations:

$$-\nabla p + \mu \nabla^2 \mathbf{v} + \mathbf{f} = \rho \left(\frac{\partial \mathbf{v}}{\partial t} + (\nabla \mathbf{v})\mathbf{v} \right), \tag{6a}$$

$$\nabla \cdot \mathbf{v} = 0 \,. \tag{6b}$$

The following boundary conditions:

$$\mathbf{u} = \mathbf{g} \quad \text{on } \Gamma_g \ , \tag{6c}$$

$$\mathbf{n} \cdot \boldsymbol{\sigma} = \mathbf{h} \quad \text{on } \Gamma_h \ , \tag{6d}$$

and the following initial conditions:

$$\mathbf{v}(\mathbf{x}, 0) = \mathbf{v}_0 \quad \text{on } \Omega \ , \tag{6e}$$

where Γ_g represents the Dirichlet or essential boundary condition, and Γ_h denotes the Neumann or natural boundary condition. A Dirichlet boundary condition is when the value from the solution is specified on the boundary, and in this case it would be the velocity. A Neumann boundary condition is when the derivative of the solution is specified on the boundary, and in this case, it would be the traction.

3.2 Numerical methods

3.2.1 Introduction to numerical modelling

Multiple phenomena in engineering can be mathematically described in terms of partial differential equations. Examples include heat transfer, stress analysis, and fluid flow. Solving these equations is of interest as they help with various engineering analyses. These equations can be solved analytically for simple cases. However, solving these equations becomes increasingly difficult as the shapes of the problem domain become more realistic.

Numerical methods, like the finite element method (FEM), have been developed to approximate solutions to these problems. These approximations can become sufficiently accurate with changes made to the solving approach, making this a reliable approach for many analyses. Implementation of the numerical method is done using a computer program.

Simply put, the idea of FEM is to discretise a domain into *elements* which are connected using *nodes*. A problem can be mathematically manipulated and converted to the finite-element form. This is where a polynomial approximation is used to define the problem over the element. This is done in a piecewise manner for every element in the domain. All of these combined result in a system of equations that is solved. Usually, there are thousands of elements; hence, the need for a computer program to find the solution.

This project focuses on solving fluid flow, which introduces the use of computational fluid dynamics (CFD). CFD is used in different fields of engineering to solve complex flows. An area of interest is cardiovascular medicine, which has shown promise in solving fluid flow problems computationally rather than experimentally, which is often difficult in this case. It is important to highlight that in this project, the CFD simulations are done using a FEM-based solver.

3.2.2 Overview of the CFD modelling procedure

The general modelling procedure for the case of cardiovascular medicine can be described as follows. For cases where idealised geometries are used, the first two steps are not required. In those instances, geometries are developed using 3D modelling utilities.

- An imaging process takes place using medical imaging tools. The geometry used in this project was developed from existing confocal image data.
- The images obtained are processed using segmentation and reconstruction to develop a 3D geometry. This geometry defines the problem domain over which the flow will be solved.
- The geometry is discretised, or *meshed*. The level of refinement determines the accuracy of the solution that will be generated.
- The meshed geometry is imported into the solver program. Here, the boundary conditions are defined over the entire fluid boundary and the material parameters are set for the fluid.
- Time-dependent parameters are input for the case of transient models. The time over which the modelling is done is also discretised.

- The model is then solved numerically to obtain the required solution. It is worth noting that only a well-posed problem can be solved. If there are errors in the boundary conditions or material parameters, the solver will not run. Mesh refinement and time domain settings can impact the solution, potentially causing inaccurate results or solver failures.
- The solution is exported to a postprocessing program that is used to visualise the solution over the domain.

The list is very condensed and contains a lot of information and theory to unpack. This will be addressed later in the chapter, when the specific problem is looked at.

3.3 Computational geometries

It is assumed that PEG injected into the myocardium flows through its interstitial spaces. The geometries discussed are appropriately scaled and representative of these interstitial spaces.

3.3.1 2D geometry

The 2D computational studies performed use a simple geometry shown below in Figure 20. It is an axisymmetric domain that simplifies a 3D cylindrical geometry. The inspiration for this comes from a previous study [12], validated using micro PIV data, that used a microfluidic channel. The study used a square cross-section that requires a 3D domain to model it accurately in the context of this project. This is because the modelling strategy in this project applies a traction boundary condition on the outer surface of the domain. For a square cross-section, one would need to consider both planes of symmetry when using this type of boundary condition. The purpose of these studies is to analyse the effect of traction on flow. To reduce computational expense, a circular channel is modelled with the same hydraulic diameter. The domain has a radius of 28.2 μm and a length of 15 mm.

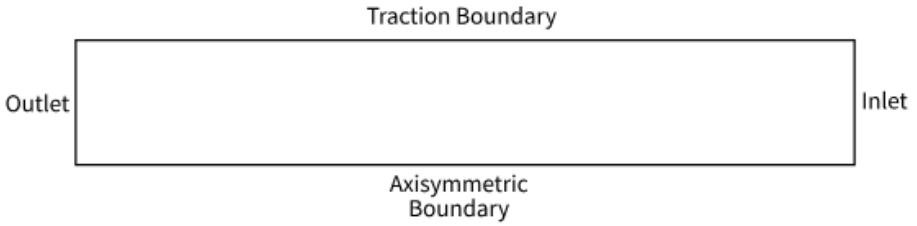

Figure 20: Illustration of the 2D microfluidic domain.

3.3.2 3D geometry

The 3D computational studies performed use a more complex geometry compared to the 2D studies. The geometry used is derived from confocal microscopy imaging and these same images were used in a previous study [12]. These images were imported into Simpleware ScanIP to reconstruct the 3D geometry. The confocal microscopy image and the reconstructed geometry can be seen below in Figure 21.

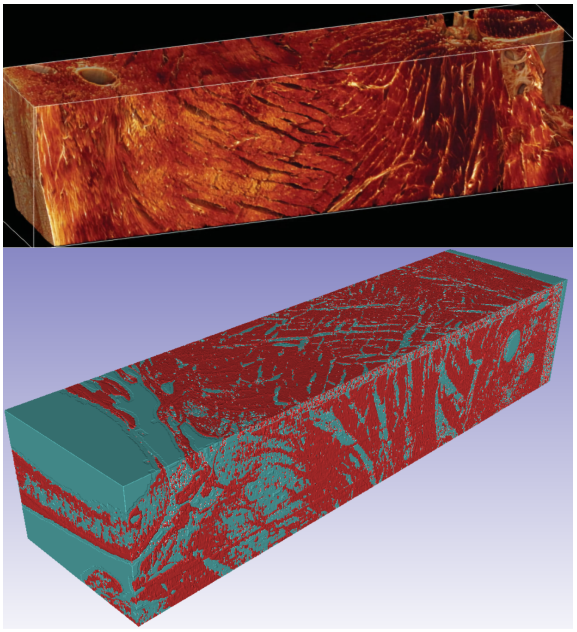

Figure 21: Confocal microscopy image of left ventricular tissue (Top) [58]. The dimensions of this tissue block are $4.25 \times 1.12 \times 0.88\ mm$. The bottom image is the reconstructed geometry in Simpleware. The regions in blue show the spaces that would be occupied by PEG.

A region of interest is selected from this tissue block that spans a region of $351 \times 311 \times 380\ \mu m$. Before post-processing, the geometry is extremely irregular due to the nature of the myocardium. Using such a geometry substantially increases computational expense. There is also the chance of simulations failing if no continuity exists between inlets and outlets. Image segmentation and post-processing techniques were used to modify the geometry and mitigate the issue of no continuity. Techniques such as manual segmentation, region growth, level-set thresholding, and mask smoothing were used to modify the geometry. The region of interest before and after post-processing can be seen below in Figure 22.

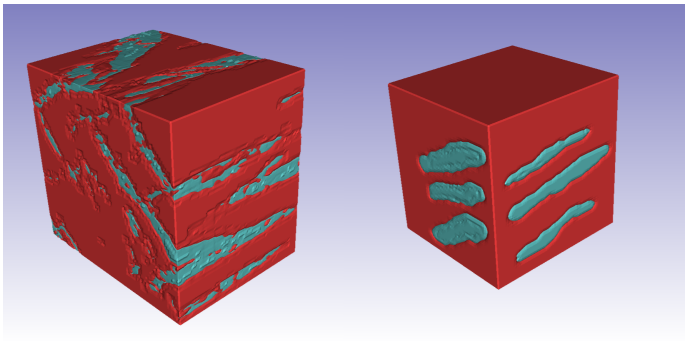

Figure 22: Region of interest before post-processing (left). Region of interest after post-processing (right).

The modified domain in Figure 22 shows two subdomains that represent the myocardium (in red) and the PEG (in blue). These two subdomains were used for the first time in an FSI model from a previous project [59]. The FSI model is discussed later in Section 3.7.1. The PEG domain from this is used for the CFD simulations in this project. This domain can be fully visualised in Figure 23.

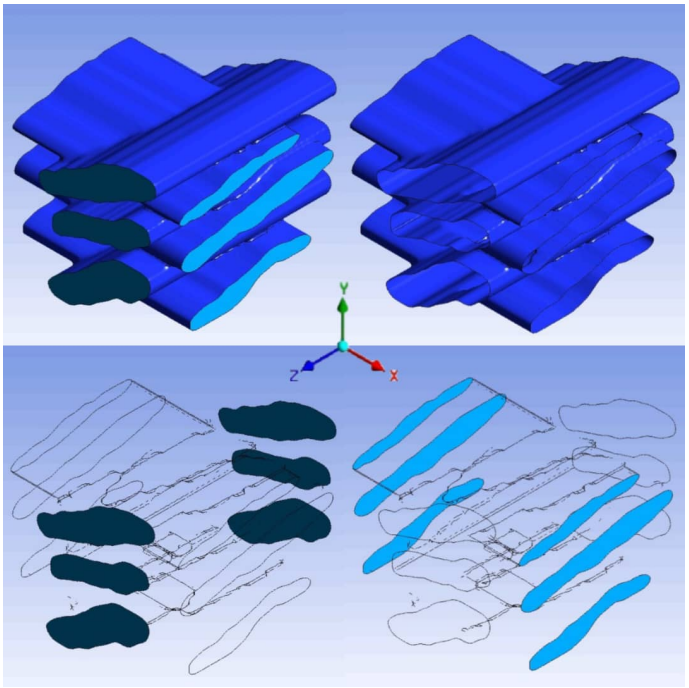

Figure 23: Visualization of the 3D fluid domain (top left), the outer surface (top right), the two outlets along the z-axis (bottom left), and the two outlets along the x-axis (bottom right).

Figure 23 highlights five relevant boundaries. These are:

- **Outer surface** - This can be seen in the top right image. This is the outer surface of the fluid domain
- $\mathbf{Z_{positive}}, \mathbf{Z_{negative}}$ - These can be seen in the bottom left image. These are the outlet/inlet faces that are normal to the z-axis.
- $\mathbf{X_{positive}}, \mathbf{X_{negative}}$ - These can be seen in the bottom right image. These are the outlet/inlet faces that are normal to the x-axis.

3.4 Overview of the ANSYS Polyflow modelling process

The following section looks at how the solver is set up. This section explores the latter stages of the CFD modelling process after importing a meshed geometry into the solver, as discussed in Section 3.2.2. It is important to define the characteristics of the computational model before starting the modelling process, as these will influence the choices made during the solver setup.

The computational models in this project are characterised and justified as follows:

- 2D/3D - In the upcoming sections, both 2D and 3D problems are solved.
- Newtonian fluid - The problem is simplified to use a Newtonian fluid.
- Incompressible - PEG is largely made up of water which is an incompressible fluid. Previous studies have also modelled it as incompressible [12].

Bearing this in mind, the modelling process in Polyflow can now be described specifically for the type of problem being solved. This specificity is required as Polyflow can solve different computational models. Each model requires in-depth explanations, and for the sake of concision, explanations are given for the model specific to the project. The modelling process in Polyflow can be described as follows:

- Define a *task*, which refers to a problem that can be solved. For all models in this project, a FEM task is used. A task may be defined as steady-state or time-dependent, and both types are considered in the project. In the case that a 2D geometry is imported, one can choose between planar and axisymmetric geometries.
- Within a task, one can define a *sub-task* that describes the physics model that will be solved. In the case where time dependence is specified, one can also set the transient iterative parameters. These include the start and end times, the time step size, and the integration method.

- Various physics models are used to solve solid and fluid problems. For all models in this project, a **generalized Newtonian isothermal flow problem** model is used. Within this model, one can set the material data and specify the flow boundary conditions.
- For the model described previously, the material data that can be specified include the shear-rate dependence of viscosity, density, inclusion of inertia, and gravity. Gravity is ignored for all models since the fluid masses are small, making its force negligible compared to other forces. Inertia is taken into account for all transient simulations and the density is kept at a constant value. The shear-rate dependence of viscosity is chosen as **constant viscosity**. For cases where gelation is modelled, time dependence is assigned to this viscosity using the EVOL option and a user-defined function (UDF). The function used is derived later in Section 3.5.4.
- After specifying the material data, the flow boundary conditions can be specified on all the boundaries. These boundaries would have been named and set in a meshing utility earlier in the meshing process. The boundary conditions that are used in the project are explained in detail in Section 3.4.1,
- Once the boundary conditions have been specified, the solver is run and the solution for the problem over the domain is computed. The solution can then be exported to a graphical postprocessor that can be used to analyse the solution and derive further solutions.

3.4.1 Boundary Conditions

In the coming chapter, boundary conditions are mentioned that are not explained in detail under each simulation for the sake of concision. These are explained in detail in this section. In the following descriptions, $\mathbf{v}$ denotes velocity and $\mathbf{f}$ denotes surface force densities, more commonly known as traction. These descriptions come from the solver user guide [57].

- Zero wall velocity condition ($v_n, v_s = 0$) - This sets the normal and tangential velocity components on the boundary to zero.
- Symmetry condition ($f_s, v_n = 0$) - This sets the normal velocity and the tangential traction to zero on the plane of symmetry for planar problems. This is equivalent to the axisymmetric boundary condition for axisymmetric problems.
- Outflow boundary condition ($f_n, v_s = 0$) - Although there is a boundary condition that can set this exact boundary condition, this is a preset condition which is used to model an outlet for a domain.

- Inflow boundary condition - One can specify the volumetric, mass flow rate, or normal velocity across a boundary surrounded by other boundary sections with properly defined adhesion conditions (slip, no-slip, or symmetry). Units are automatically handled when moving between 2D and 3D models. Polyflow computes the inflow using either a fully developed method or a constant normal force. This can be specified or set as automatic for Polyflow to choose the best method.

  For the fully developed method, Polyflow solves a fully developed problem. This assumes that all derivatives normal to the inlet are zero except the pressure gradient. Polyflow then imposes the computed velocity profile as the prescribed velocity. For the constant normal method, the normal force is prescribed, and its value is used to obtain the flow rate. The pressure value is calculated, and the velocity components are not prescribed.

- Normal traction and tangential velocity condition (f_n, v_s) - This is used to specify a normal traction with a tangential velocity on the boundary. Similar in nature to the outflow condition, it is worth noting that one may specify a Dirichlet boundary condition to one component of the solution and a Neumann boundary condition to another component. One cannot specify both in the same component (for example, f_n, v_n) as it may lead to incompatibility.

- Normal traction and tangential traction condition (f_n, f_s) - Similar to the previous condition, this is used to specify a normal and tangential traction on the boundary.

3.5 Rheological behaviour of PEG during gelation

3.5.1 Background

The following section looks at the procedure followed to model PEG as it undergoes gelation in silico. It is important to note that this method is not case-specific, and it can be adjusted for use with other forms of PEG, provided it is modelled within the same framework. The data used comes from a project [13] that investigated gelation times and viscoelastic fluid properties for different forms of PEG. These forms are not the standard 20PEG-8OH, which is non-reactive by itself. It is modified to include either acrylate (Ac) or vinyl sulfones (VS) that allow the hydrogel to form cross-links and undergo gelation. In this project, each variation of the gel is also mixed with heparin (hep) and heparin sulphate (HS), which creates gels with improved healing properties. This aspect is not discussed in detail as it does not provide additional insight into understanding fluid behaviour.

Various gelation data sets exist from the previous study [13], and the most appropri-

ate one is chosen for this project. Looking back at Section 2.3.3, the requirement for a scaffold is that it must be biodegradable. Therefore, the gelation reaction studied involves the copolymerisation of **20PEG8Ac** with **10PEG4SH** which results in a degradable gel. In this reaction, 20PEG8Ac serves as the hydrogel, while 10PEG4SH acts as the crosslinker. The details of this reaction are covered in Section 2.4.2. Two datasets analyse this reaction: one with hep and one with HS. In the previous study [13], it is mentioned that the heparin sulphate-based gel is more suitable for myocardial infarction therapy; therefore, this dataset is used. It should be noted that these reactions do not involve suspending stem cells within the hydrogel as in actual stem cell therapy. Therefore, this procedure should be repeated using data sets that explore cell suspension in the hydrogel and its impact on fluid properties.

3.5.2 Rheology

There are three runs of this heparin sulphate-based gelation reaction. The rheometer used was an **AR-1500** (TA Instruments, USA) and a 20mm **parallel plate** geometry was used to characterise the fluid. The type of test performed was an **oscillatory** test that provides loss and storage moduli data over time. Looking back at Section 2.5.1, the test involves applying a sinusoidal strain and recording the stress response. The test was carried out at a constant temperature of **25°C**, strain of **2%**, and frequency of **1 Hz**.

For a viscoelastic fluid, there is a phase shift between the stress and strain, which is used to calculate the loss and storage moduli. The phase shift is due to the relaxation time of the fluid, and as stress is applied, the material responds gradually over time until equilibrium is reached. The loss modulus represents the fluid's viscous component, while the storage modulus represents its elastic component. These moduli are used to calculate the complex modulus and, using the angular velocity, to compute complex viscosity. The gelation reaction can be visualised in Figure 24 below. Initially, the mixture is a liquid, as indicated by the loss modulus being higher than the storage modulus. At approximately 400 seconds, the storage modulus surpasses the loss modulus, causing the mixture to behave as a gel.

The different parameters mentioned describe the following:

- **Strain** is of the form $\lambda = \lambda_0 \cdot sin(\omega \cdot t)$,
- **Stress** lags behind strain as $\sigma = \sigma_0 \cdot sin(\omega \cdot t + \delta)$,

where ω is the angular velocity of the rheometer and δ is the phase angle which represents the phase difference between the two parameters above.

- **Loss modulus** is computed using stress, strain, and the phase angle as $G'' = \frac{\sigma_0}{\lambda_0} \cdot sin(\delta)$,

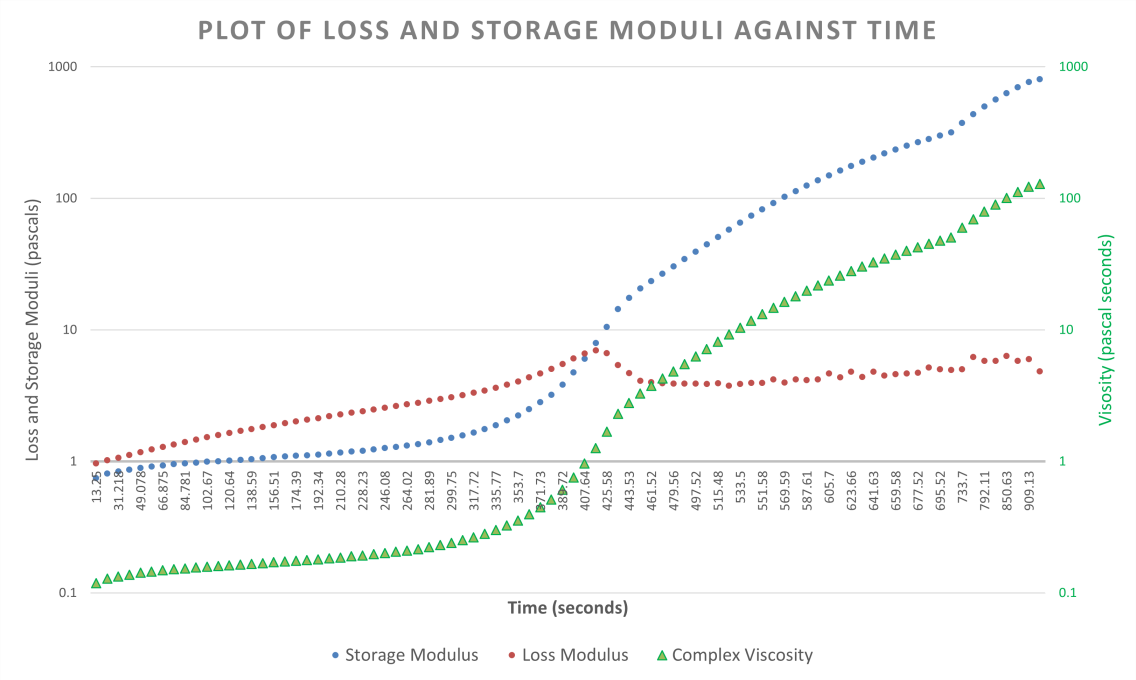

Figure 24: Plot showing the cross-over between loss and storage moduli as well as the variation of complex viscosity over time as gelation occurs.

- **Storage modulus** is similarly computed as $G^{'} = \frac{\sigma_0}{\lambda_0} \cdot cos(\delta)$.

Using these two parameters, one can then compute:

- **Complex modulus** as $G^* = (G^{'2} + G^{''2})^{0.5}$,
- **Complex viscosity** as $\eta^* = \frac{G^*}{\omega}$.

3.5.3 Material model

It is hypothesised that the majority of losses occur when the hydrogel transitions from liquid to gel. Figure 24 shows the first 400 seconds where the loss modulus exceeds the storage modulus until their curves intersect. It is essential to point out that the viscosity varies over time under a constant shear rate. Keeping this in mind, the following section will provide the basis for modelling the PEG within Ansys Polyflow.

As PEG gels over time, the full volume may not gel equally. This may occur due to variations in temperature or chemical concentration. This situation leads to a mixture of viscoelastic gelled PEG and Newtonian liquid PEG. Therefore, modelling PEG to a high level of accuracy requires considering it as a two-phase flow regime.

To avoid this level of complexity in the first instance of gelation modelling, the mixture of PEG is modelled as a single phase.

For a purely viscous fluid, the response of the stress to an applied strain results in a phase angle of 90 degrees. As the phase angle deviates far from this value, the fluid's elasticity becomes significant. Therefore, a viscoelastic model is necessary to capture the fluid's elastic effects as it flows. Figure 25 below illustrates how the phase angle varies while the mixture is in its liquid phase. The data was truncated to show the liquid phase of the hydrogel before the mixture transformed into a gel. The values indicate that the phase angle is well below 90 degrees; thus, one would ideally need a viscoelastic model.

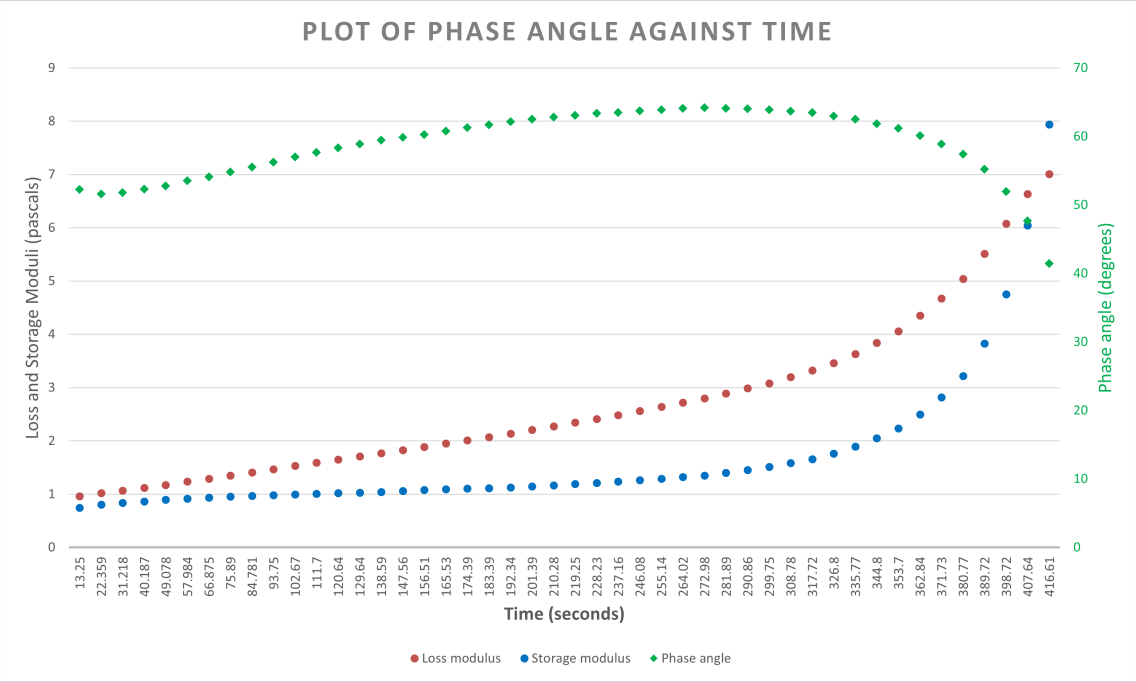

Figure 25: Plot showing the variation of phase angle against time while the fluid is in the liquid phase.

Using a viscoelastic material model and including the effect of gelation presents complexity. Therefore, it is ideal to develop the material model using a viscous material model. This can be justified by using a specific dimensionless number called the **recoverable shear**. It is similar to the Weissenberg number that can evaluate the viscoelastic nature of the flow. The ANSYS Polymat [60] user guide indicates that the Weissenberg number is not an effective indicator for viscoelastic flows with shear thinning. Looking back at Section 2.2.1, PEG exhibits shear thinning behaviour.

Therefore, the recoverable shear (Sr) is used and is defined as follows:

$$Sr = \frac{N_1[\dot{\gamma}]}{2\sigma_{xy}[\dot{\gamma}]}\,, \tag{7}$$

where N_1 is the first normal stress difference and σ_{xy} is the steady shear stress. Shear stress data is already available from the rheology data. The first normal stress difference is the difference between the first and second normal stress components of the stress tensor, T_{11} and T_{22}. This can be found using an empirical rule proposed by Laun [61] which uses the loss and storage moduli as follows:

$$N_1(\dot{\gamma}) = 2G^{'}[1 + (\frac{G^{'}}{G^{''}})^2]^{0.7}\,. \tag{8}$$

This empirical rule is preferred over the Cox-Merz rule [62] for the normal stress difference ($N_1(\dot{\gamma}) = 2G^{'}(\omega)$), which is valid over limited shear rates. According to the Polymat user guide [60], the rule proposed by Laun is valid for polyethylenes. This is suitable for the case of PEG as it is a polyethylene itself. Using this rule and the steady shear stress data available, one can calculate the recoverable shear while the mixture remains a liquid.

The recoverable shear gives an idea about the elasticity of the flow. If it is greater than 1, then the flow is considered viscoelastic and requires an appropriate model. However, looking at Figure 26 below, Sr is below 1 for the majority of the time the mixture is a liquid. Even at the cross-over point, it remains slightly above 1. In contrast, the Sr reaches a value of about 1,000 at 560 seconds and continues to further reach a value of 10,000 at 670 seconds. At the cross-over point, an Sr value of about 1.8 is negligible compared to the much higher values seen later in gelation.

This can be used to reasonably justify that, while the mixture is a liquid, it can be modelled as a viscous fluid. The viscosity change can then be modelled as a **time-dependent** viscosity, which can be implemented in ANSYS Polyflow as a user-defined function when defining material parameters. It is important to note that the cross-linker used exclusively affects gelation, and the shear rate does not; therefore, the time taken to reach gelation will not change irrespective of changes in the shear rate. This indicates that the change in viscosity over time will be similar for other shear rates, with scaled results for stress. This also depends on the type of model used for the viscous fluid.

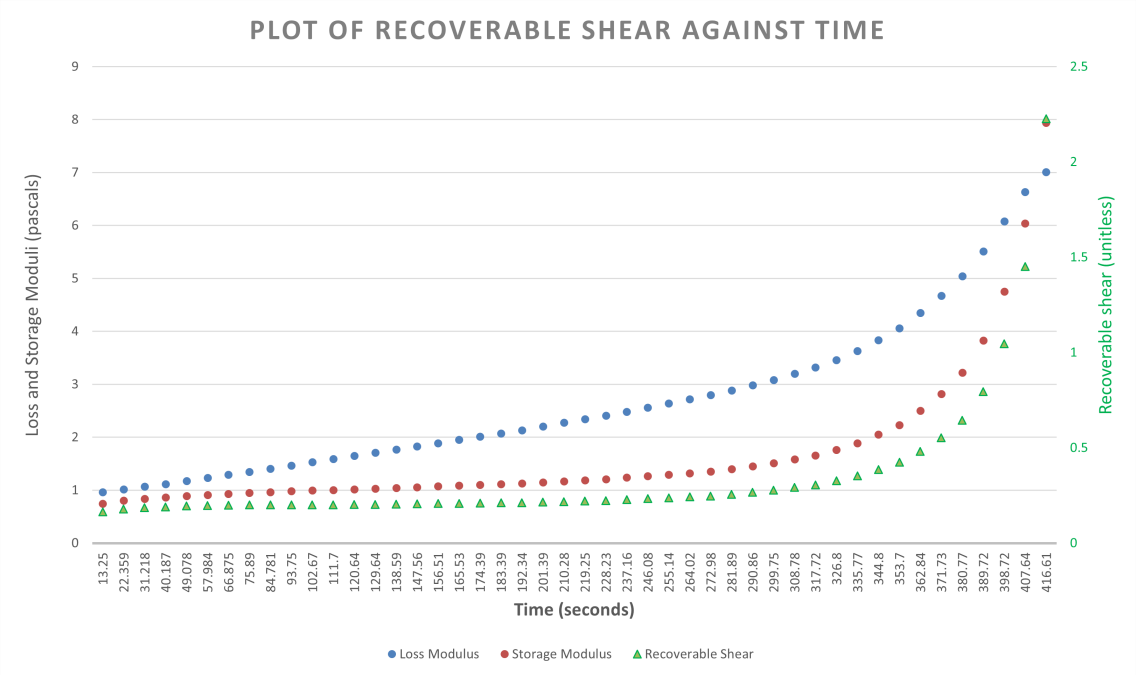

Figure 26: Plot showing the recoverable shear against time while the mixture is in the liquid phase.

3.5.4 Time-dependent viscosity curve fitting

The viscosity data that can be computed from the rheology data is the complex viscosity, η^*. This needs to be converted to shear viscosity, which is the material parameter to be used as an input into Polyflow. There is an empirical correlation, the Cox-Merz rule [62], that states that for low shear rate ranges, the complex viscosity as a function of angular velocity is equivalent to the shear viscosity as a function of the shear rate. More simply put: $\eta^*(\omega) = \eta(\dot{\gamma})$. Therefore, the complex viscosity computed from the rheology runs can be equated to shear viscosity. Complex viscosity was calculated for each of the three gelation reaction runs. The variation between each of the runs can be seen in Figure 27.

Polyflow allows parameters to have time dependence. Once the start and end times of the transient simulation are specified, the user can control how a parameter behaves between that time. The parameter in this case is viscosity, and it is modelled as $\eta(t)$. The experimental data in Figure 27 can then be used to fit a curve. Once an appropriate fit is obtained, it can be used as an input to outline the behaviour of the viscosity over the period of interest.

Two methods were used to fit a curve to the data. The first method used **ridge**

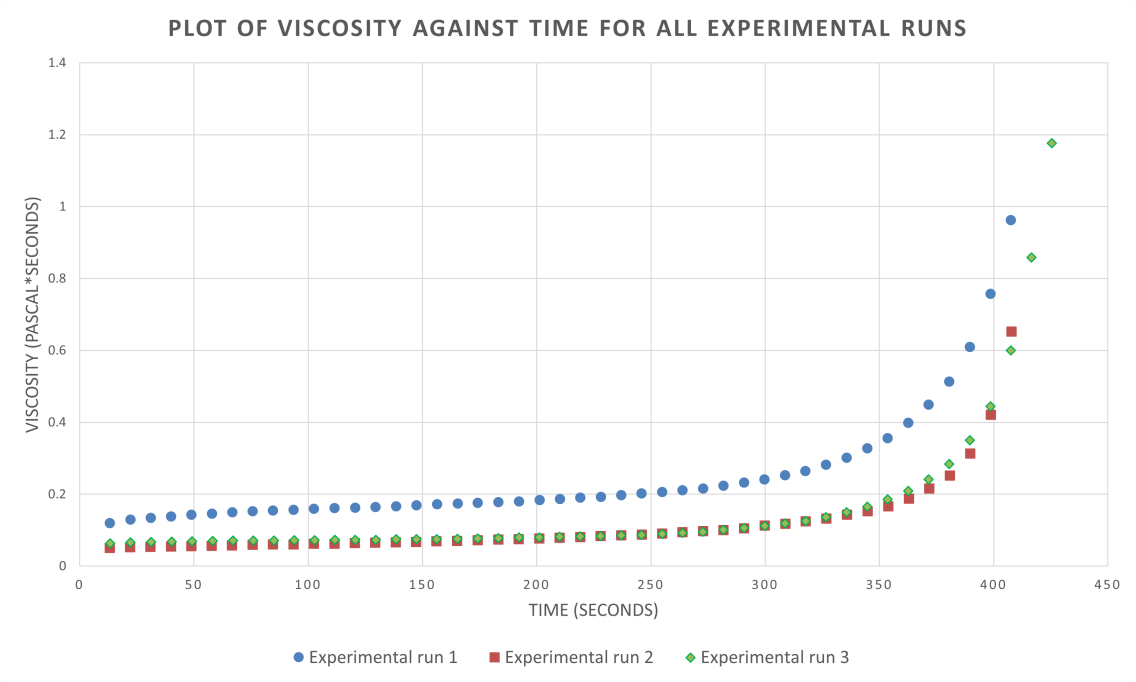

Figure 27: Plot showing the variation of viscosity against time for all experimental runs.

regression to generate a polynomial. This was done using the scikit-learn library, which is a machine-learning library for Python. Polynomials of increasing order were generated and compared with each experimental run. The measures used for the comparison were the **R-sqaured** (R^2) and the **mean squared error** (MSE). The order of the polynomial was increased until the values of R^2 and MSE levelled out at constant values. This method resulted in a **6th**-order polynomial. The error between this and the experimental runs is shown in Table 2.

Experiment	R-squared	Mean squared error
Experiment 1	0.6688	0.0093
Experiment 2	0.7612	0.0028
Experiment 3	0.9573	0.0019

Table 2: Comparison between the 6th-order polynomial and the experimental runs

The equation for the sixth-order polynomial can be written as:

$$\eta(t) = a + bt + ct^2 + dt^3 + et^4 + ft^5 + gt^6 \,, \tag{9}$$

where **a = 0.122**, **b = -3.58e-3**, **c = 9.31e-5**, **d = -9.72e-7**, **e = 4.84e-9**, **f = -1.14e-11**, and **g = 1.03e-14**. The behaviour of this polynomial compared to the experimental runs can be visualised in Figure 28 below.

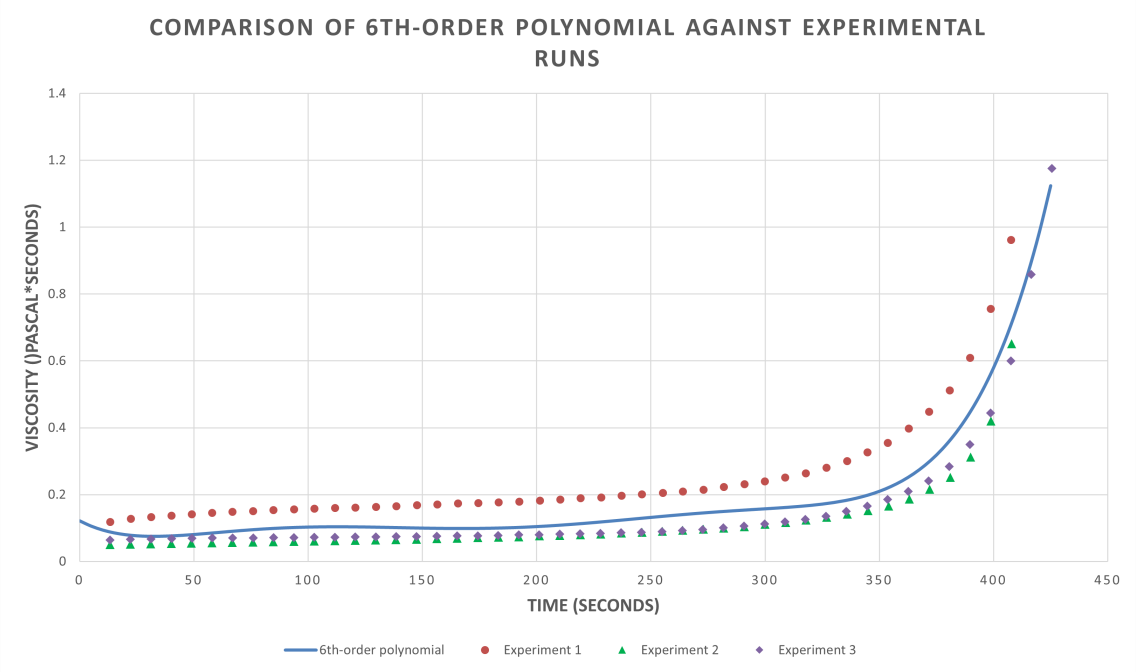

Figure 28: Plot showing the comparison of the 6th order polynomial against all experimental runs

The second method used **exponential curve fitting** to fit an exponential curve to the data. This was done using the SciPy library in Python, which is designed for scientific computing. The **scipy.optimize** sub-package was used specifically for the curve fitting. The curve to fit is of the form:

$$\eta(t) = ae^{bt} + c\,, \tag{10}$$

where a,b, and c were first estimated using a graphing tool. These estimates served as inputs to the curve fitting function, and the optimised parameters are obtained as **a = 2.85e-6**, **b = 0.030**, and **c = 0.107**. Table 3 shows the fitting error compared to experimental runs, and these are visualised in Figure 29.

Experiment	R-squared	Mean squared error
Experiment 1	0.6627	0.0095
Experiment 2	0.7348	0.0031
Experiment 3	0.9552	0.0020

Table 3: Comparison between the exponential fit and the experimental runs

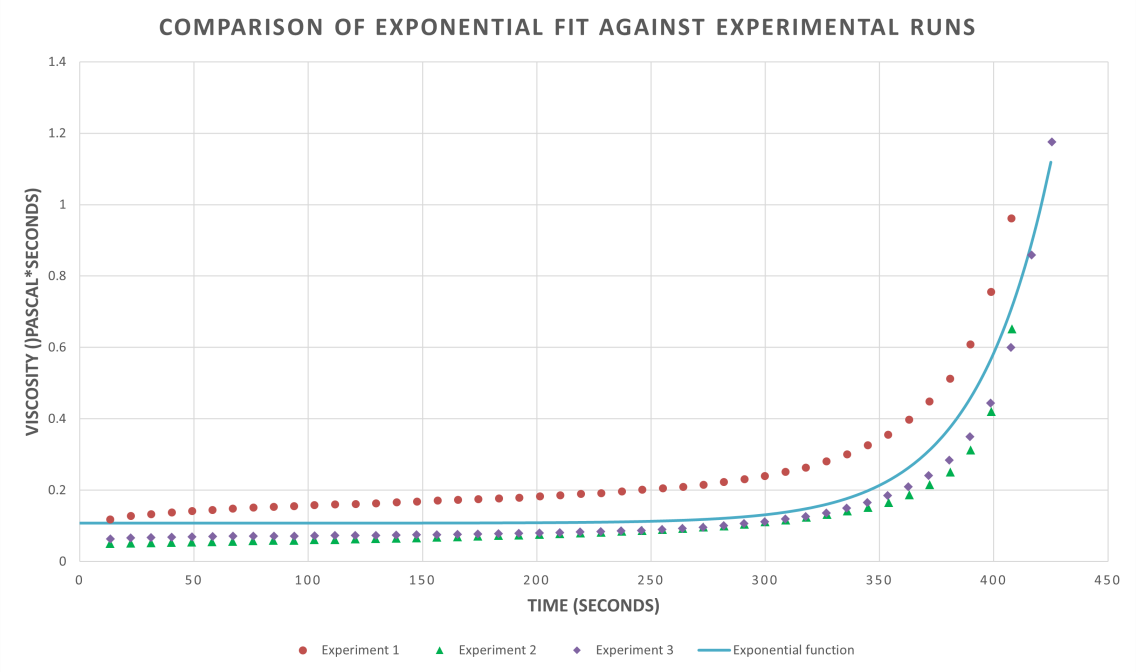

Figure 29: Plot showing the comparison of the exponential fit against all experimental runs

Comparing the two methods, the second method is a better choice to model the behaviour of the viscosity variation. Although the first method has better MSE values, the difference is negligible. The behaviour of all the experimental runs is indicative of exponential behaviour, and it makes logical sense to model it as such. Therefore, when implementing this behaviour in Polyflow, it will be modelled using the exponential fit.

3.6 Parametric analysis of a 2D idealised microfluidic geometry

Table 4 below summarises all 2D computational studies performed using the 2D geometry in Section 3.3.1.

Name	Model type	Viscosity ($Pa \cdot s$)	Boundary condition
Constant viscosity studies			
CV-grid-ind *Section 3.6.1*	steady-state	1	Traction boundary: $f_n = 15000\ Pa$
CV-diff-trac1 *Section 3.6.2*	steady-state	1	Traction boundary: f_n =10 Pa, $v_s = 0\ m/s$
CV-diff-trac2 *Section 3.6.2*	steady-state	1	Traction boundary: f_n =10 Pa, $f_s = 0\ Pa$
CV-param-trac *Section 3.6.4*	steady-state	1	Traction boundary: f_n =5000-175000 Pa
CV-lin-ver *Section 3.6.4*	transient	1	Traction boundary: $f_n = 0.15cos(\pi \cdot t)$ +0.4 Pa
Ramp viscosity studies			
RV-cons-trac *Section 3.6.2*	transient	$\mu = 0.09t + 0.1$	Traction boundary: f_n =10 Pa
RV-per-trac1 *Section 3.6.2*	transient	$\mu = 0.09t + 0.1$	Traction boundary: $f_n = 0.15cos(\pi \cdot t)$ +0.2 Pa
RV-per-trac2 *Section 3.6.2*	transient	$\mu = 0.09t + 0.1$	Traction boundary: $f_n = 0.15cos(\pi \cdot t)$ +0.4 Pa
RV-POC-cons *Section 3.6.5*	transient	$\mu = 0.09t + 0.1$	Inlet: v_n =1 m/s
RV-POC-ramp *Appendix D*	transient	$\mu = 0.09t + 0.1$	Inlet: v_n = t+1 m/s
RV-POC-per *Appendix D*	transient	$\mu = 0.09t + 0.1$	Inlet: v_n = cos(7t)+1.1 m/s
Other studies			
Param-visc *Section 3.6.3*	steady-state	0.1 - 1.2	Traction boundary: $f_n = 15000\ Pa$

Table 4: Summary of all 2D computational studies done.

The naming convention for the studies is as follows: the studies that use a constant viscosity begin with the suffix **CV** and those that use a ramp viscosity (time-dependent viscosity) begin with **RV.** All studies are **axisymmetric** and use a density of **1200 kg/m^3**. For all studies where traction is specified on the traction boundary, both the inlet and outlet are set as outflows. All transient studies use the implicit Euler method for integration and a variable time-stepping regime. All studies use the same values for the initial, minimum, and maximum time-step values detailed in Table 5. Each parameter is chosen for the following reasons:

- **Inital timestep value** - This is chosen to allow the solution to converge quickly at the beginning of the simulation. When using a gelling material model, there is an initialisation phase that takes place at the start of the solution (the effect of this can be seen in Figure 64). Once that is complete, the numerical solution tracks an analytical solution accurately.
- **Minimum timestep value** - When a value higher than this is used, the solver does not run successfully. The value was chosen by decreasing it until it resulted in the solver running successfully.
- **Maximum timestep value** - This is chosen to allow the timestep value to increase whenever the solver requires it to reduce computational expense.

All transient studies are performed for a duration of 10 seconds.

Time step parameter	Value (s)
Initial value of the timestep	0.001 s
Minimum value of the timestep	0.0001 s
Maximum value of the timestep	0.01 s

Table 5: Time step paramters for all 2D transient studies.

3.6.1 Grid independence study (CV-grid-ind)

A grid independence study is initially conducted to ensure that the other studies that follow are grid independent. This is performed using the geometry discussed earlier in Section 3.3.1. The studies that follow investigate the effect of applied traction on a fluid domain and its observed flow rate. Therefore, it is necessary to ensure that the mesh is sufficiently refined so that for different applied tractions, the mesh count does not affect the flow rate. Furthermore, while investigating the 2D domain, the decision was made to analyse the average velocity observed. The flow rate is dependent on the outlet area and the average velocity at the outlet. Since the outlet area remains consistent, it can be ignored, and the focus can be shifted to the average velocity.

Table 6 highlights the element sizes used and the resulting mesh count. Steady-state simulations are run with an applied normal traction and an arbitrary viscosity. The resulting average velocity at the outlets is analysed.

Element size (μm)	Mesh count
7	8500
4	26,000
3	45,000

Table 6: Preliminary mesh information.

In the second phase of the grid independence study, the outlet was examined further. Given the importance of the outlet in determining grid independence, the region closer to the outlet was refined compared to the overall domain, as shown in Figure 30. The refinement is carried out in ANSYS Meshing, where the outlets are chosen and mesh refinement is implemented with a refinement level of 3.

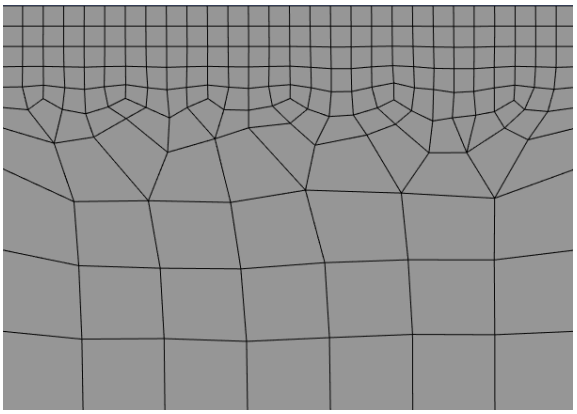

Figure 30: Illustration of the refined edge mesh.

Using the same element sizes from the preliminary grid independence study, new meshes are generated and used with the same simulation parameters. The mesh information for these meshes can be found in table 7. The results of this analysis can be found in Section 4.1.1.

Element size (μm)	Mesh count
4	26,500
3	45,400

Table 7: Refined mesh information.

3.6.2 Preliminary analysis using the traction boundary condition

3.6.2.1 Different traction boundaries (CV-diff-trac1, CV-diff-trac2)

Looking back at Section 3.4.1, there are two ways of imposing a normal traction on a domain; (f_n, v_s) and (f_n, f_s). An analysis is required using both boundary conditions to determine which is appropriate. Both can be used to apply normal traction onto the boundary; however, setting the tangential component to f_s or v_s may lead to a difference in the results. An arbitrary 2D axisymmetric domain, similar to the one in Figure 20, is used for the analysis with a radius of **2mm** and a length of **40mm**. This is chosen such that there is sufficient length along the flow domain to allow the flow to develop fully. An arbitrary normal traction is also applied to the domain.

The mesh used for this preliminary analysis is refined in a way that is suitable for analysing Hagen–Poiseuille flow. The mesh refinement strategy is implemented in the following manner: For a fully developed, steady-state, Hagen-Poiseuille flow case, the maximum velocity observed at the outlet is twice the average velocity at the inlet. A steady-state simulation is set up to replicate Hagen–Poiseuille flow with a specified inlet velocity. The maximum velocity at the outlet is noted and the mesh is refined until the maximum velocity is double that of the inlet velocity. This process confirms that the mesh is sufficiently refined for the analysis. The size of the elements used for the mesh is **50** μm and the total number of elements is **320,000**. Different boundary conditions are applied with specified normal traction, while the Neumann BC varies between shear traction and shear velocity. In both instances, the Neumann BC is set to 0. The results of this analysis can be found in Section 4.1.2.

3.6.2.2 Constant traction applied (RV-cons-trac)

To test the concept of time-dependent viscosity, a simulation is set up in which a constant traction is applied to the boundary. An arbitrary value is used for the constant traction that is applied to the domain. In this instance and for further analyses in this section, the viscosity increases significantly faster than the gelation model. In the gelation model, the viscosity increases from 0.1 $Pa\cdot$ to 1 $Pa\cdot$ over 400 seconds, while for these studies, the same increase occurs over a 10-second period. This approach reduces the computational expense of simulating a large time domain while still allowing for an appreciable difference in flow behaviour as a result of the viscosity change. The result of this simulation can be found in Section 4.1.2.

3.6.2.3 Periodic traction (RV-per-trac1, RV-per-trac2)

The analysis from the previous section can be extended so that a periodic traction BC is applied to the boundary. The reason for investigating such a BC is that the

final model is planned to be set up with a periodic BC. Therefore, it is necessary to investigate the use of periodic traction BCs and understand their limitations within the solver. Similarly to the previous section, a time-dependent viscosity is implemented.

In the first attempt, a periodic function was implemented for the BC as: $f_n = 0.15cos(\pi \cdot t) + 0.15\ Pa$. Errors arose from a divide by 0 issue as the traction approaches 0. To mitigate this, the periodic function is shifted in the y-axis so that it does not approach 0. Two traction BCs were set up, one closer to the x-axis than the other. The periodic functions are visualised in Figure 31. The results of these simulations can be found in Section 4.1.2.

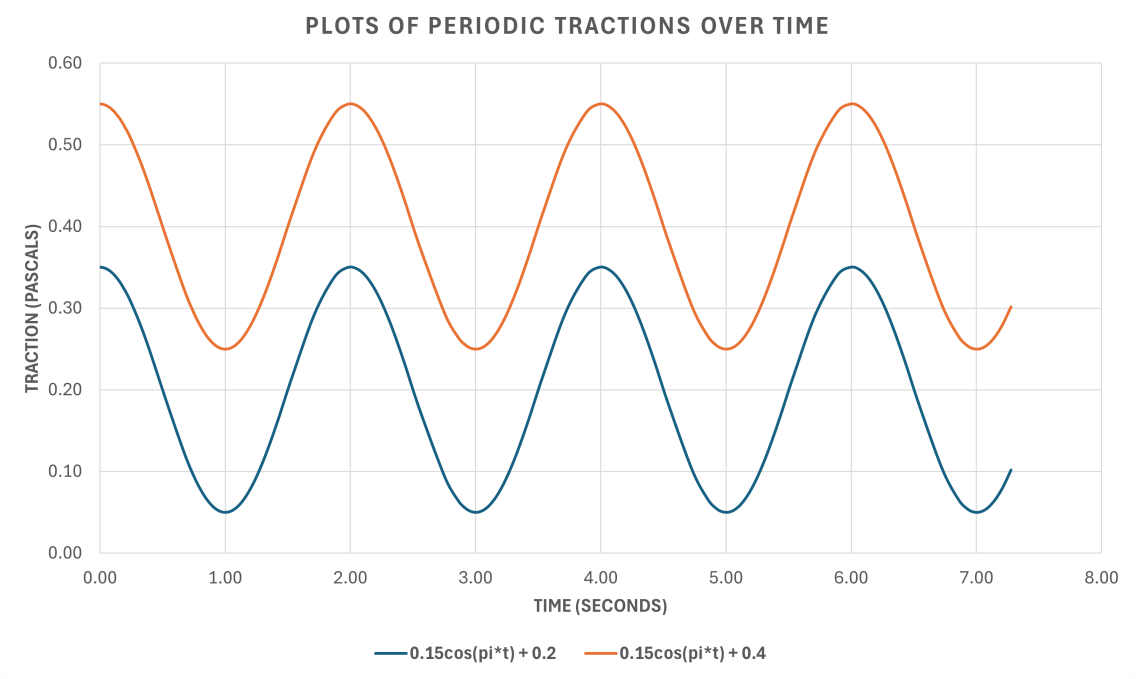

Figure 31: Plots of periodic traction functions over time.

It is still of interest to obtain results for a periodic function that has 0 or near 0 values. This can be achieved using the relationship between applied traction and observed average velocity. The analysis in Section 3.6.4 yields a linear relationship between the two parameters. This could potentially be used to determine the average velocity result for a periodic function that has 0 values. To prove this concept, the results of the above simulation are used, and the method is presented in Appendix A

3.6.3 Paramteric study on the effect of varying viscosity (Param-visc)

The mesh used for the parametric studies comes from the grid independence analysis conducted in Section 3.6.1. In this study, the normal traction applied remains constant, whereas the viscosity varies between the limits of viscosity for the gelation model. The traction used is much higher than that used in the latter simulations. The results still remain consistent when modelled with a lower traction. The results are presented in Section 4.1.3.

3.6.4 Paramteric study on the effect of varying traction (CV-param-trac, CV-lin-ver)

In this study, the viscosity remains constant while the traction varies. Similarly to Section 3.6.3, the range within which the traction varies is higher than what is expected in subsequent simulations. The same grid-independent mesh as the previous parametric study was used. A transient simulation with varying traction is also conducted. The results are presented in Section 4.1.4.

3.6.5 Proof of concept simulation (RV-POC-cons)

The studies in Section 3.6.2 utilise a time-dependent, constant viscosity model. The concept of a time-dependent viscosity model is theoretical and is implemented numerically using a solver. To this end, an analytical solution is derived which is manipulated to use a time-dependent viscosity. The analytical solution is used alongside numerical solutions from Polyflow and Fluent to evaluate their accuracy and performance. The details of this analytical solution can be found in Appendix B.

It is important to note that a 2D axisymmetric domain needs to be set up separately in Fluent and Polyflow. In Polyflow, the symmetry axis needs to be aligned with the y axis, whereas for fluent it needs to be aligned with the x axis. The same geometry and mesh described in Section 3.6.2 is set for each case. In Polyflow, the time-dependent viscosity is set using the *EVOL* option, which allows the use of preset functions to model time-dependent behaviours. In Fluent, the time-dependent viscosity is set by interpreting the code described in Appendix C.

The results are presented in Section 4.1.5. This analysis is further extended to test the performance and accuracy of the solvers for inlet velocities that vary linearly and periodically. Details of these analyses are provided in Appendix D.

3.7 Application to realistic 3D tissue structure

Looking back at the research aim stated in Section 1.2.2, the aim is to model the behaviour of PEG in myocardial tissue while it undergoes gelation. The gel is contained within passive infarct tissue and is subjected to stress from adjacent healthy tissue. This stress is taken up by both the infarct tissue and the gel. The gel is liquid and the stress imposed on it may result in significant flow out of the interstitial space in the tissue. This can be visualised in Figure 32 below.

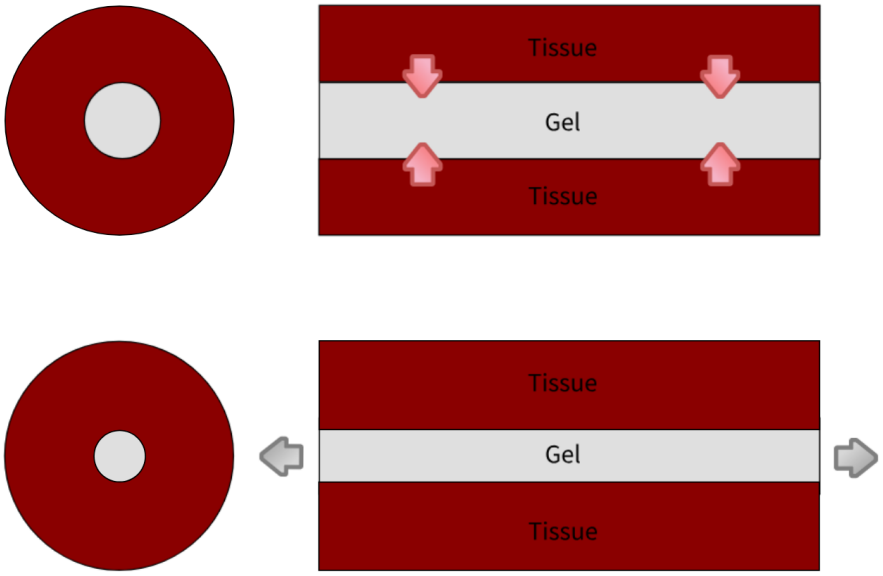

Figure 32: Illustration of myocardial tissue squeezing gel out of its interstitial spaces.

The illustration above shows how the tissue behaves during the contraction phase of the cardiac cycle. The varying stresses in the heart lead to deformations in the tissue structure, which in turn deform the interstitial space. This means that a fluid-structure interaction (FSI) model would ideally be needed to capture the changing shape of the domain. However, due to the constraints outlined in Section 1.3.2, a rigid CFD model is implemented in Ansys Polyflow.

The Polyflow model uses a traction boundary condition described in Section 3.4.1 to apply a normal traction to the boundary of the fluid domain. The application of such a boundary condition (BC) results in an outflow from all outlets specified in the domain. This observation aligns with the flow behaviour of a fluid domain present within a periodically moving solid domain. Maluleke [59] conducted FSI simulation case studies on biomaterial displacement caused by ventricular-induced myocardial deformation. The case study results indicated that setting all orifices as outlets leads to biomaterial flowing out of the fluid domain.

The presented model uses a periodic traction BC to simulate outflow from a fluid domain without modelling an external moving solid domain. Applying a time-dependent traction BC to the fluid domain, which varies during a single cycle, results in a variable flow rate out of the domain. This traction BC replicates the effect of the moving solid domain on the flow rate behaviour. This can be used with a fluid domain that undergoes a phase change to analyse the impact of changing the viscosity of a material as it exists within the myocardium.

The next thing to consider is the time interval over which the fluid domain will be modelled. Looking back at Section 3.5.3, the material model developed is valid for the case where recoverable shear is less than 1. Figure 33 shows the variation of recoverable shear over time for multiple gelation runs. Using a conservative approach, the farthest time is chosen, which is around 417 s. Therefore, a time interval of **0-417s** is chosen.

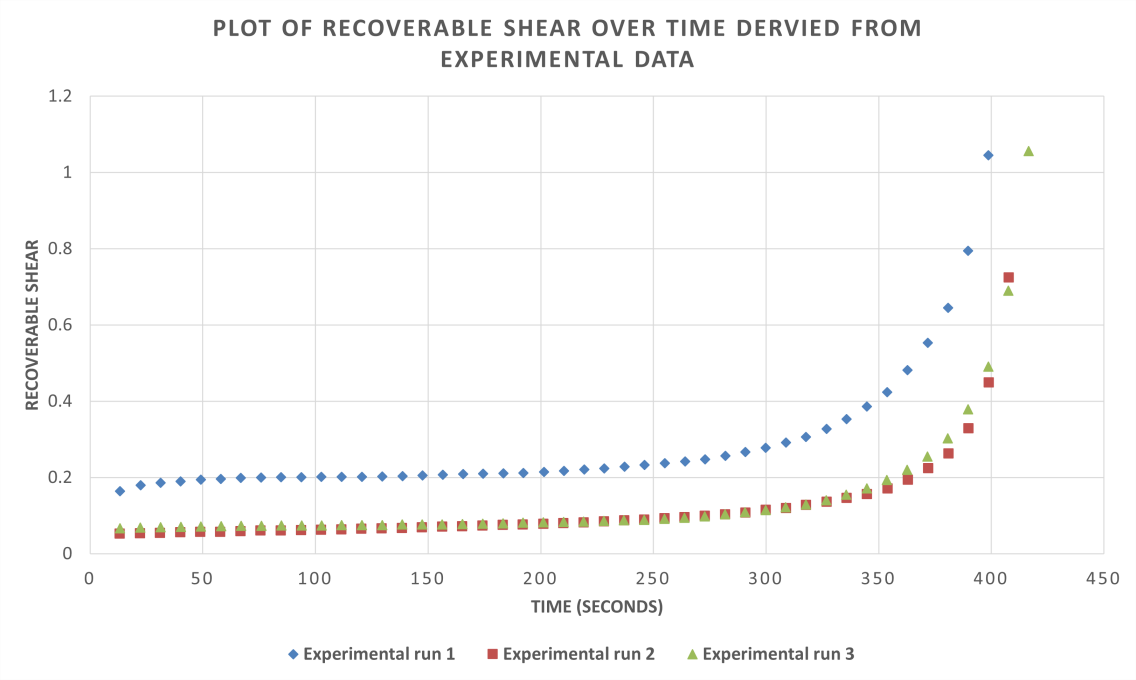

Figure 33: Plot of recoverable shear over time for multiple experimental runs.

The last thing to consider is the accuracy of the Polyflow model when compared with an FSI simulation. It is difficult to match the exact velocity flow field from the FSI simulation by Maluleke [59], and it is even more complicated to match the flow field for all relevant outlets. Figure 34 below shows the differences in the velocity contours between the FSI and Polyflow model. Therefore, the model is simplified

with the project objectives in mind, which aim to determine if losses occur during gelation. A parameter of interest is the volume lost per cardiac cycle. Instead of replicating the velocity flow field from an FSI simulation, one can instead replicate the overall volume loss in a single cardiac cycle. This can be more closely matched by using the Polyflow model and an appropriate traction boundary condition.

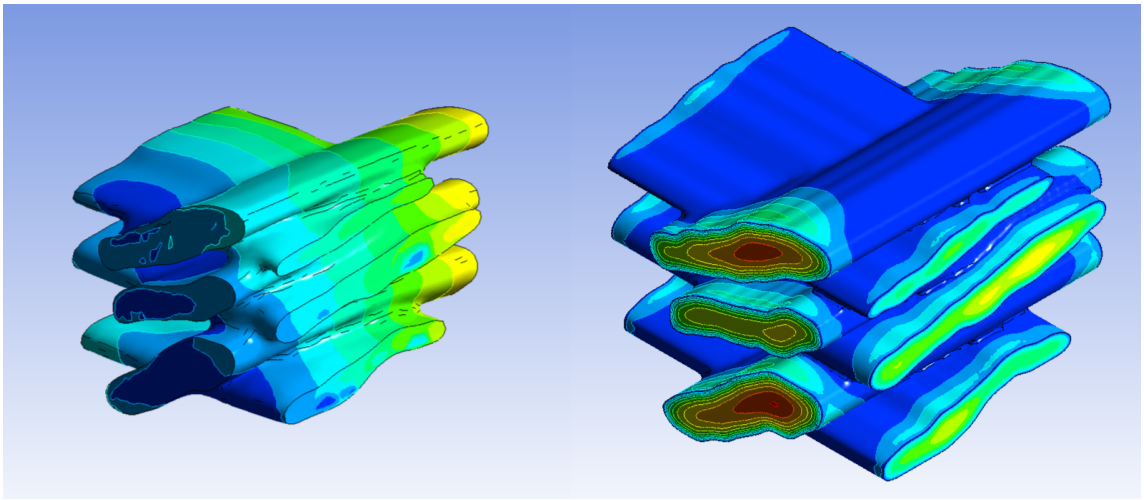

Figure 34: Velocity contours of the fluid domain showing the difference in the flow field between the FSI simulation (right) and the Polyflow model (left).

3.7.1 Analysis of relevant FSI results for input into 3D model

The FSI model set up by Maluleke utilised MpCCI (mesh parallel code coupling interface) to couple Abaqus and Fluent together. A myocardial infarct tissue block was modelled in Abaqus, and a third-order Yeoh model was used for the material model. The PEG fluid domain was modelled in Fluent, and a power-law model was used to describe the shear-thinning behaviour of PEG. The respective geometries can be seen in Figure 35. The modelling strategy that Maluleke implemented can be summarised as follows:

- An infarct microstructural tissue block is placed in the wall of a ventricle in an existing and validated rat biventricular (BV) model. Appropriate boundary conditions are applied to the BV model to replicate the deformation of the ventricles during a cardiac cycle.
- The nodal displacements of the tissue block mesh over time are generated during multiple cardiac cycles. This is used to replicate the deformation of the tissue block without the need to model the entire BV model, which is computationally expensive.

- The nodal displacements of the tissue block are used as an input boundary condition for the FSI model, where the tissue block is coupled to a fluid domain. Here, all orifices in the fluid domain are set to outlets.

Figure 36 below shows the strain variation of the tissue block during multiple cardiac cycles. It is worth highlighting the drift observed in the strain response as the minimum strain slightly increases over time. Therefore, the strain behaviour during the latter stages of the simulation is taken as the steady-state behaviour of the heart over a longer period.

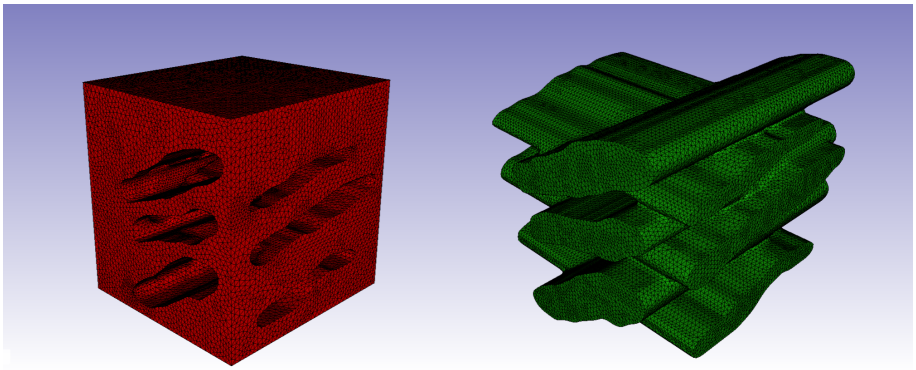

Figure 35: Meshes for the solid and fluid domain used for the FSI simulation

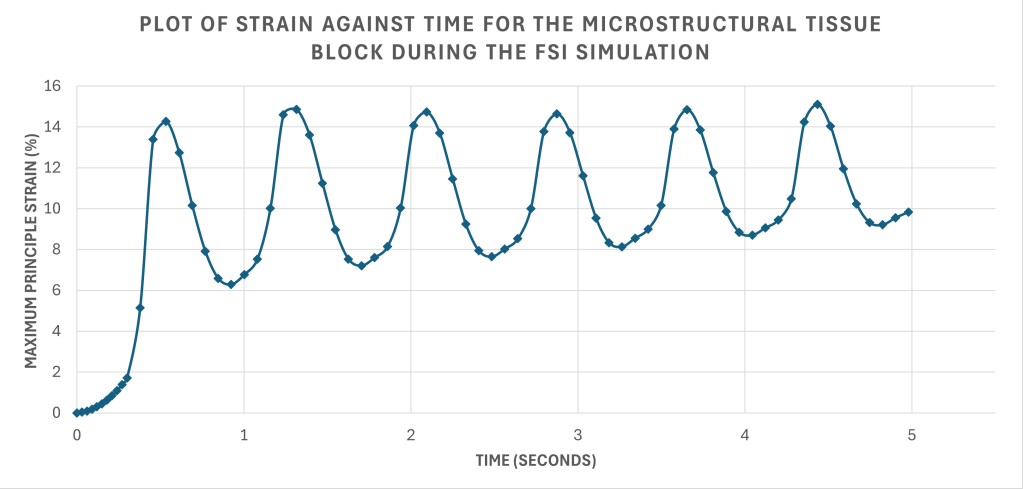

Figure 36: Plot of strain over time for the tissue block during the FSI simulation

The FSI results are used to analyse the total volumetric flow rate of PEG out of the tissue block. The results are available as discrete time steps and can be loaded into

CFD-Post for analysis. The flow rate behaviour is obtained per cycle, and the first cycle is ignored. This is because the first cardiac cycle includes a loading step and does not represent the steady-state behaviour of the heart. Figure 37 shows the flow rate behaviour of PEG over multiple cycles, demonstrating consistent behaviour.

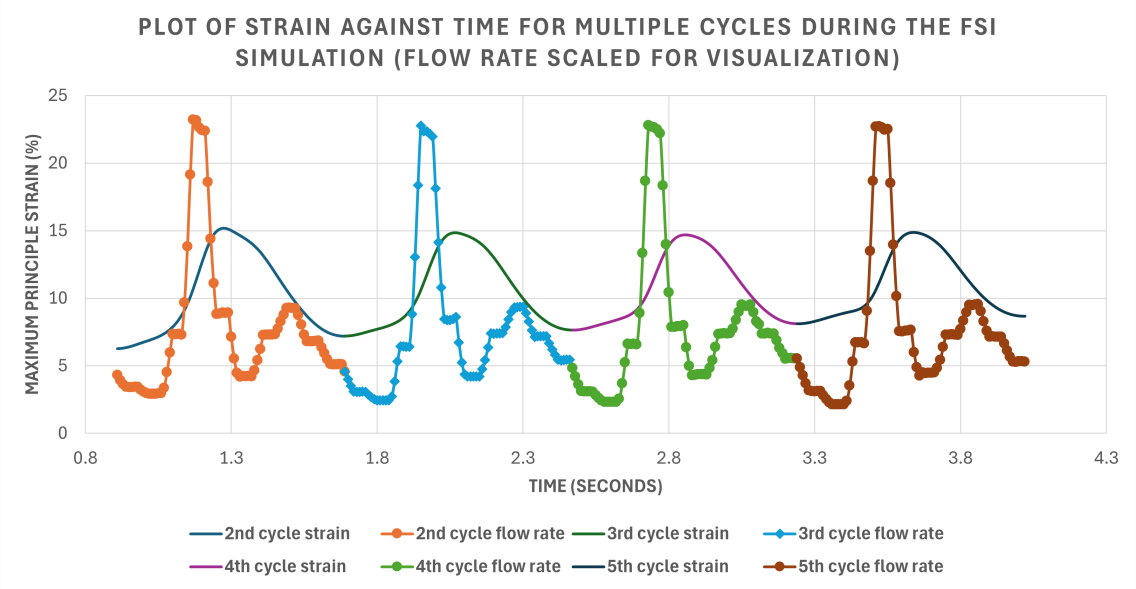

Figure 37: Plots of flow rate and strain over time for multiple cardiac cycles. The flow rate is scaled for visualisation purposes.

The area under each flow rate response is computed, showing the values converging onto a steady-state value as the simulation progresses. Table 8 shows the total volume lost per cycle. The converged value is taken as the volume loss per cycle when considering a longer duration for analysis.

Cycle	**Total volume out** $\times 10^{-2} mm^3$
2	1.19
3	1.17
4	1.16
5	1.16

Table 8: Volume lost per cycle in the FSI simulation.

3.8 Modelling the traction boundary condition

The traction boundary conditions described in the following subsections are applied in the Polyflow model as a UDF written in CLIPS. The expressions can be found in Appendix E.

3.8.1 Traction boundary condition 1

The model discussed here is taken from Motchon [56], who analysed the effect of varying the stiffness of the gel and its impact on tissue stress. The particular model obtained uses a gel that is much softer and therefore more similar to that of a liquid gel. It is important to note that even if it is a softer gel, it is still modelled as a solid in Motchon's work.

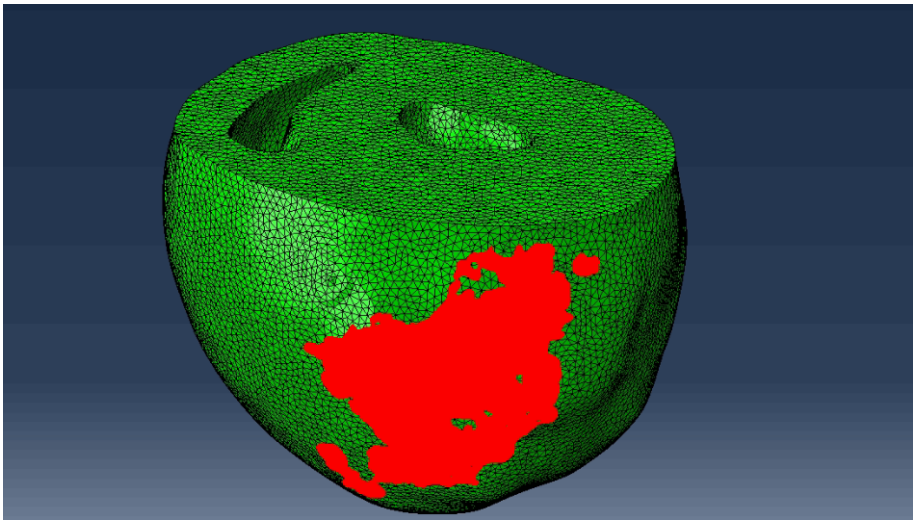

Figure 38: Mesh of the biventricular model analysed with the gel shown in red.

This boundary condition is developed with the idea that a traction boundary is used in the Polyflow model. The traction experienced by the gel, while present in the myocardium, may govern the resulting flow rate behaviour of PEG. Therefore, it is necessary to characterise the traction response. Figure 38 shows that the gel in the biventricular model covers a larger area than in the FSI model discussed earlier. Hence, it is essential to analyse different regions to note any variation in traction.

As shown in Figure 39, two regions are chosen for analysis. One region, near the top of the domain (region A), shows the presence of PEG in the upper section of the ventricle wall. Another region is selected near the bottom (region B), where PEG is present near the bottom of the ventricle walls. Varying numbers of elements are

chosen to highlight a variation. During the analysis, it was noted that choosing a smaller number of elements results in "uneven" behaviour. For context, the lower region is used to plot the traction response for 9,000 elements, whereas the upper region is analysed with 20,000 elements. This uneven behaviour is shown by the blue line in Figure 40.

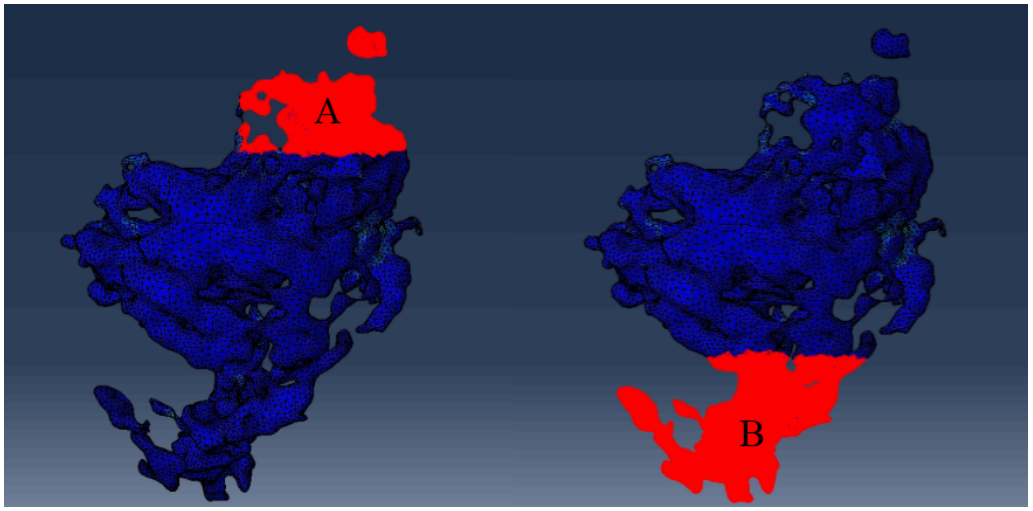

Figure 39: Meshes of the gel in the biventricular model showing the regions (in red) analysed at the top and bottom.

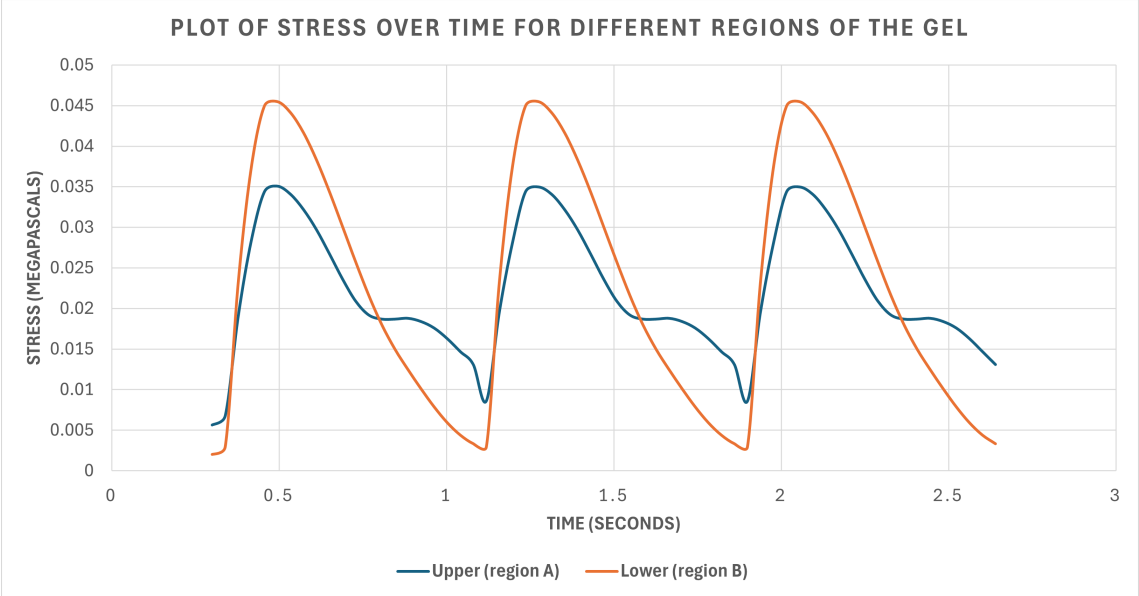

Figure 40: Plot of stress over time for both regions described in figure 39.

This behaviour itself also varies when different regions are analysed throughout the domain. However, when a larger number of elements is chosen, the responses "average" and a consistent behaviour emerges, as shown by the orange line in Figure 40.

Different regions are analysed because the heart's non-uniform structure results in location-dependent stresses. Figure 16, discussed in the literature review, shows larger stresses at the bottom of the biventricular model compared to the top. The musculature of the heart varies from top to bottom, with thicker musculature toward the bottom [63]. It is not just the thickness but also the fibre direction that gives rise to contractile activity [64]. This may lead to a difference in the traction that the myocardium exerts on the PEG depending on the location. As seen in Figure 40, the traction response of the gel sampled in a lower region experiences higher peaks.

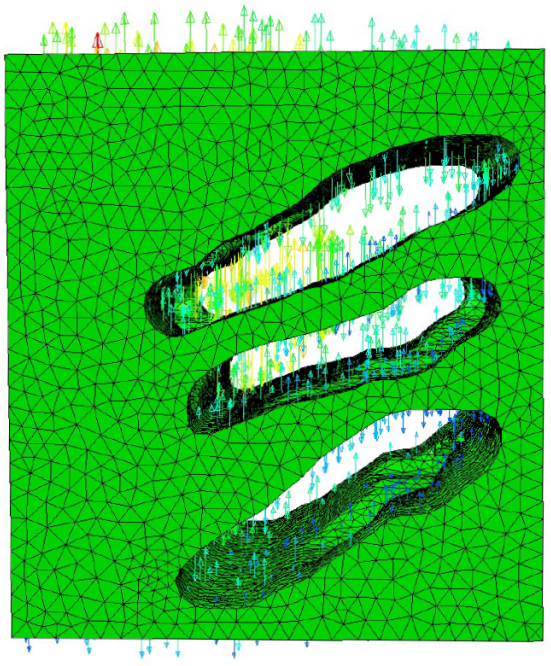

Figure 41: Normal stress vectors for the tissue block in a specific direction showing the variability in the stress vectors.

The traction response of the gel sampled with a larger number of elements is used, and a curve is fitted to the response. The details of the fit can be found in the Appendix F. Using this response directly in the Polyflow model leads to significantly higher flow rates compared to the FSI model. This is due to the uniform application of normal traction across the domain in the Polyflow model. In contrast, the FSI

model displays significant variability in the magnitudes of stress vectors within the tissue block. Figure 41 shows how the stress vectors vary.

Therefore, the traction response is scaled in the Polyflow model to match the volume loss per cardiac cycle in the FSI model. The details of this scaling process are explained in Section 3.8.4 later. Once the traction response is appropriately scaled, it can be used in the Polyflow model to observe the flow rate behaviour. From the analysis conducted in Section 3.6.4, it was observed that there is a linear relationship between the applied traction and the resulting flow rate. The resulting flow rate from this boundary condition can be seen in Figure 42. In this case, the area under the curve for both flow rates is the same, which shows that the same volume is lost per cycle.

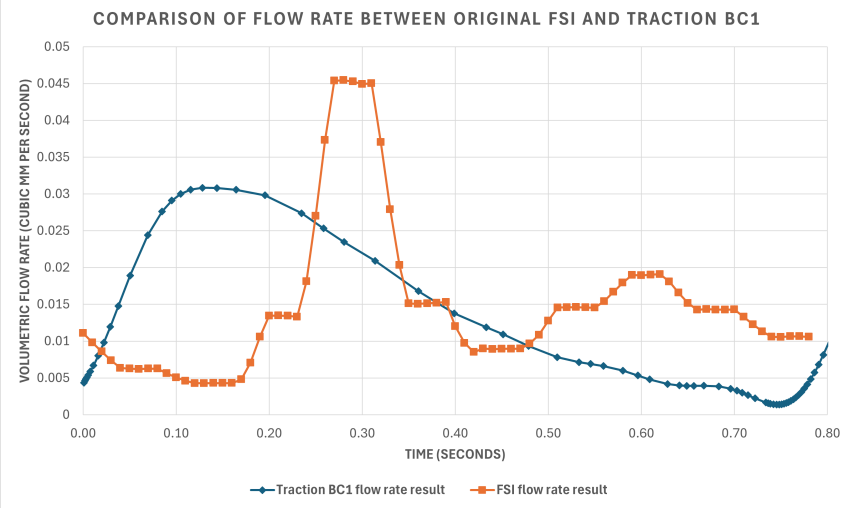

Figure 42: Plots of volumetric flow rate comparing the FSI result to the result obtained by using traction BC1.

There is a significant difference in the flow rate behaviour, which may give rise to different volumes lost per cycle when analysed over a longer period with a gelling material. To this end, a second traction boundary condition is developed.

3.8.2 Traction boundary condition 2

This method reverse engineers the boundary condition so that it results in a flow-rate behaviour that is consistent with the FSI model. From the analysis conducted in Section 3.6.4, it is noted that there is a linear relationship between the applied traction and the resulting flow rate. Therefore, the traction boundary can be modelled using the behaviour of the flow rate response.

The flow rate behaviour from the FSI simulation is used and a curve is fitted to the response. The details of the fit can be found in Appendix F. A similar scaling process is used to scale the function so that throughout a cardiac cycle, the volume lost per cycle is matched. Figure 43 shows a close match between the flow rates derived from the Polyflow and FSI models.

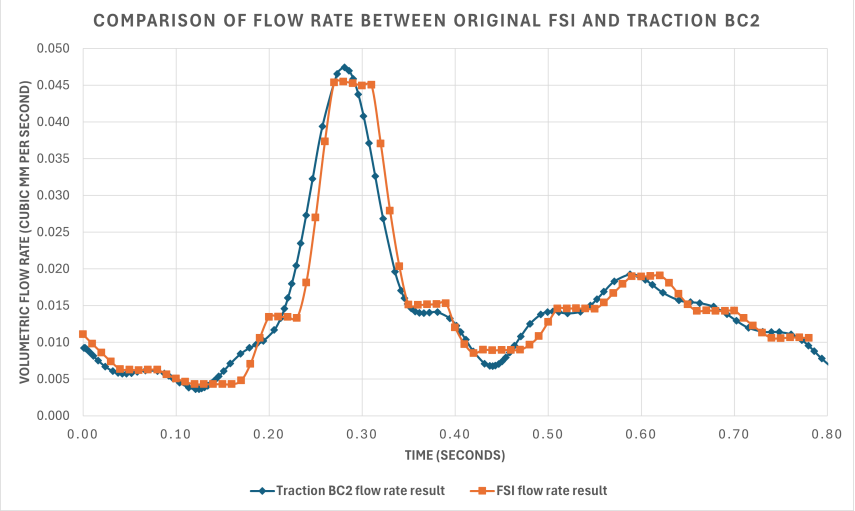

Figure 43: Plots of volumetric flow rate comparing the FSI result to the result obtained by using traction BC2.

3.8.3 Traction boundary condition 3

Upon closer inspection of the flow rate behaviour over multiple cycles in Figure 37, a specific correlation is observed. Through visual inspection, it is evident that a relationship exists between the gradient of the strain response of the tissue block and the flow rate of the gel. This correlation is further investigated.

Due to the slight variation in the strain discussed earlier in Section 3.7.1, the last two strain cycles serve as the steady-state response of the strain. A curve is fitted to the strain response. This expression is differentiated to obtain the gradient of the strain response and the absolute value of the gradient is taken over time. This can be seen in Figure 44. This agrees with the visual inspection mentioned earlier and is used to model the traction boundary condition. In the last two boundary conditions, the resulting flow rate never drops to zero during the cardiac cycle. Therefore, the absolute gradient response is modified so that the minimum flow rate does not reach 0. The absolute gradient response is scaled to match the FSI model's single-cycle volume loss. Figure 45 shows the variation in the flow rate using this boundary condition.

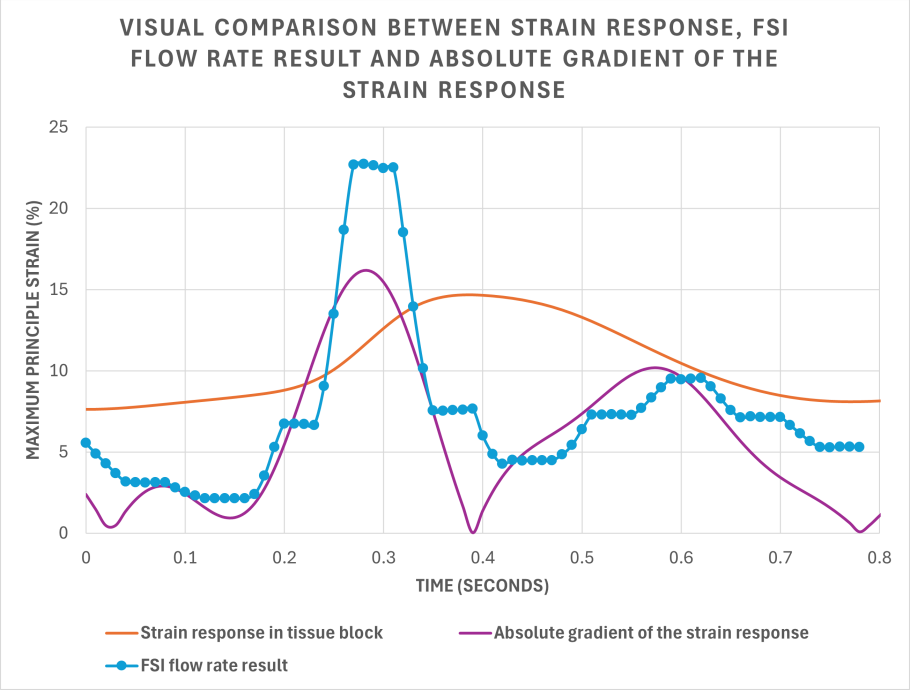

Figure 44: Visual comparison of the strain during the last cycle with its absolute gradient. The original FSI result is also included.

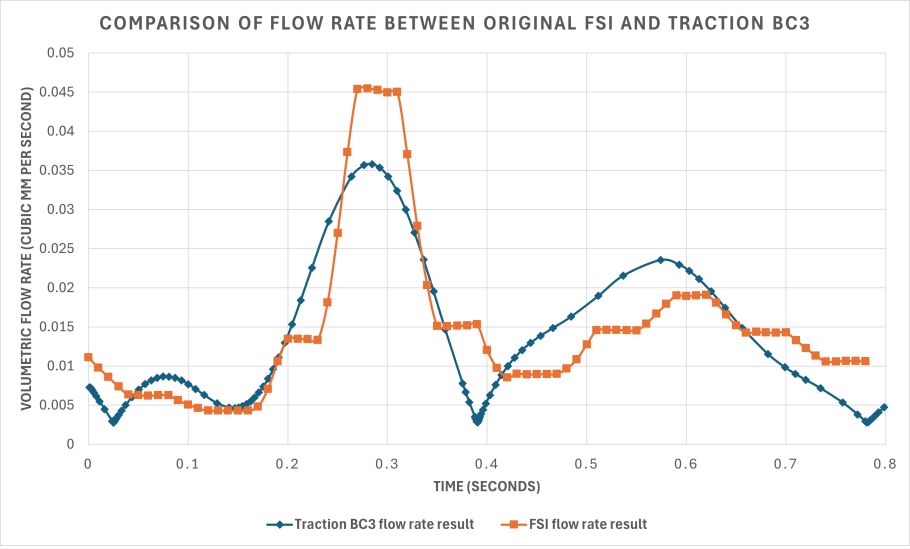

Figure 45: Plots of volumetric flow rate comparing the FSI result to the result obtained by using traction BC3.

3.8.4 Scaling procedure

The scaling procedure follows the logic that there is a linear relationship between the applied traction and the observed flow rate. Thus, the area under a flow rate curve, representing volume, is linked to the applied traction. The goal is to match the volume lost per cycle in the FSI simulation detailed earlier in Table 8. The scaling factor used to multiply the traction expression can be adjusted linearly. This is done until the flow rate results using Polyflow match the volume lost in the FSI simulation.

It is important to highlight the differences in the setup between the Polyflow and FSI models. The Polyflow model uses a Newtonian material model whose viscosity changes with time. The FSI model employs a shear-thinning power law material model with parameters $k = 0.01Pa \cdot s^n, n = 0.701$. Therefore, it is necessary to find a way to match the material models so that the results from both can be correctly compared. For a power-law model, when $n = 1$, the model reduces to a Newtonian fluid model with the consistency index being the apparent viscosity. This is implemented in the Polyflow model as a constant viscosity and is used in conjunction with the traction BCs to generate a comparable flow rate result.

The scaling procedure is demonstrated using the traction BC described above in Section 3.8.2 (BC2). The Polyflow model uses the Fourier series as a traction boundary to obtain a flow rate response. In the first instance, a scaling factor of **1** multiplies the Fourier series, and the volume lost over a cycle is obtained as $\mathbf{7.94 \times 10^{-4} mm^3}$. Given that the target volume lost is $\mathbf{1.16 \times 10^{-2} mm^3}$, the ratio between the two volumes can be obtained as:

$$\frac{1.16 \times 10^{-2}}{7.94 \times 10^{-4}} = 14.6\,. \tag{11}$$

The Fourier series can then be multiplied by this ratio and reused in the Polyflow model to obtain a subsequent flow rate. The area under the new flow rate response closely matches the target volume lost in the FSI model. This traction BC can now be regarded as the effect of the moving myocardium on the flow behaviour of PEG and be used in conjunction with a gelling material model.

This scaling procedure works well when the ratio between the first volume used and the target volume falls within a relatively small range. In the case of BC1 described in Section 3.8.1, the function is an order of magnitude higher than the function for traction BC2. The same scaling procedure was applied to it to obtain the ratio used to scale the function. That ratio was used to scale the Fourier series and the scaled function was reused in the Polyflow model. When the subsequent flow rate

response and the respective volume loss were obtained, it was discovered that it did not converge onto the desired volume. However, when the new volume was used with the target volume to obtain a new scaling factor, the resulting traction BC successfully worked, and the volume converged onto the target volume.

Figure 46 illustrates the relationship between the two parameters during the simulation. Initially, the relationship is perfectly linear, after which it fluctuates around the initial consistent value. This explains the issue faced with the BC1 scaling procedure, where the ratio between the generated volume and the target volume is large. This fluctuation may stem from inertial effects since these effects are taken into consideration when setting up a transient simulation. Nevertheless, as the scaling procedure is iteratively applied, the volume lost per cycle converges towards the target volume.

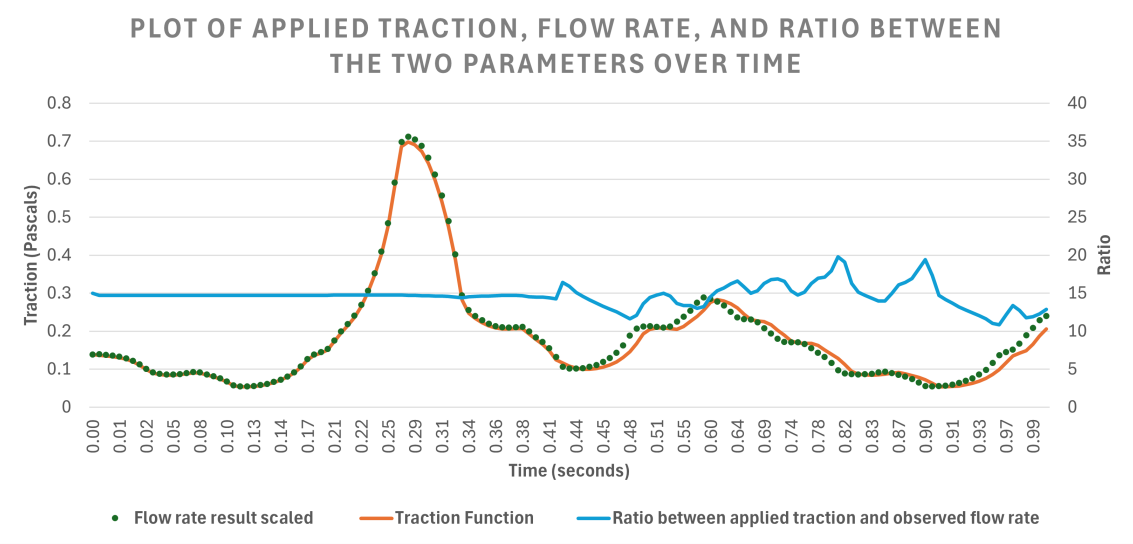

Figure 46: Plot of traction over time with the scaled flow rate response and ratio of the two parameters during the simulation.

3.9 Analysis of a 3D microstructural domain

Tables 9 and 10 summarise the 3D computational studies performed using the 3D geometry described in Section 3.3.2. The naming convention for the studies is as follows: those using the gelation model developed in Section 3.5.4 are denoted with the suffix **Gel**, whilst studies using alternative viscosities are prefixed with **3D**. BC1, BC2, and BC3 mentioned in the following refer to the traction boundary conditions developed in Section 3.8. The density for all the studies is set at $\mathbf{1200\ kg/m^3}$.

For any numerical integration performed, the Numpy library is used in Python with the trapezoidal rule. Although the trapezoidal rule is not the most efficient method of numerical integration, it is preferred because of the nature of the solutions generated. The BCs used generate flow rate solutions that have sharp variations as well as unevenly spaced data due to the use of a variable time-stepping regime. This is unsuitable for more accurate numerical methods, such as Simpson's rule. Improving the trapezoidal method results can be achieved by increasing the number of time steps per cardiac cycle simulated.

Name	Model type	Viscosity ($Pa \cdot s$)	Boundary condition
3D-grid-ind *Section 3.9.1*	steady-state	1	Outer surface: $f_n = 10\ Pa$
3D-domn-vald *Section 3.9.2*	steady-state	$\eta(\dot{\gamma}) = \dot{\gamma}^{0.883-1}$	$Z_{negative}$ inflow: $\dot{m} = 3.42 \times 10^{-7}\ kg^3/s$
3D-param-visc *Section 3.9.3.1*	steady-state	0.1-1.2	Outer surface: f_n =0.7 Pa
3D-param-trac *Section 3.9.3.2*	steady-state	0.1-1.2	Outer surface: f_n =0 - 0.7 Pa
3D-card-cycl *Appendix H.1*	steady-state	1	Traction boundary: f_n =0.7 Pa
3D-solv-convg *Appendix H.7*	transient	0.579, 0.746	Traction boundary: f_n =BC1

Table 9: Summary of all 3D computational studies done using different viscosities

Name	Boundary condition	Description
Gel-timstp-ind (*Section 3.9.4*	Outer surface: $f_n = BC1, BC2, BC3$	This study finds optimal time-step settings for all boundary conditions to ensure solution stability upon time-step refinement.
Gel-const-visc (*Appendix H.3*)	Outer surface: $f_n = BC2$	This study aims to approximate the region during gelation where the increment in viscosity occurs gradually.
Gel-splt-domn (*Appendix H.7*)	Outer surface: $f_n = BC1$	This study shows that the simulation of large time domains can be segmented and reassembled, producing the same outcomes and allowing for parallel computations.
Gel-solv-convg (*Appendix H.7)*	Outer surface: $f_n = BC1$	This study demonstrates that the reduction in flow rate during gelation is solely attributed to reduced viscosity, without solver influence.
Gel-solve-perfm (*Appendix I*)	Outer surface: $f_n = BC1$	This study summarizes one-second simulation runtimes on different core setups for both a standard PC and the UCT HPC system, including runtimes using meshes from Table 12.
Gel-full-model (*Section 3.10.1*)	Outer surface: $f_n = BC1, BC2, BC3$	This study simulates gel outflow due to myocardial deformations from a defined region, incorporating the complexity of gelation.
Gel-simple-model (*Section 3.10.2*)	Outer surface: $f_n = BC1$	This study simulates gel outflow in a simpler geometry. This is done to analyse a specific behaviour observed in the results of the Gel-full-model simulation.

Table 10: Summary of all 3D computational studies done using the gelation model developed.

Similarly to the analyses conducted using the 2D geometry, wherever a traction BC is specified on the outer surface, all inlets and outlets are set to outflows.

3.9.1 Grid independence study (3D-grid-ind)

Generating an outflow using a traction BC in Polyflow requires specific grid independence criteria, as shown in the 2D grid analysis in Section 3.6.1. The valuable output required from the model is the volume lost during the gelation process, and this can be derived from the flow rate behaviour over time. With this in mind, the parameter of interest is the flow rate, which serves as a benchmark to achieve grid independence.

Following the grid independence analysis in Section 3.6.1, the regions near the output are refined more than the general domain. This approach reduces the computational expense associated with running a simulation using an overall finer mesh. The solver run times for different mesh refinements are highlighted in Appendix I. To improve grid independence and reduce computational cost, the regions closer to the outlets of the domain are refined until the flow rate converges. This mesh refinement is done in Simpleware.

The 2D grid independence study examines a symmetric domain where all outlets have identical dimensions. Any single outlet can be selected and used as a benchmark to achieve grid independence. In the case of the 3D domain, the outlets differ, and each outlet has its own standard for grid independence. The outlet with the largest variation in its velocity field is chosen and used as the benchmark to ensure that the mesh is acceptably refined. Once the mesh is sufficiently refined using this outlet, it can be assumed that all other outlets are adequately refined. For an arbitrary traction applied to the domain, it can be seen that both $Z_{positive}$ and $Z_{negative}$ faces both have the largest variation in velocity. The velocity contours for an arbitrary traction are shown in Figure 47. The $Z_{positive}$ face is selected for the analysis.

An extremely coarse overall mesh and an extremely refined outlet may be used when following this refinement methodology. This is incorrect, as the mesh would not be grid-independent for traction applied on the traction boundary. This two-step mesh refinement process applies the following logic. Since applying a traction to the boundary results in an outflow, it is desirable to attain grid independence for applied traction. The first step of this process reduces the overall element size to an acceptable value so that the mesh is grid-independent for applied traction. The second step of this process refines the outlets so that the flow field converges at the outlets. Simpleware is used to mesh the geometry, with refinement achieved by varying a coarseness parameter. Table 11 below shows the relevant mesh information for successively refined meshes.

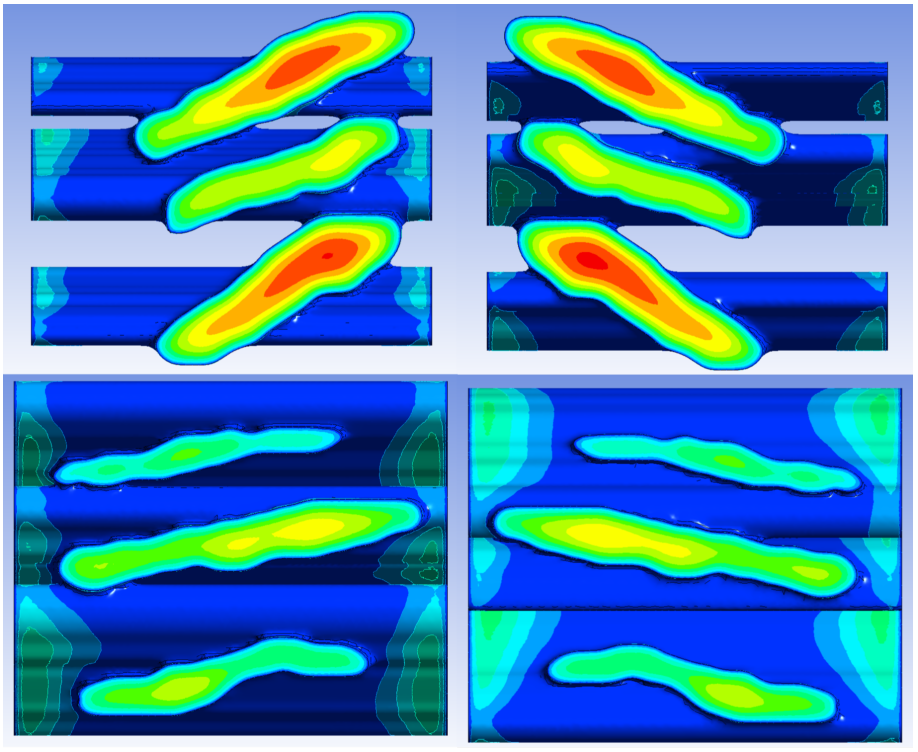

Figure 47: Velocity contours for all outlets of the fluid domain. The top row shows contours for $Z_{positive}$ and $Z_{negative}$ respectively. The bottom row shows contours for $X_{positive}$ and $X_{negative}$ respectively.

Mesh count	**Element size** (μm)	**Outer surface elements**	**$Z_{positive}$ outlet elements**
224,000	5.48	54,800	2250
337,000	4.66	77,300	3500
510,000	4.03	99,700	5360
852,000	3.43	164,447	7276
2,200,000	2.59	334,388	13,732

Table 11: Preliminary mesh refinement information.

Figure 48 shows a mesh that is refined without any refinement at the outlets. These meshes are used in conjunction with the simulation parameters described in Table 9 to analyse the flow rate out of the $Z_{positive}$ outlet. Furthermore, the velocity field at the outlet is compared for all meshes using a point cloud definition set up in CFD-Post. Figure 49 shows the point cloud visualised at the relevant outlet.

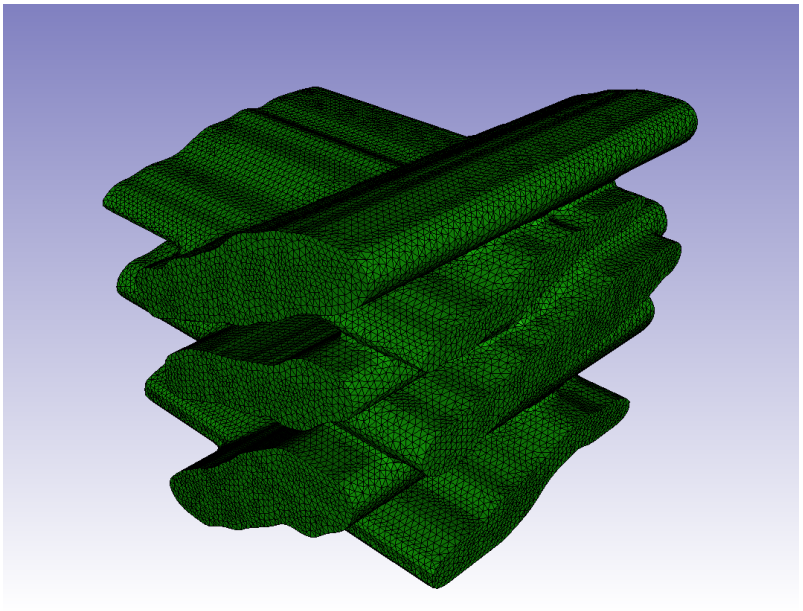

Figure 48: Mesh of the fluid domain without any mesh refinement.

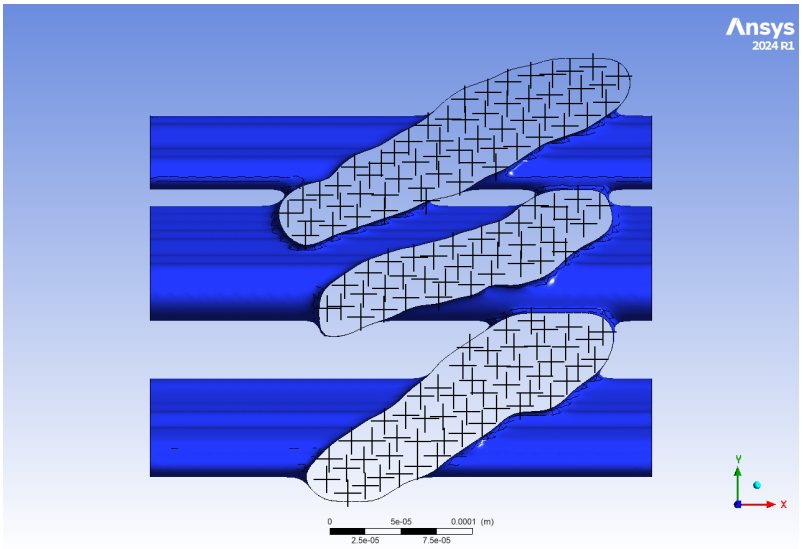

Figure 49: Point cloud created over the relevant face used for the grid independence analysis.

Further refinements to the mesh are made based on sufficient resolution of the velocity field. The regions shown for refinement are shown in Figure 50.

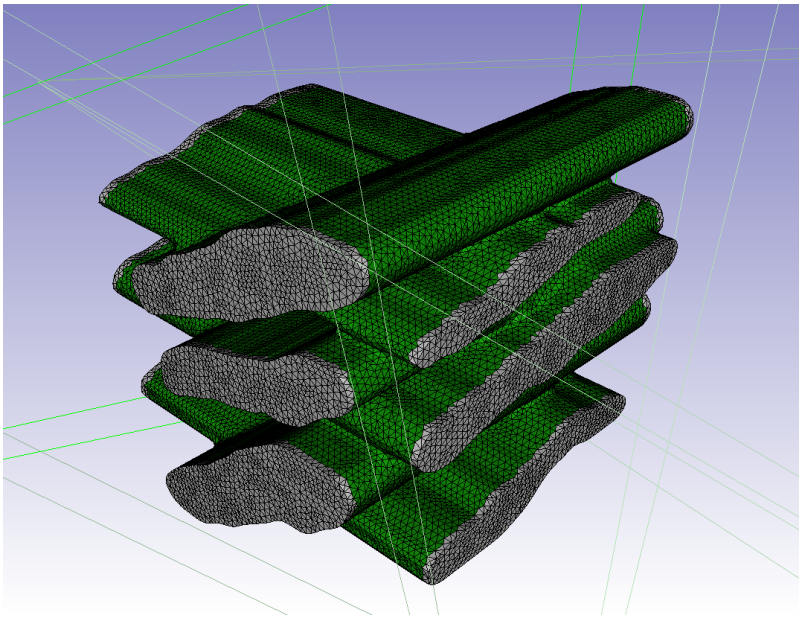

Figure 50: Mesh of the fluid domain highlighting the regions chosen for mesh refinement.

Table 12 below shows the mesh information for varying refinements made using the original 510 $\times 10^3$ mesh. Compared to the meshes in Table 11, many more elements are present on the $Z_{positive}$ face per total number of elements. This indicates an increased concentration of elements on the face, which is desirable. Figure 51 shows an example of a mesh with refined outlets compared to the regular mesh in Figure 48. These meshes are used again in conjunction with the simulation parameters in Table 9 to generate refined results. All the results of the grid independence study are presented in Section 4.2.1.

Mesh count	**Refined element size (μm)**	**Boundary elements**	**$Z_{positive}$ outlet elements**
626,000	5.76	125,000	5680
819,000	4.60	166,000	8900
977,000	4.00	185,000	13,100
1,200,000	3.5	208,000	16,000
2,000,000	2.3	313,000	33,900

Table 12: Subsequent mesh refinement

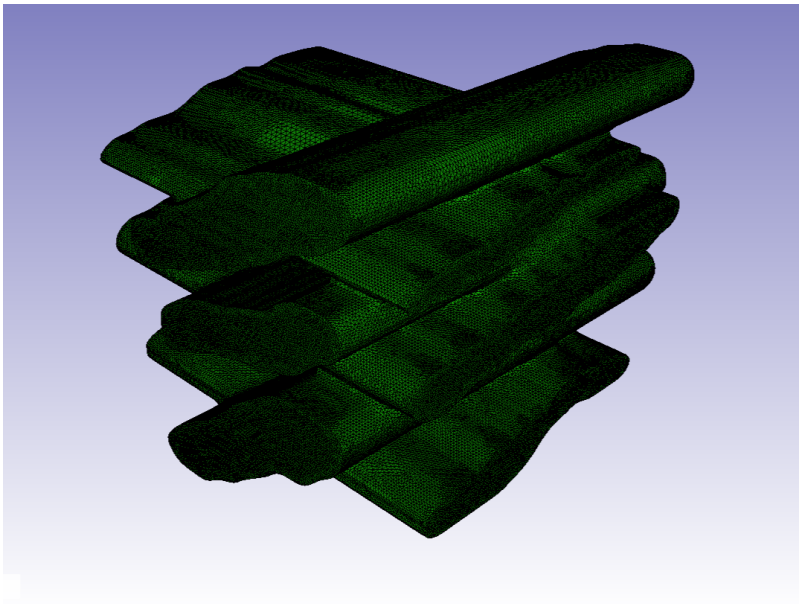

Figure 51: Mesh of the fluid region with mesh refinement.

3.9.2 Validation of microfluidic domain (3D-domn-vald)

It is imperative to validate the domain size before using it for simulation. From a study by Ngoepe et al. [12], an in silico study was performed that simulated a shear-thinning fluid flowing through a realistic tissue model. Their 3D in silico study was validated by a 2D in vitro microPIV study and a 2D in silico study. The simulation parameters are taken from this study and used to generate velocity results for comparison. Using the current fluid domain, $Z_{negative}$ is chosen as the inlet, while the rest of the faces are designated as outlets. The results are presented in Section 4.2.2.

3.9.3 Parametric studies

The BCs developed for use with this geometry experience tractions between 0 and 0.7 Pa. This is the order of magnitude used for the parametric studies to confirm the relationships established in the 2D parametric studies. The simulation parameters for the following studies are described in Table 9. The results for the following parametric studies are presented in Section 4.2.3

3.9.3.1 Parametric study on the effect of varying viscosity in 3D (3D-param-visc)

Following the 2D study in Section 3.6.3, the applied traction remains constant while viscosity varies within the limits of the gelation model. In the 2D study, the average velocity was chosen as the output parameter of interest. In this case, the volumetric flow rate is used.

3.9.3.2 Parametric study on the effect of varying traction in 3D (3D-param-trac)

In the study, for a given viscosity, three constant tractions are investigated within a specified range of traction (0.1, 0.4, 0.7). The gradient of the linear relationship is expected to change across viscosities, and this relationship is also explored.

3.9.4 Time step independence (Gel-timstp-ind)

Before using the traction BCs developed in Section 3.8 for the final analysis, it is essential to ensure that the simulations run are time-step independent. For all transient simulations run in Polylfow, the standard settings are used for time stepping. The initial time-step value is either set equal to or close enough to the minimum time-step value. As discussed earlier in the 2D analysis, this is done because of the initialisation stage due to the use of a gelling material model. Following this logic, the initial time step values are set close to the minimum time step value. The maximum time-step value is set relatively high. This allows the size of the time steps to increase if the solver convergence is good, thereby reducing the overall computational expense. Table 13 shows the settings used for the initial, minimum, and maximum time steps for all BCs.

It is worth highlighting that the start and end times for the study are chosen during a stage in the gelation process where the viscosity change occurs quickly.This is selected from 410-412 s. The logic behind this selection is that the solver is expected to use more time steps to converge onto a solution where the viscosity changes rapidly. If the solver remains time-step independent in this region for viscosity change, it will be time-step independent everywhere else. This can be seen in Figure 52, where the viscosity change occurs faster during the end stages.

The base time-step settings for all BCs are chosen based on the solver successfully running a simulation. This can be seen in Table 13 where the 1st run for each BC denotes the base time-step setting. It was found that setting a minimum time step value higher than the base setting resulted in the solver failing to reach a converged solution. Once the initial time-step settings are obtained, they are successively refined, as shown in Table 13. The results can then be compared to see if a converged solution is achieved and these are presented in Section 4.2.4.

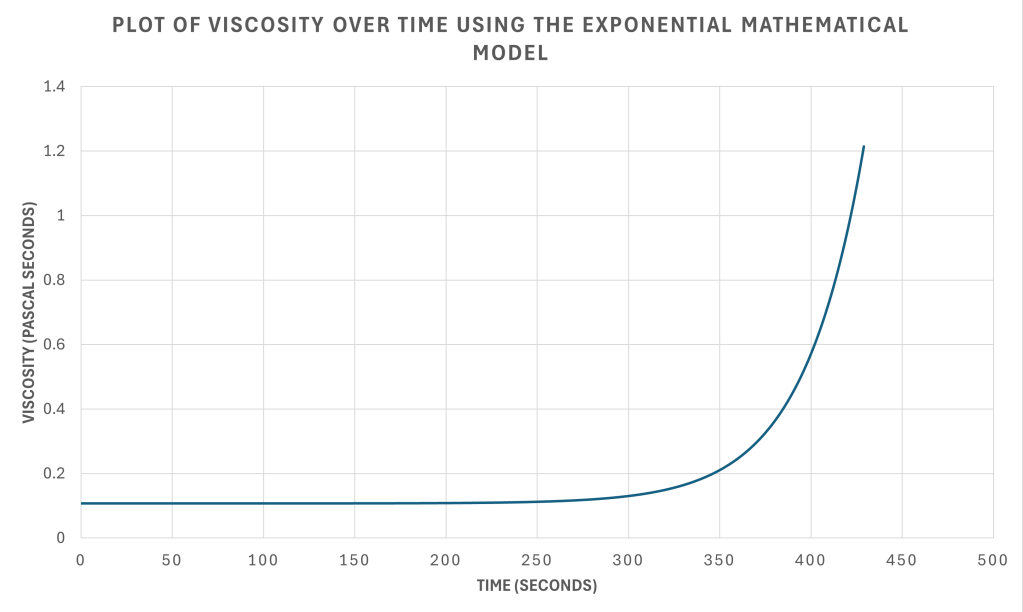

Figure 52: Plot of viscosity over time for the gelling material model used.

Boundary Condition	Initial value	Minimum value	Maximum value
BC1 1st run	0.001	0.001	0.01
BC1 2nd run	0.0005	0.0005	0.005
BC1 3rd run	0.00025	0.00025	0.0025
BC2 1st run	0.001	0.001	0.01
BC2 2nd run	0.0005	0.0005	0.005
BC2 3rd run	0.00025	0.00025	0.0025
BC3 1st run	0.001	0.0001	0.01
BC3 2nd run	0.0005	0.00005	0.005
BC3 3rd run	0.00025	0.000025	0.0025

Table 13: Timestep settings for all simulations

Various other studies are conducted to validate the modelling approach before conducting the case studies that follow. These include a justification for the rigid CFD assumption made, a methodology for shortening the time domain to be simulated, a methodology for obtaining results faster using multiple compute cores, and a study that tests the convergence of the solver as it generates a solution with a gelling material model. The respective methodology and results can be found in Appendix H.

3.10 Case Studies

3.10.1 Flow behaviour of PEG during gelation (Gel-full-model)

Using the analysis conducted in the previous subsection, a methodology can now be outlined to achieve the research objective stated in Section 1.2.2. Each BC can be used with a gelling material model to investigate PEG losses as it undergoes a phase change within the myocardium. Additionally, using different BCs allows one to note any differences between the solutions. In accordance with the analysis in Section H.3, the total time domain to be simulated can be divided into three intervals: 0-190 s, 190-220 s, and 220-417 s.

To simulate the initial two time domains, the following strategy is implemented. At the beginning of each section, a few cycles are simulated. As anticipated, the gradual change in viscosity leads to a uniform volume lost per cycle. This value is averaged to produce a representative figure for the volume lost per cycle within each section. This average can subsequently be multiplied by the total number of cycles in that region to determine the overall volume lost per section. In the final region, where viscosity change is dynamic, the solution is simulated across the complete time domain. This process is optimised using the analysis in Section H.5, where the time domain to be simulated is segmented according to the number of solvers used. Using a 40-core setup on the UCT HPC system, ten solvers are configured, allocating four cores to each solver. Solutions are then generated for all boundary conditions over the entire duration of gelation. The results are detailed in Section 4.3.1.

3.10.2 Flow behaviour of PEG in a simpler geometry (Gel-simple-model)

The results of the preceding case study reveal certain behaviours concerning the kinetics of volume loss per cycle that warrant further investigation. A subject of inquiry is whether these behaviours are specific to the simulation domain or represent an intrinsic characteristic of gelling materials under pulsatile flow conditions. To address this, a model is set up that uses a simple 3D cylindrical geometry with the same BC. Further details on the geometry can be found in Appendix K.

This case study focusses on behaviour rather than loss; therefore, only the region experiencing a change in dynamic viscosity is simulated. The prior case study indicates that assuming constant viscosity in later regions past 200 seconds is slightly inaccurate, revealing an abrupt step change. Therefore, in this study, the time frame during which dynamic viscosity begins to change is increased and begins sooner. The simulated time domain begins at 200 s, in contrast to 220 s in the previous study. The results are presented in Section 4.3.2.

4 Results and Discussion

This chapter presents all the results related to the analysis done using the 2D and 3D geometry. The first section presents 2D geometry results in the following manner: grid independence study, various traction BC configurations, parametric studies for viscosity and traction, and validation for using the solver with time-dependent viscosity. The next section presents 3D geometry results, including: grid independence study, domain size validation, parametric study of the same two key parameters, time-step independence, rigid CFD model justification, solver setup optimisations for efficient solutions, and solver convergence with time-dependent viscosity. The final section discusses results from two case studies. The first case study examines the gelation of PEG while present in the myocardium. The second case study explores whether a specific behaviour observed in the first study is influenced by the domain shape using a simple 3D geometry.

4.1 Results of the analysis of the 2D microfluidic geometry

4.1.1 Grid independence study results

The results presented in this section are related to the analysis conducted in Section 3.6.1. Figure 53 illustrates a velocity contour that shows the flow field generated by applying normal traction. The results in this section relate to two separate grid independence studies. Figures 54 and 55 show results for the unrefined meshes detailed in Table 6. Figures 56 and 57 show results for meshes with a refined outlet as detailed in Table 7.

Figure 54 below visualises the differences in velocity solutions at the outlet for successively refined meshes. The results indicate that the solutions exhibit poor convergence as the distance from the axis of symmetry to the traction boundary increases. Figure 55 illustrates the relative differences in the velocity solutions. A significant relative difference is observed near the traction boundary.

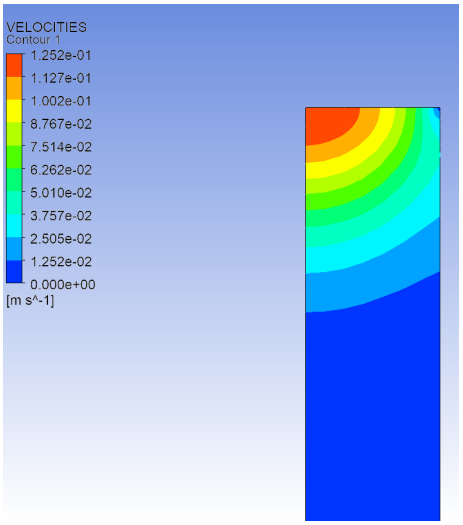

Figure 53: Velocity contour of the simulation where normal traction is applied to a fluid domain. In this instance, the shear velocity at the boundary is set to 0. The velocity observed at the wall (right) is perpendicular to the surface.

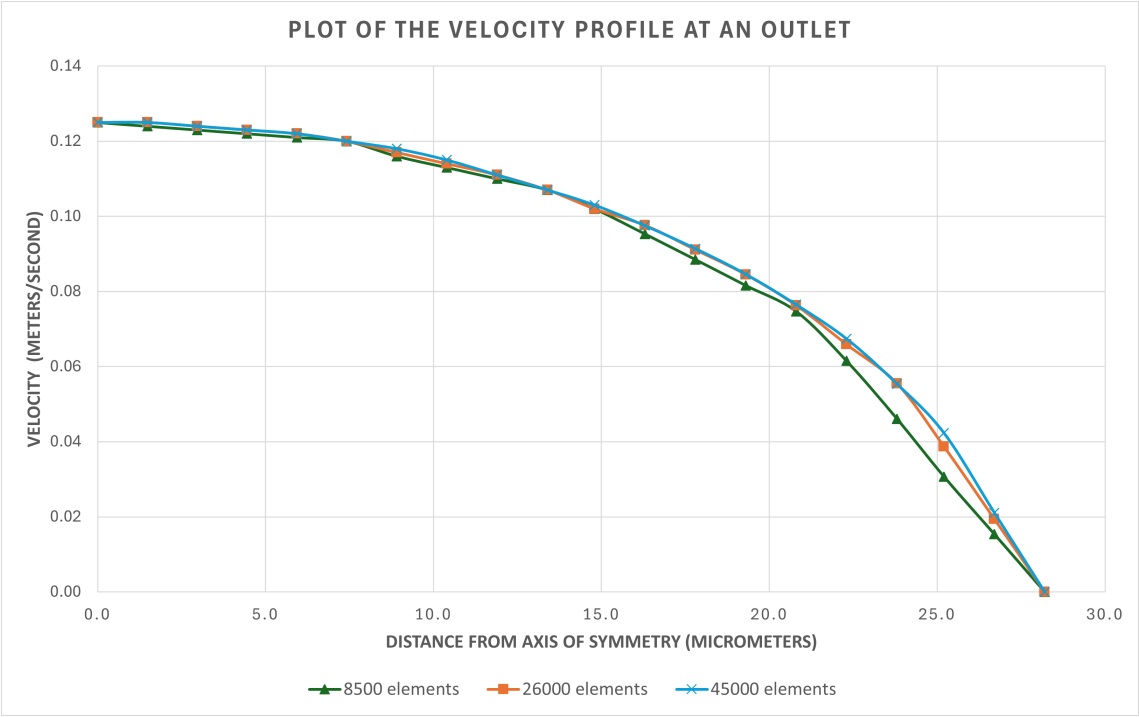

Figure 54: Velocity profiles for different meshes without special refinement.

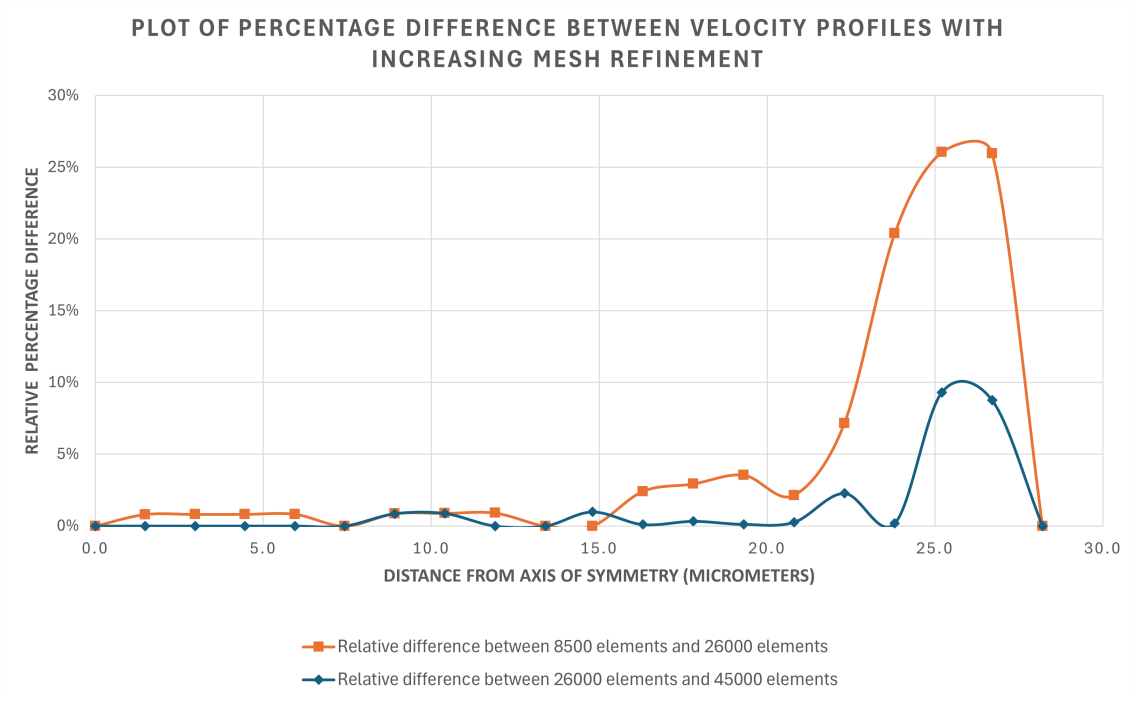

Figure 55: Percentage differences between different meshes as you move further away from the axis of symmetry. It is important to highlight the large difference observed closer to the edge.

Figure 56 illustrates the velocity solutions that converge with the refined outlets in comparison to a highly refined mesh from the initial grid independence analysis. Figure 57 illustrates a significant decrease in the relative difference in velocity solutions as the outlets are refined.

Upon examining the results presented in Figure 56 and Figure 57, it is evident that the outlet velocities converge when using a finely refined outlet. A notable reduction in the relative difference is observed closer to the outlet, achieved with only a minimal increase in the mesh count. This approach for grid independence is similarly applied in the 3D grid independence study.

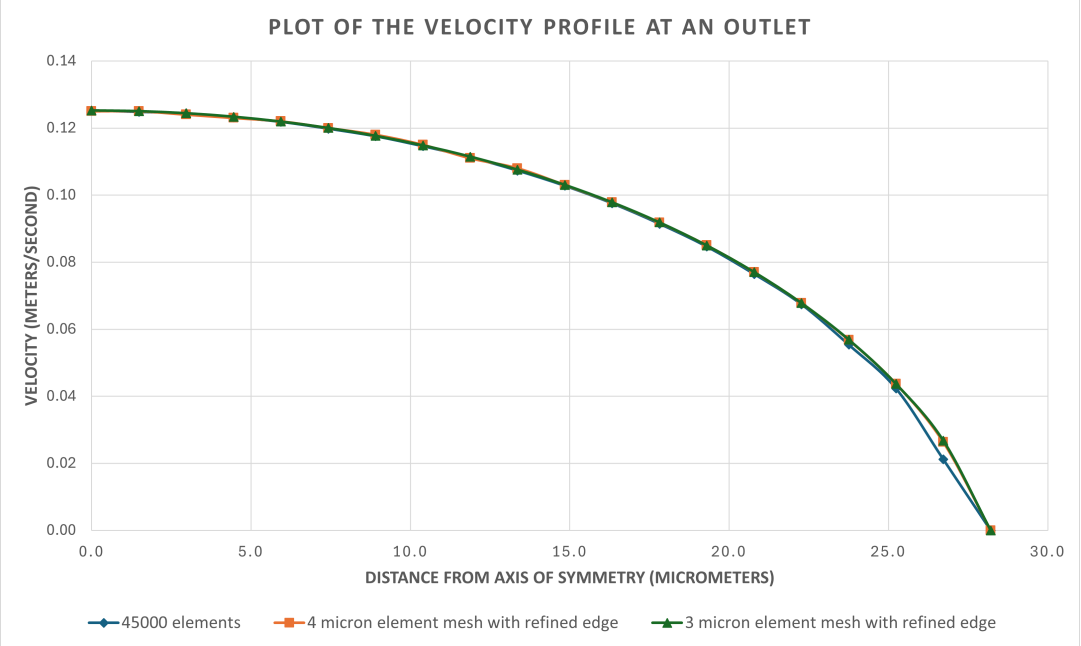

Figure 56: Velocity profiles for different meshes with the outlets refined.

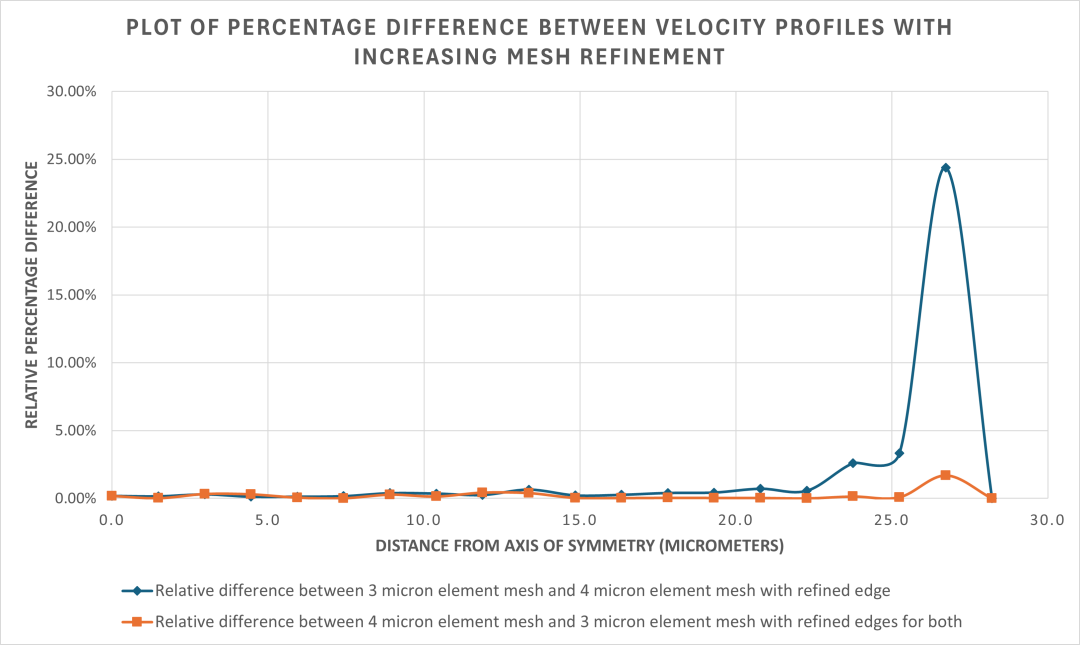

Figure 57: Percentage differences between different meshes as you move further away from the axis of symmetry.

4.1.2 Traction BC preliminary analysis results

The results in this section are related to the analysis performed in Section 3.6.2.

4.1.2.1 Different traction boundaries

Figure 58 illustrates the variation in results for the same normal traction applied with varying Neumann boundaries. The results indicate that using the traction BC with a specified shear velocity is preferable. Setting the shear traction to zero results in an uneven velocity distribution, despite the normal traction being uniformly applied. This can be shown in the bottom image of Figure 58. Moreover, it is ideal to impose a no-slip condition at the walls of the fluid domain. The computational models discussed in Sections 2.5.2 and 2.5.3 impose no-slip conditions. In the study by Ngoepe et al. [12], no-slip was also specified when modelling their realistic geometry. Setting the shear velocity to 0 m/s enforces this condition. In cases where the shear velocity is specified, a non-zero velocity is observed at the wall, as shown in the top image of Figure 58. However, this velocity is normal to the wall.

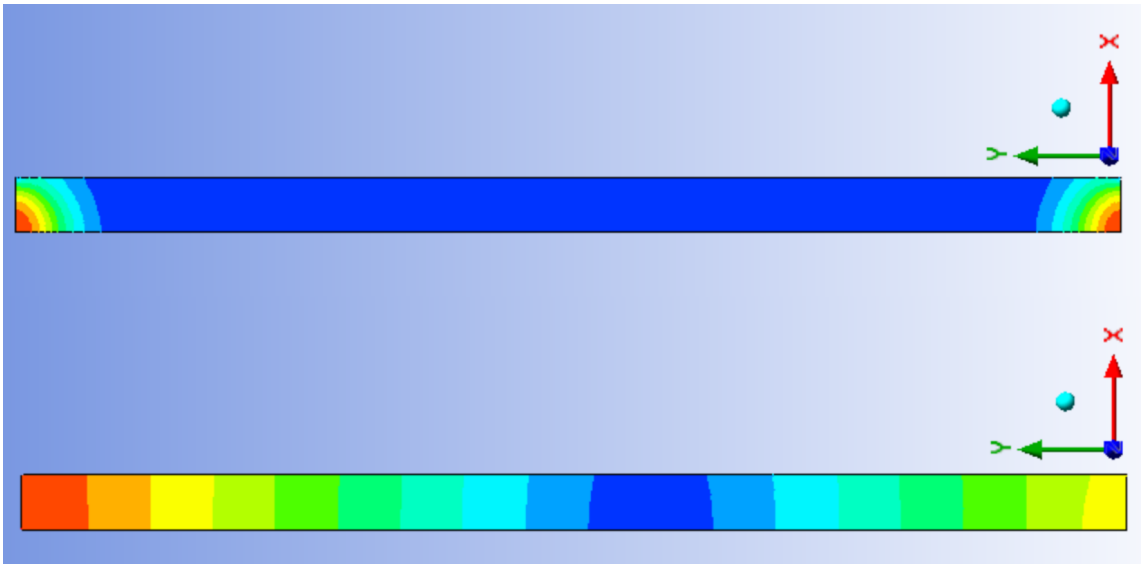

Figure 58: Velocity contour plots due to using different traction BCs. The top contour is for the case where the shear velocity is set to 0 m/s. The bottom contour is for the case where the shear traction is set to 0 Pa.

4.1.2.2 Constant traction

As anticipated, when constant traction is applied, the average velocity decreases as viscosity increases over time. Figure 59 below shows the gradual drop in average

velocity as the viscosity increases.

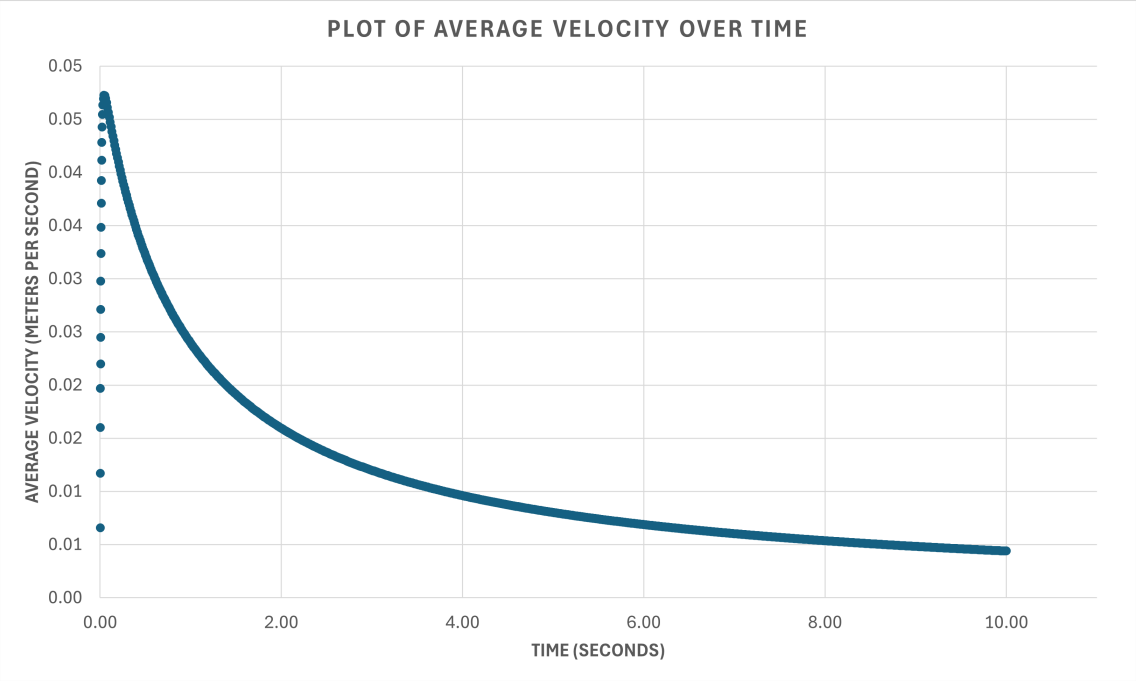

Figure 59: Plot of average velocity over time as a constant traction is applied on the boundary with a gelling material.

4.1.2.3 Periodic traction

The findings align with the anticipated outcomes. As viscosity increases, for the same fluctuating effort exerted to move the fluid, the flow rate peaks will drop. Figure 60 shows the drop in the velocity maxima as the viscosity increases. For the function closer to the x-axis, $f_n = \mathbf{0.15cos}(\pi \cdot \mathbf{t}) + \mathbf{0.2}\ Pa$, the solver required **200** timesteps to reach the solution. Conversely, the function further from the x-axis required **128** timesteps. From these results, it is evident that the total number of timesteps varies for each periodic function used. For the function closer to the x-axis, the result required more timesteps. Therefore, it can be deduced that if a function nears a value of 0, the required timesteps will increase significantly, potentially becoming infinite.

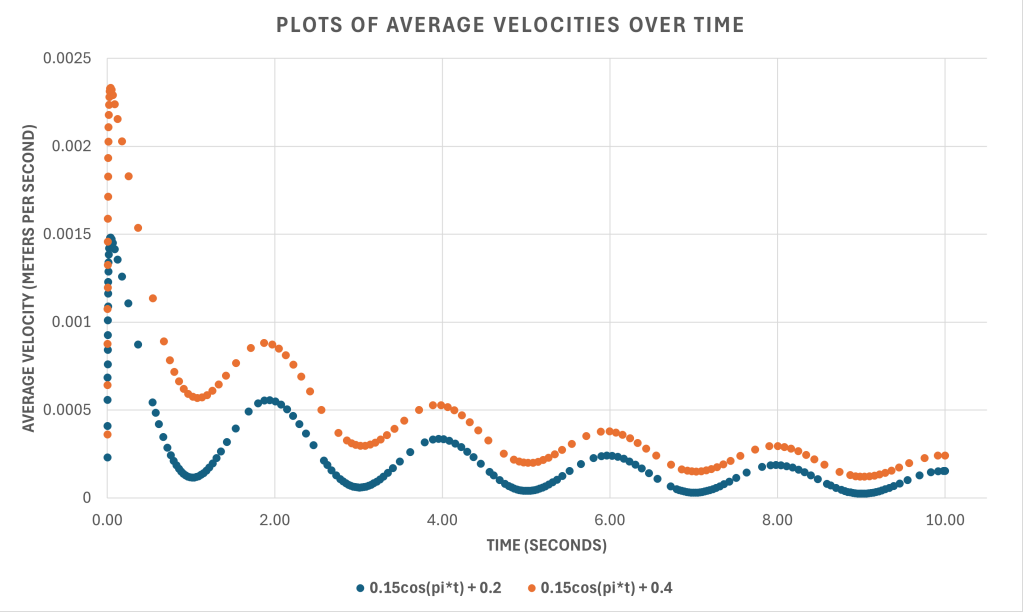

Figure 60: Plots of average velocity over time for different periodic tractions applied with a gelling material.

4.1.3 Varying viscosity parametric study results

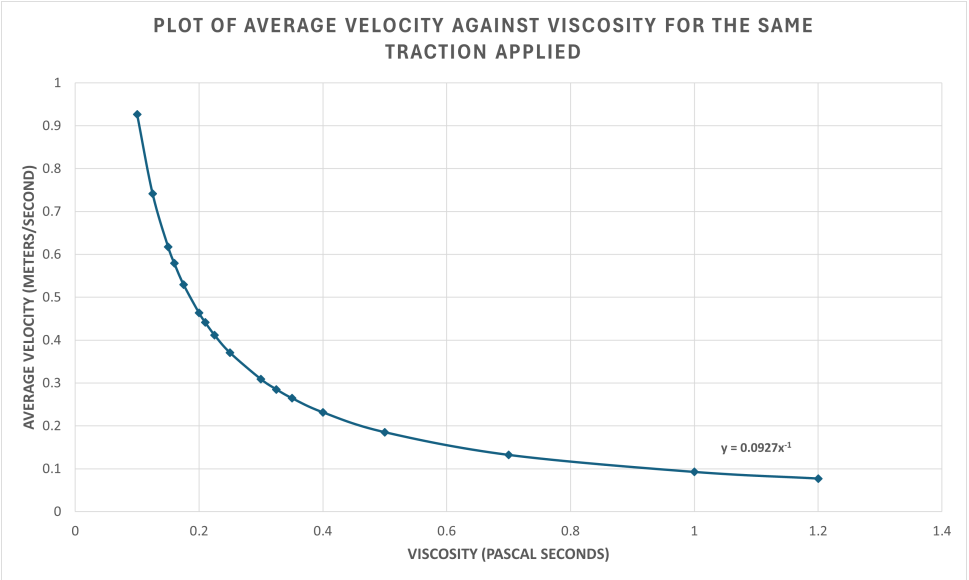

Figure 61: Plot of average velocity against viscosity for the same traction applied which shows an inverse relationship.

The results in this section are related to the analysis conducted in Section 3.6.3. Figure 61 indicates an inverse relationship between fluid viscosity and the observed average velocity for the same traction applied.

4.1.4 Varying traction parametric study results

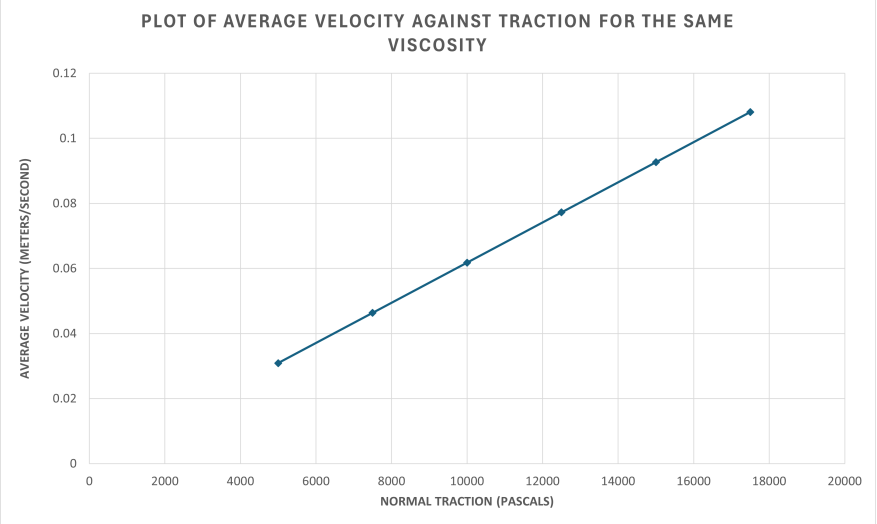

Figure 62: Plot of average velocity against normal traction.

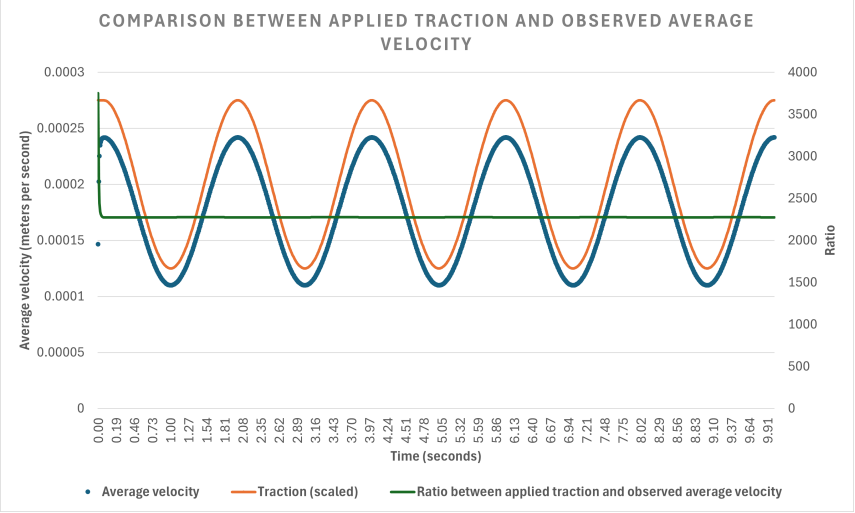

Figure 63: Plot of average velocity against time with the traction function scaled for visualisation purposes. The ratio between the two parameters is also plotted to show a perfectly linear relationship.

The results in this section are related to the analysis conducted in Section 3.6.4. Figure 62 shows that the applied traction is linearly related to the average velocity for static simulations. Figure 63 verifies the linear relationship for a transient simulation. It can be concluded that this relationship remains consistent in both steady-state and transient simulations.

4.1.5 Proof of concept simulation results

The results presented in this section are related to the analysis performed in Section 3.6.5. Appendix B provides the derivation of the relationship between inlet pressure and viscosity as $inlet\ pressure = 2\times10^6\times0.035\times\mu$. The Polyflow solution illustrated in Figure 64 is closely aligned with the analytical solution, except during the initial few milliseconds. This can be attributed to the initialisation of the time-dependent viscosity function when the simulation is run. The Fluent solution does not converge immediately and takes some time to converge onto the analytical solution. Figure 65 displays the relative difference between each numerical solution and the analytical solution.

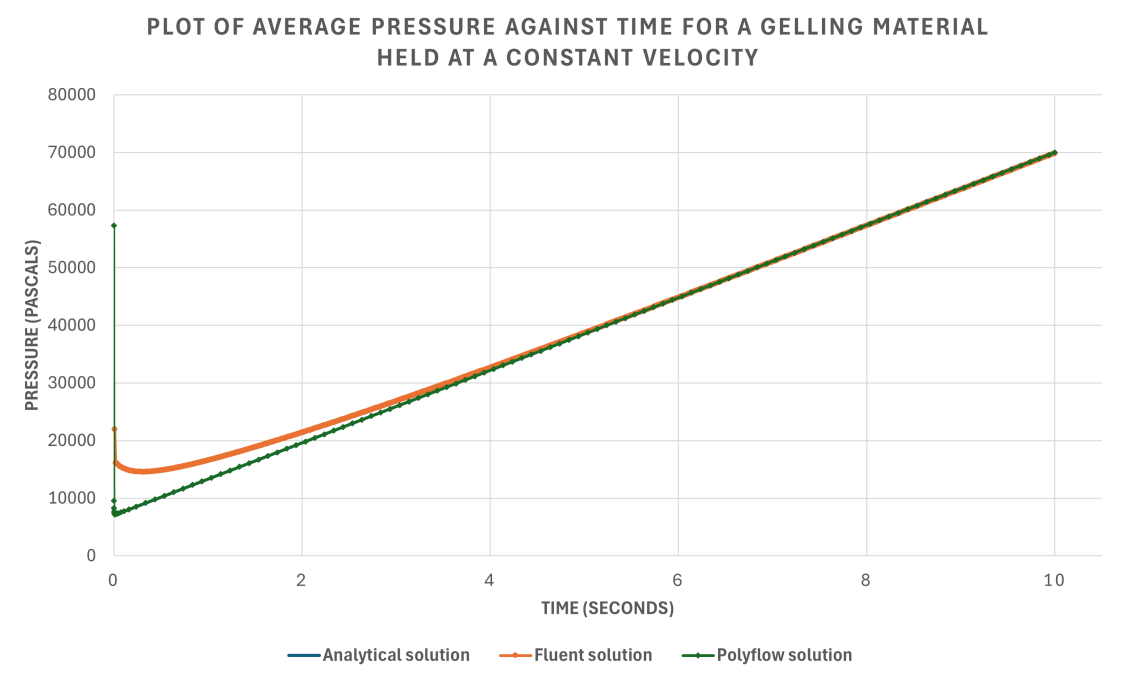

Figure 64: Plot of average pressure against time for a gelling material for analytical and numerical solutions.

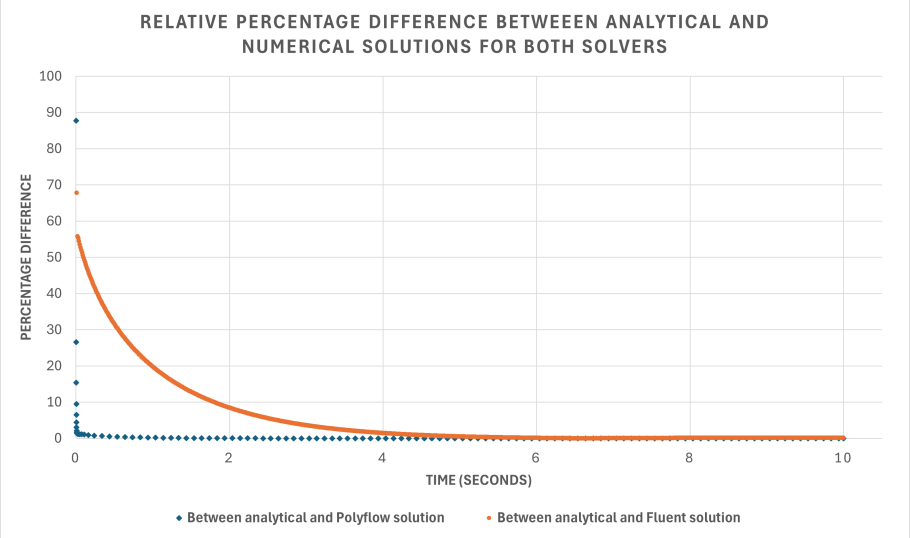

Figure 65: Relative differences between the analytical solution and each numerical solution.

The observation made between pressure and viscosity is in line with the conclusions drawn by Yang et al. discussed in Section 2.5.2. They noted that the pressure in the flow channel increases with increasing material viscosity. In this computational study, it is observed that the pressure at the inlet increases as the viscosity increases.

4.2 Results of the analysis of the 3D microfluidic geometry

4.2.1 Grid independence study

The results presented in this section are related to the analysis conducted in Section 3.9.1. Table 14 and Figure 66 are results that support the discussion regarding the use of meshes without special refinement. Table 15 and Figure 67 support the discussion of using meshes with refined outlets.

The preliminary grid independence study results, using the meshes in Table 14, indicate that the 510 $\times 10^3$ element mesh converges within 2% of the 2,200 $\times 10^3$ element mesh results. This shows that the mesh is sufficiently refined for the traction applied to the boundary. The velocity field is also extrapolated on the point cloud definition described earlier. Figure 66 shows the relative differences between the velocity results of the 510 $\times 10^3$ element mesh and the 2,200 $\times 10^3$ element mesh. It shows that the velocity results converge in the central region of the face; however, large relative differences remain closer to the edges. To minimise this, the 510 $\times 10^3$ element mesh is used and the outlets are refined.

Mesh count $\times 10^3$	**Volumetric flow rate** $\times 10^{-3} \frac{mm^3}{s}$	**Relative difference** %
224	5.73	15.6
337	5.93	11.7
510	6.49	2.03
852	6.54	1.27
2200	6.62	0

Table 14: Flow rate results for each mesh with their relative differences calculated with respect to the solution obtained using the 2,200 $\times 10^3$ element mesh.

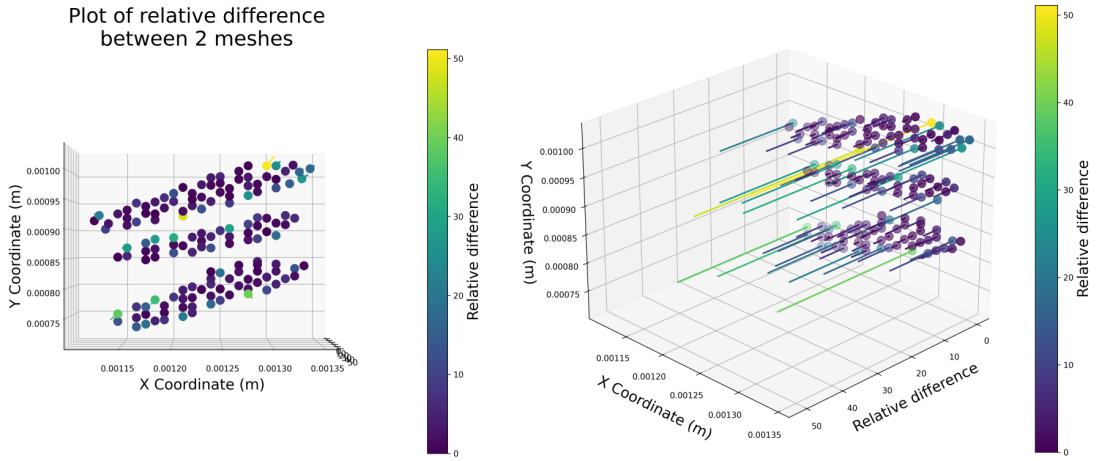

Figure 66: Relative differences between velocity results extrapolated on the point cloud. This is between two meshes that do not have outlet refinement.

Mesh count (refined) $\times 10^3$	**Volumetric flow rate** $\times 10^{-3} \frac{mm^3}{s}$	**Relative difference** %
626	6.18	9.56
819	6.12	10.61
977	6.80	0.35
1200	6.78	0.17
2000	6.77	0

Table 15: Flow rate results for each mesh with their relative differences calculated with respect to the solution obtained using the 2,000 $\times 10^3$ element mesh.

Table 14 shows the relative differences in the flow rate results generated using normally refined meshes. Figure 66 visualises the relative differences across the $Z_{positive}$ for the velocity results generated using the 510 $\times 10^3$ element mesh and the 2,200 $\times 10^3$ element mesh.

The results of the subsequent grid independence study indicate that the mesh comprising 977 $\times 10^3$ elements converges within 1% of the flow rate obtained with the 2,000 $\times 10^3$ element mesh. The results are detailed in Table 15. The velocity data is further extrapolated using the point cloud for comparison. Figure 67 illustrates the relative difference in velocity results, indicating a general decrease in relative difference compared to the preliminary mesh refinement. Therefore, the 977 $\times 10^3$ mesh can be confidently used for further analysis. Furthermore, the GCI value for the mesh is calculated using the solutions obtained. The details of this analysis can be found in Appendix G.1. The GCI_{coarse} value is obtained as 2.5% which indicates that the courser mesh in this case is reasonably refined.

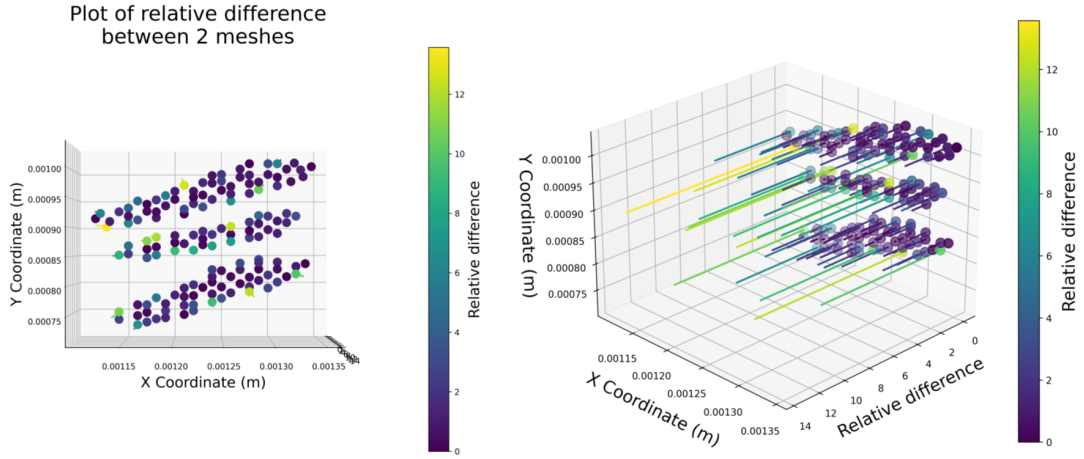

Figure 67: Relative differences between velocity results extrapolated on the point cloud. This is between two meshes that have outlet refinement.

4.2.2 Domain validation results

The results presented in this section are related to the analysis conducted in Section 3.9.2. Figure 68 illustrates the lines along which the velocity results are extrapolated. The left image shows the Z positive face, the top right image shows the X positive face, and the bottom right image shows the X negative face. Figure 69 shows the velocity profiles along the lines drawn at each outlet.

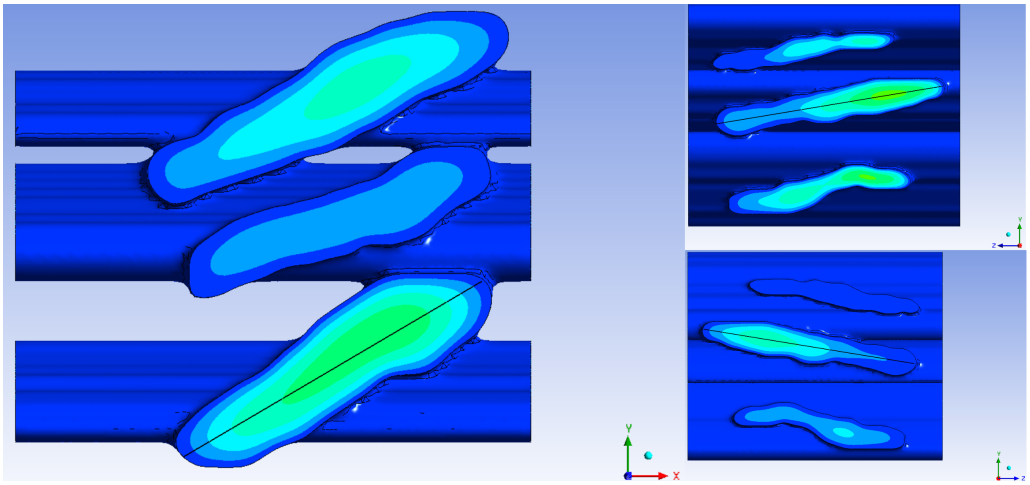

Figure 68: Velocity contours showing the lines (in black) along the faces where the velocity results are extrapolated.

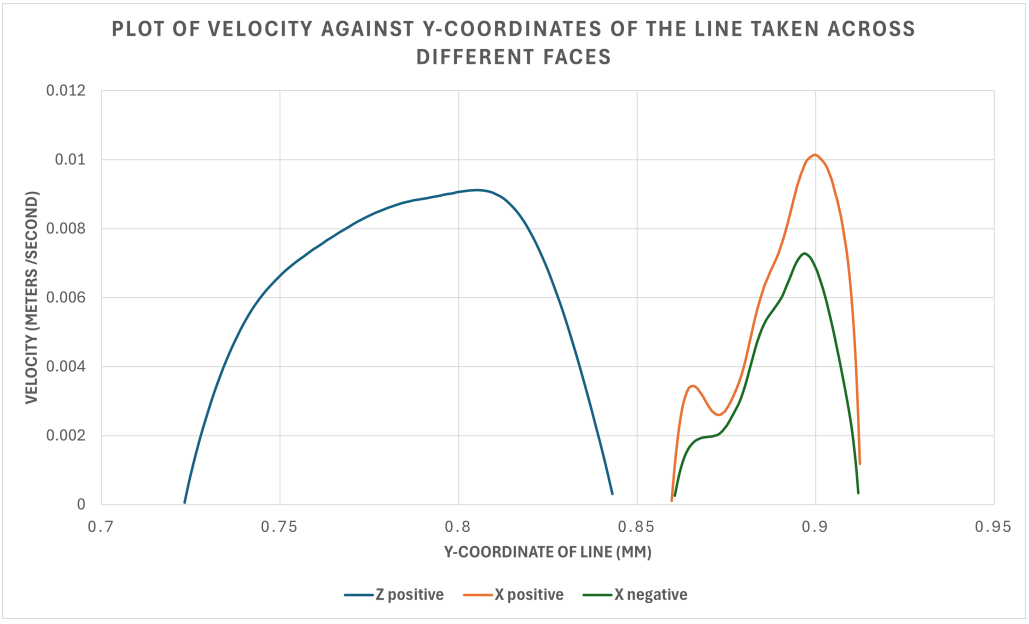

Figure 69: Plot of velocity along all lines described in Figure 68 above.

When comparing these results with those obtained in the study [12], it is noted that the results from this domain are larger by an order of magnitude of 10. This can be attributed to variations in domain sizes and overall geometry. The referenced study used a domain measuring $660 \times 560 \times 440\ \mu m$, whereas the domain used in this

project measures 351 × 311 × 381 μm. For the same flow rate, a smaller domain typically exhibits higher flow velocities compared to a larger domain, provided that the inlets and outlets remain consistent. Given these considerations, the domain may be appropriately used for microfluidic simulations.

4.2.3 Parametric study results

The results in this section are related to the analysis performed in Section 3.9.3.

4.2.3.1 Varying viscosity parametric results

Figure 70 below illustrates an inverse relationship between the viscosity of the domain and the resultant flow rate. This finding is consistent with the analysis performed using the 2D geometry. Consequently, it can be inferred that the observed behaviour is invariant across various geometries. However, the exact mathematical relationship between viscosity and flow rate specifically depends on the traction applied and the geometry.

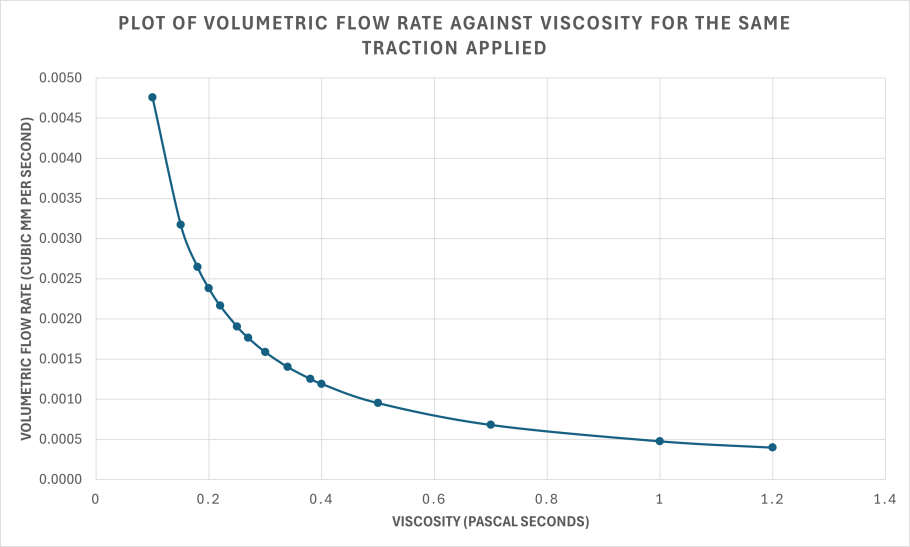

Figure 70: Plot of observed flow rate against viscosity set for a constant traction applied.

4.2.3.2 Varying traction parametric results

The study results, illustrated in Figure 71, corroborate the relationship identified in the earlier 2D analysis. The relationship between the applied traction and the observed flow rate is shown to be linear.

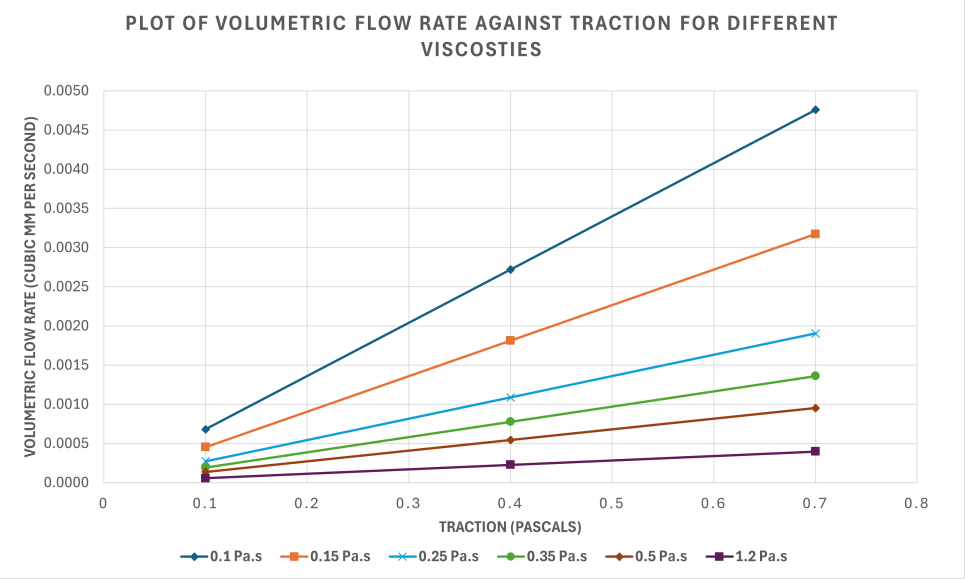

Figure 71: Plots of observed flow rate against applied traction for different viscosities.

As anticipated, the behaviour varies with differing viscosities. The gradient of the traction variation is found to be inversely related to the viscosity set, as illustrated in Figure 72.

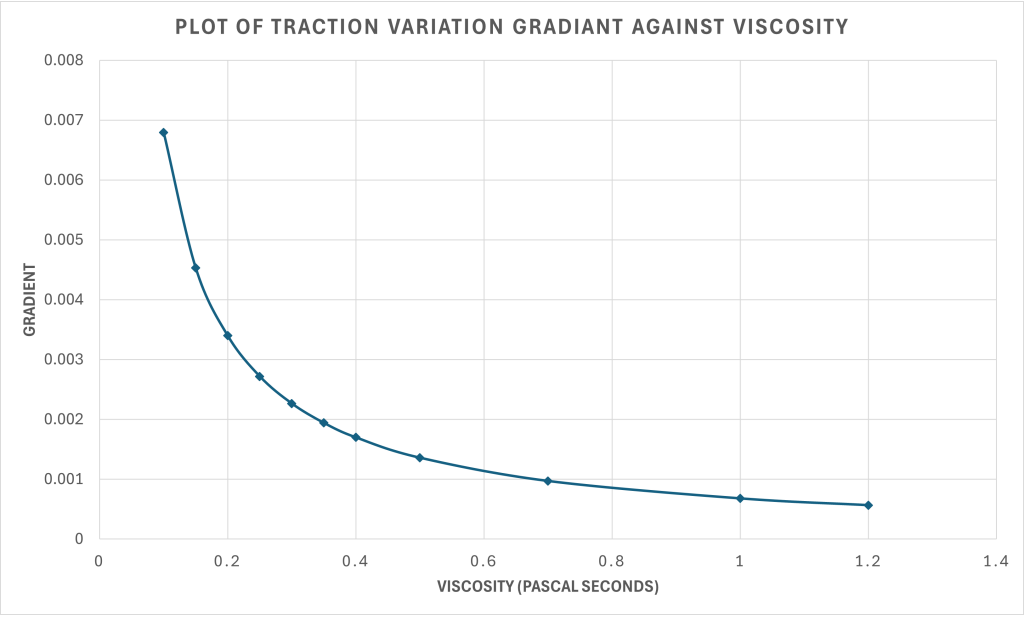

Figure 72: Plot of traction variation gradient against viscosity used.

Further discussion can be made on the impact of applied traction on shear rate variation within the fluid domain. Figure 73 illustrates the variation in the shear rate at an outlet. This variation is important when considering the non-Newtonian behaviour of PEG as it results in corresponding changes in viscosity within the fluid domain. These changes in viscosity affect the resulting distribution and may affect the overall retention of PEG. This result agrees with the findings of Ngoepe et al. in their study [12] where they showed that shear rates vary significantly within a single channel.

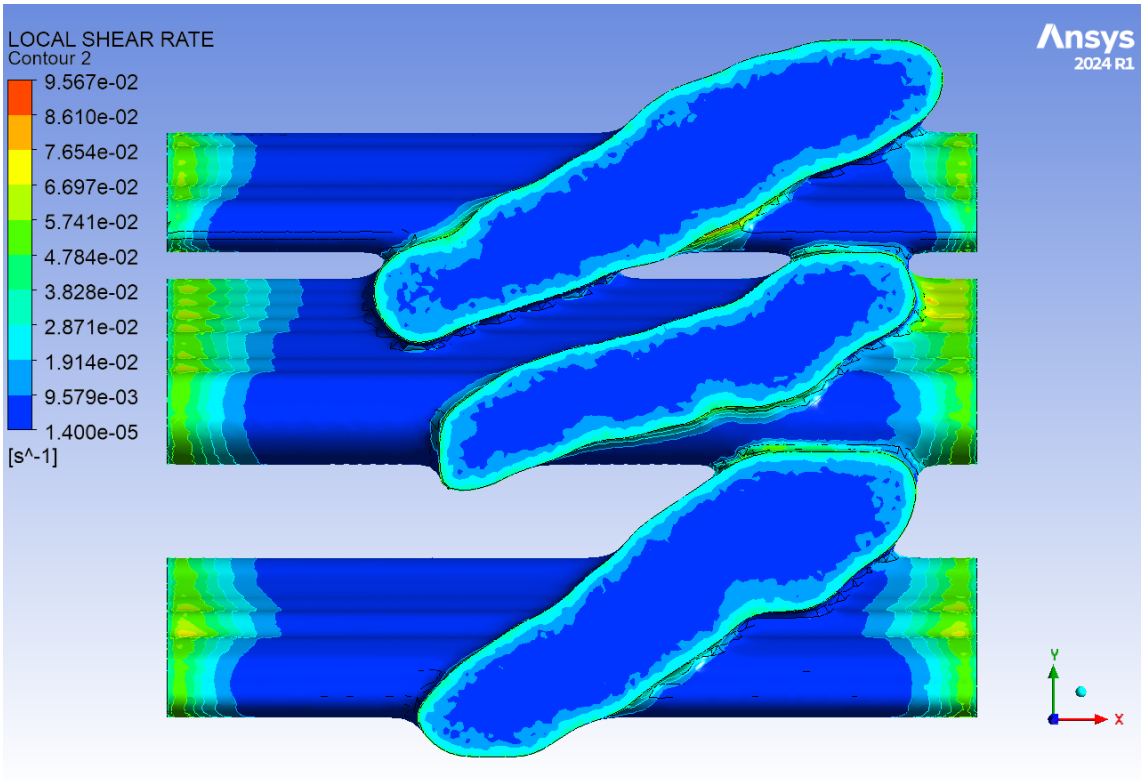

Figure 73: Shear rate contour of the fluid domain showing the variation in shear rate at an outlet.

However, there are differences in the results when comparing the magnitude of the shear rates with previous studies. The shear rate contour in Figure 73 is obtained for the maximum traction applied to the domain. The results of Ngoepe et al. and Maluleke [59] had higher shear rates (maximum of 36 $s^{-}1$ and 164 $s^{-}1$, respectively), while the maximum shear rate in this study is around 0.09 $s^{-}1$. These results show consistent shear rates across all outlets, unlike Maluleke's results, which exhibited significant variation across all outlets.

4.2.4 Timestep independence study

The results presented in this section are related to the analysis conducted in Section 3.9.4. Table 16 shows the run times for each boundary condition, along with their corresponding time-step refinements.

Boundary condition	1st run time (hours)	2nd run time (hours)	3rd run time (hours)
BC1	8.89	10.9	17.8
BC2	9.68	14.7	20.4
BC3	9.5	14.8	26.3

Table 16: Run times for each boundary condition with increasing time step refinement.

Figure 74 visually presents the BC1 solutions for each run. The area under the curve (in this instance, representing the volume lost) is computed for each run and compared to quantify the degree of convergence. The volumes for runs 1, 2, and 3 are 3.85 $\times 10^{-4} mm^3$, 3.86 $\times 10^{-4} mm^3$, and 3.86 $\times 10^{-4} mm^3$, respectively. The volume for run 1 is within 1% of that for run 3, indicating that the base time-step setting is appropriate for further analyses.

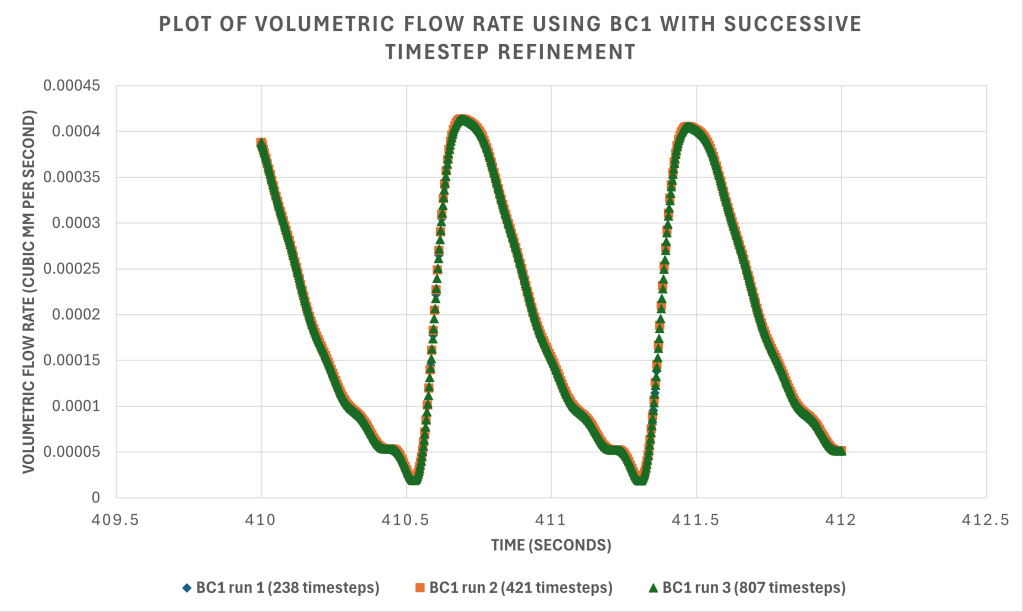

Figure 74: Plot of flow rates obtained using BC1 with increasing time step refinement. The number of time steps required for each solution is also noted.

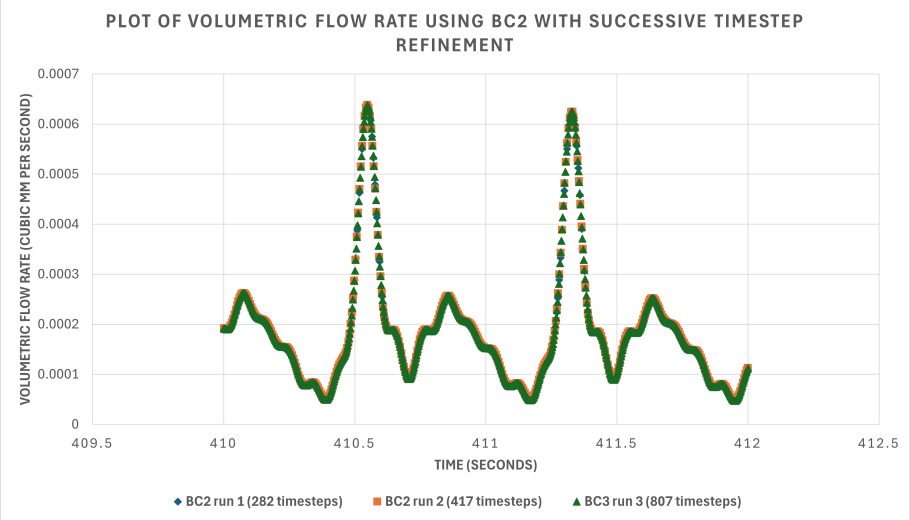

Figure 75: Plot of flow rates obtained using BC2 with increasing time step refinement. The number of time steps required for each solution is also noted.

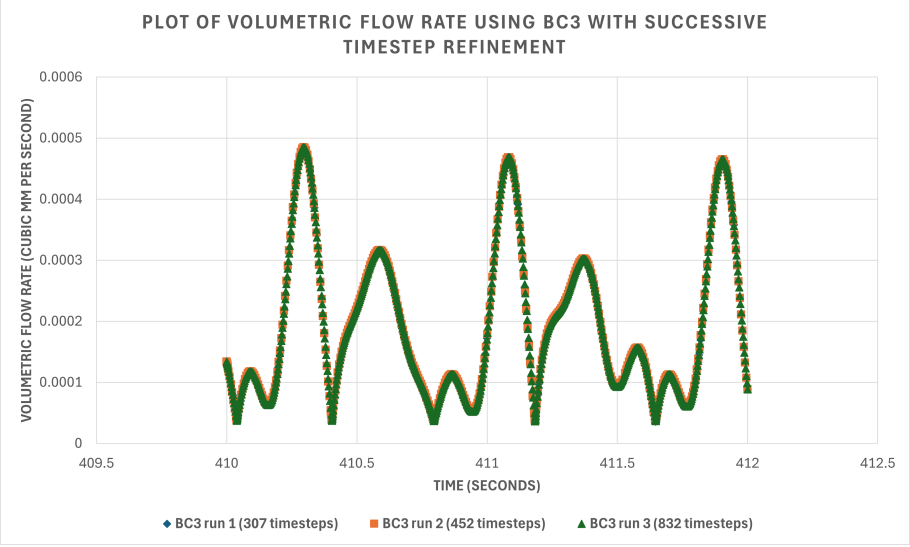

Figure 76: Plot of flow rates obtained using BC3 with increasing time step refinement. The number of time steps required for each solution is also noted.

Similarly to BC1, the runs for BC2 demonstrate satisfactory convergence despite increasing time-step refinement. The solutions are presented in Figure 75 and the same area analysis is performed. The volumes for runs 1, 2, and 3 are 3.74 $\times 10^{-4} mm^3$, 3.74 $\times 10^{-4} mm^3$, and 3.75 $\times 10^{-4} mm^3$, respectively. The base time-step setting for

this BC is also adequate for further application. Similarly to BC1 and BC2, the solutions for BC3 also exhibit good convergence. The volumes for runs 1, 2, and 3 are 3.93 $\times 10^{-4} mm^3$, presented to three significant figures. The results from the time step independence study indicate that the base time step settings are suitable for all BCs, yielding accurate solutions while significantly reducing run time. Furthermore, the GCI method is adopted to obtain a convergence index value. This is done to assess the error obtained by using a courser time-step setting. The details of this analysis can be found in Appendix G.2. The convergence index is found to be 0. 49%, indicating good convergence which justifies using the courser time-step setting.

4.3 Case Study results

4.3.1 Gelling results for all BCs

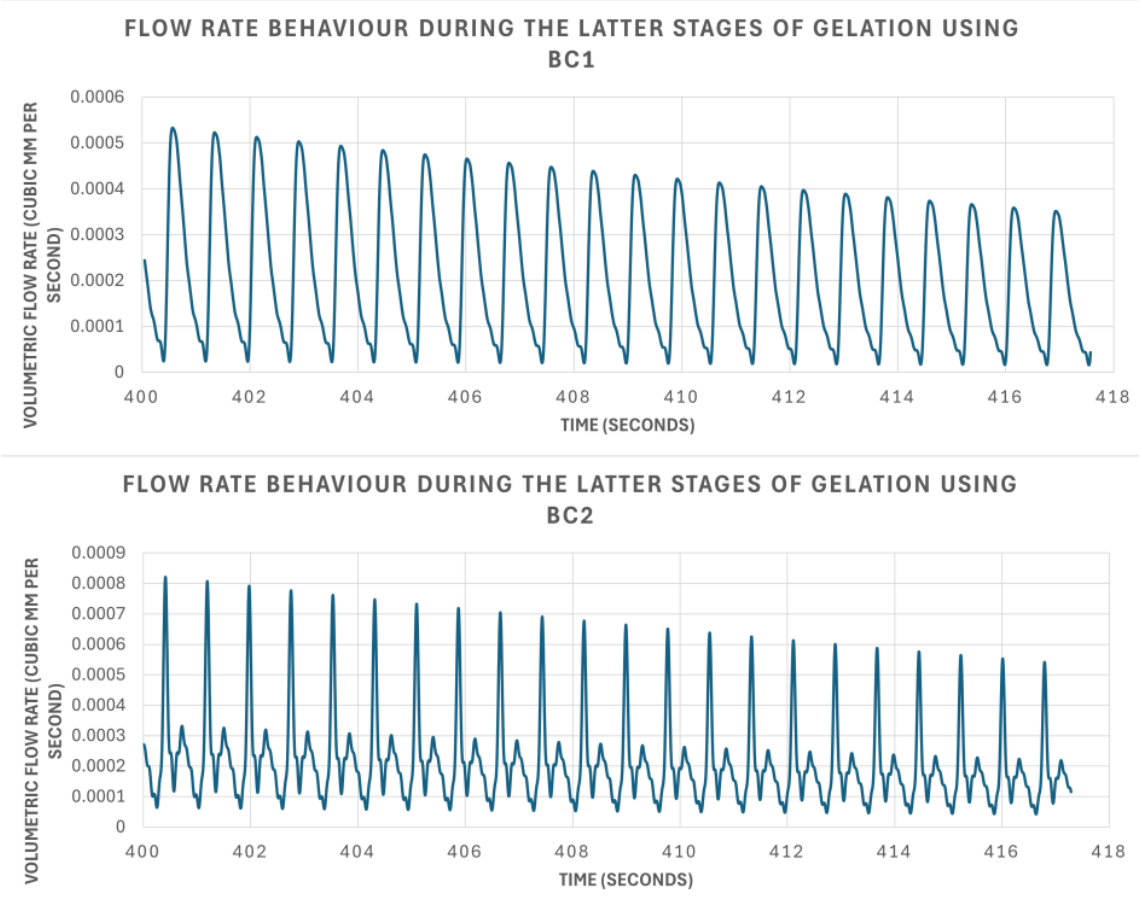

Figure 77: Plots of volumetric flow rate over time for BC1 and BC2 during the latter stages of gelation.

The results presented in this section are related to the analysis performed in Section 3.10.1. Illustrating the total simulated flow rate solution proves impractical, as the duration of the cardiac cycle is significantly shorter than the total time domain simulated. Figure 77 illustrates the effect of the transient viscosity change on the flow rate toward the end of gelation. To better visualise the solution, the volume lost per cycle is computed and plotted for all solutions, as demonstrated in Figure 78. The volume lost per cycle investigated is the volume lost from the control volume currently under consideration and not necessarily from the myocardium. The findings indicate that, although flow rate behaviours differ across BCs, the volume loss per cycle remains consistent. An instability exists in the BC3 solution, which is discussed in Appendix J.

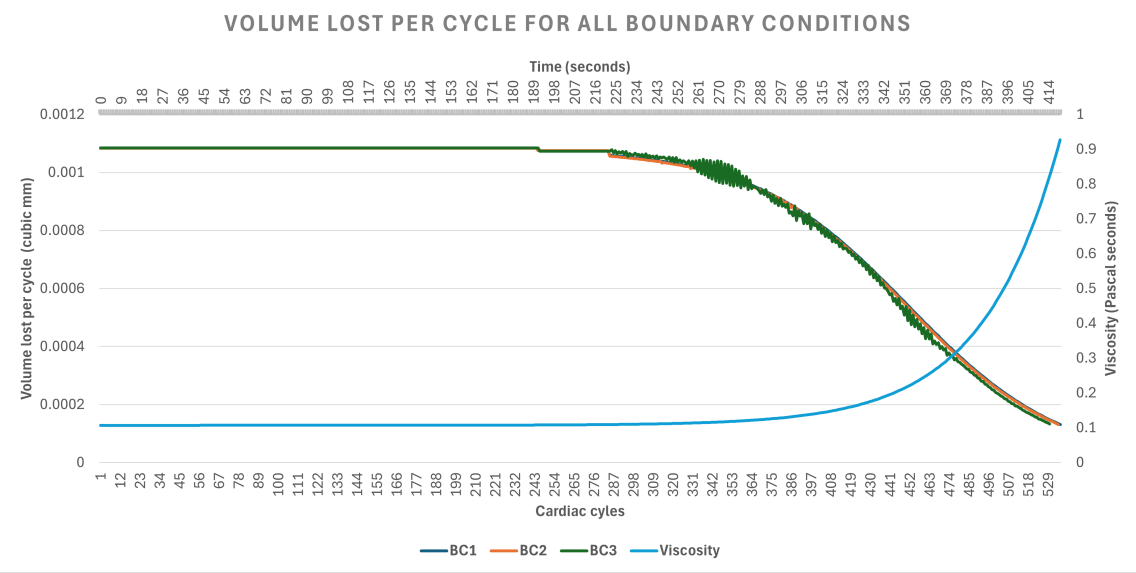

Figure 78: Plot of volume lost per cycle overlayed with the viscosity change over time using all BCs.

It is important to note that the results obtained for the volume lost per cycle is novel and is not present in the literature discussed in Section 2.6.2. The total volume of PEG lost from each solution can be determined by calculating the volume lost in each respective region. In the steady-viscosity regions, the volume lost per cycle is multiplied by the total number of cycles within that region. In the transient viscosity region, the volume loss is calculated by determining the area beneath the curve in the plot of the volumetric flow rate over time. The results for each solution are summarised in Table 17.

Solution	Volume for 1st steady region (0-190s)	Volume for 2nd steady region (190-220s)	Volume for transient region (220-417)	Total volume (mm^3)
BC1	245 cycles × 0.00108 mm^3 = **0.265** mm^3	39 cycles × 0.00107 mm^3 = **0.0419** mm^3	252 cycles, **0.176** mm^3	0.483
BC2	244 cycles × 0.00108 mm^3 = **0.259** mm^3	40 cycles × 0.00107 mm^3 = **0.0430** mm^3	251 cycles, **0.175** mm^3	0.482
BC3	245 cycles × 0.00106 mm^3 = **0.264** mm^3	40 cycles × 0.00105 mm^3 = **0.0420** mm^3	252 cycles, **0.173** mm^3	0.474

Table 17: Volume lost in each region of the viscosity change for all solutions.

Using the volume lost per cycle for any one solution and the volume of the simulated domain (0.0197 mm^3), another result can be visualised. The plot of loss per cycle as a percentage of the total fluid volume can be presented over time. This is illustrated in Figure 79 which shows that while the viscosity is low during the initial stages of gelation, 5% of the domain is expelled per cardiac cycle. This quickly drops to 2.5% with a slight increase in viscosity. In the later stages of gelation, the loss per cycle appears to decelerate, as indicated by a change in the gradient, despite the viscosity increasing exponentially. This observation warrants further investigation into the mechanisms underlying the loss associated with the variation in viscosity.

The BC1 solution can be used and trimmed to the region where the viscosity change is transient. As illustrated in Figure 80, there is an inverse correlation between volume loss per cycle and viscosity. While they may seem to exhibit a linear relationship visually, a qualitative analysis is essential to understand the nature of the relationship between these two parameters.

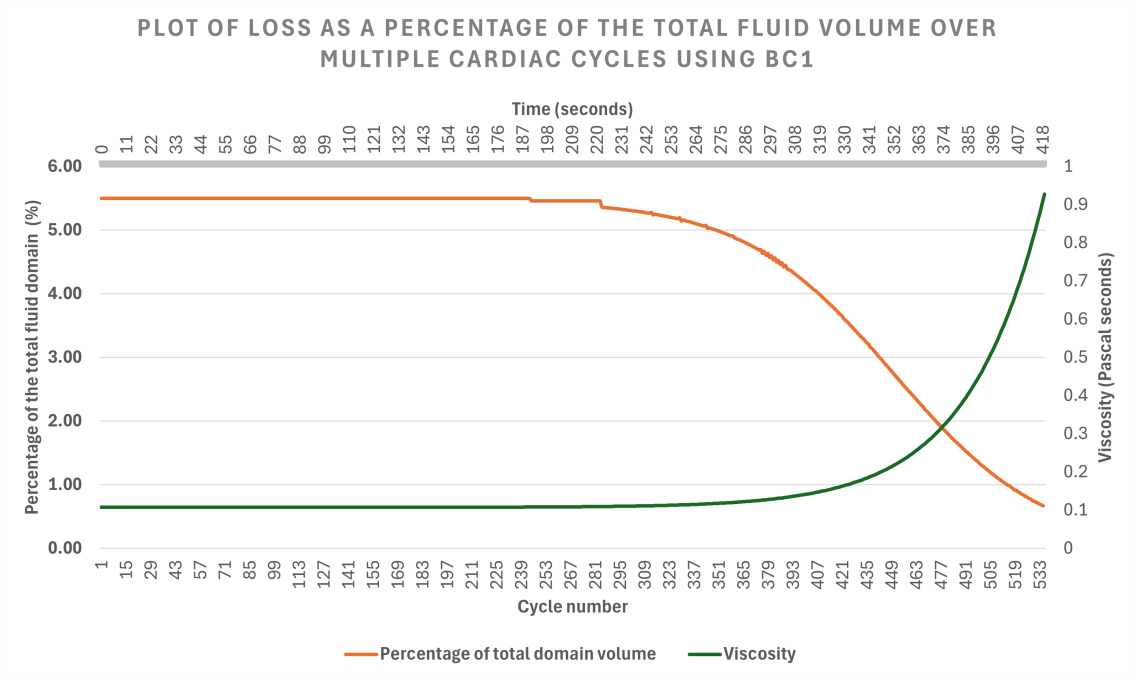

Figure 79: Plot of loss as a percentage of the domain volume over time using the BC1 solution.

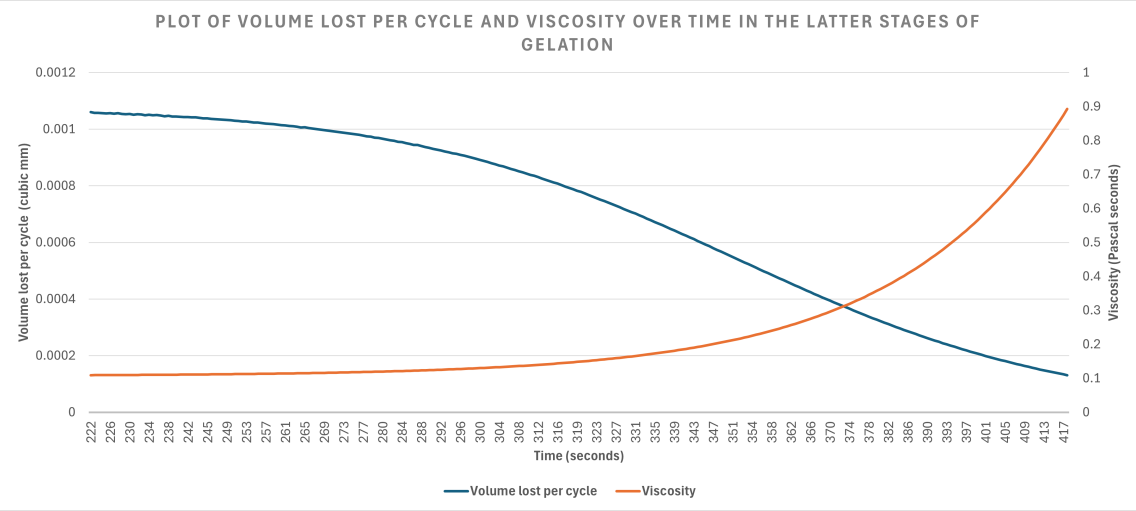

Figure 80: Plot of volume loss per cycle and viscosity over time.

The rate of change for each parameter can be calculated and used to analyse the kinetics of loss in response to variations in viscosity. The gradient of the viscosity

change can be readily determined, as it is already defined mathematically by an exponential function. The volume loss gradient per cycle can be derived by fitting a curve to the observed behaviour. This is achieved using a fourth-order polynomial, with details available in Appendix L. The function's derivative and the viscosity change gradient can be used for a more detailed behaviour analysis.

As illustrated in Figure 81, the viscosity gradient demonstrates a perfectly linear relationship when represented on a logarithmic scale. This observation aligns with the expectation that the gradient function behaves as a pure exponential function. The volume loss gradient per cycle initially increases with a slight rise in viscosity; however, with successive increases in viscosity, the gradient begins to decline. This can be interpreted as follows. During the initial stages of gelation, the volume lost per cycle decreases quickly. However, beyond a certain viscosity threshold, the rate of loss slows down. This suggests that, even if viscosity continues to rise, it does not further reduce the rate of loss. However, maintaining a higher viscosity at the end of gelation remains advantageous, since the loss per cycle falls below 1% of the domain volume, indicating good retention.

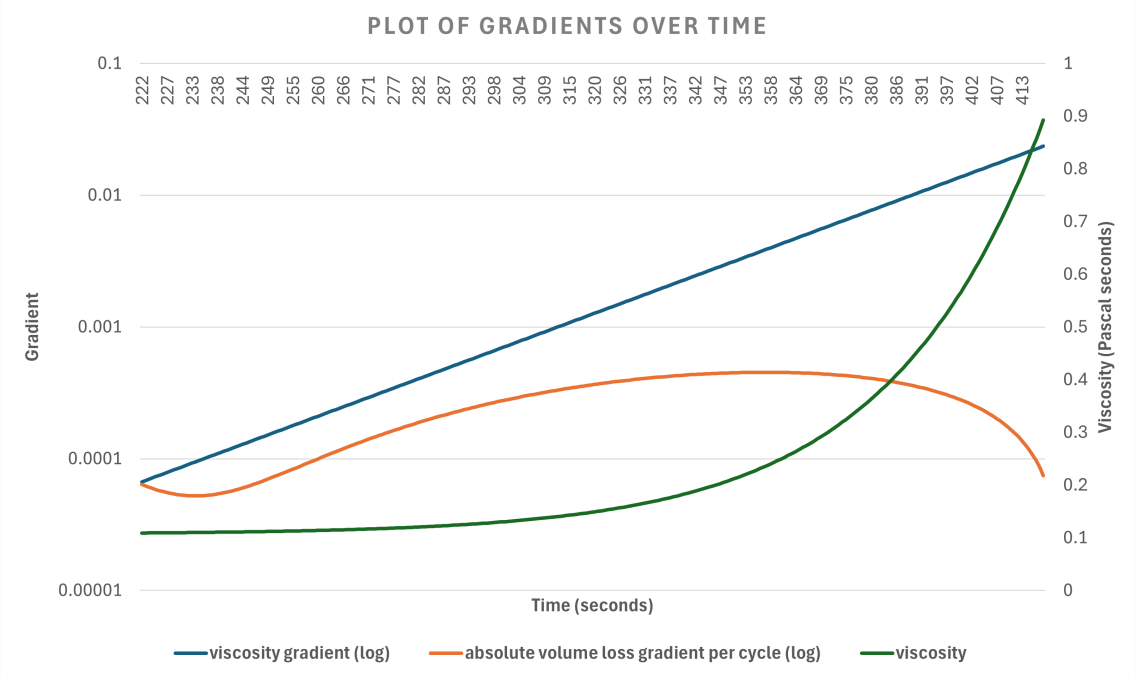

Figure 81: Plots of the viscosity gradient and the volume loss gradient per cycle over time.

Using this result, one can plot the gradients against each other within the same time

domain. Figure 82 further illustrates the results presented in Figure 81.

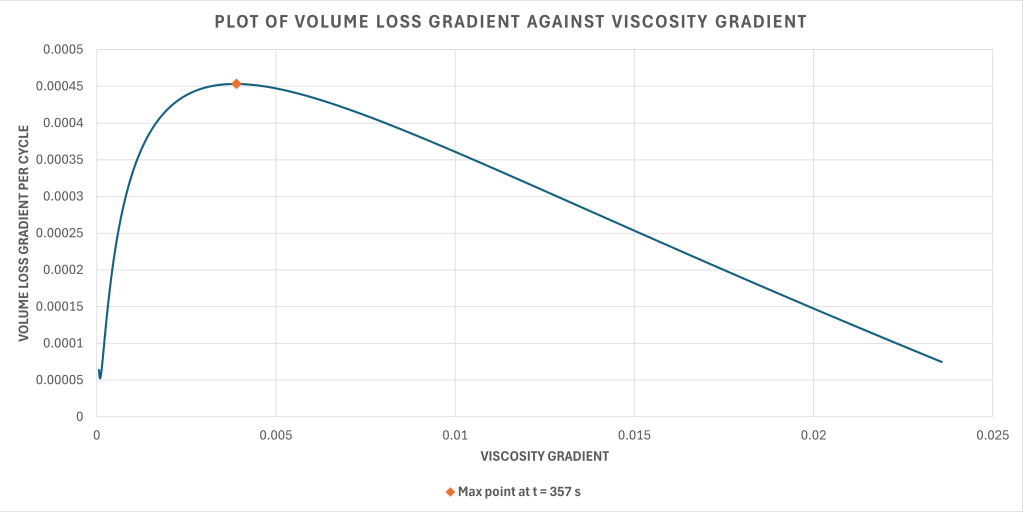

Figure 82: Plot of volume loss gradient against viscosity gradient showing the time at which the maximum occurs.

A maximum is observed for the volume loss gradient per cycle, occurring at a time of 357 s. This corresponds to a viscosity of 0.24 $Pa \cdot s$. Beyond this point, as the viscosity gradient increases, the rate of volume loss per cycle decreases. Furthermore, it is worth mentioning the relationship between the two parameters both prior to and following this maximum point. Before the volume loss gradient reaches its maximum, the relationship is nonlinear; subsequently, it becomes linear. It is uncertain whether this behaviour is domain-specific or is an inherent property of gel flow because of increasing viscosity. To investigate this, the same experiment is conducted using a simplified geometry.

4.3.2 Gelling results for a simple 3D geometry

The results presented in this section are related to the analysis performed in Section 3.10.2. Figure 83 below illustrates the volume lost per cycle and the evolution of viscosity over time. The findings show similarities with the previous case study that involves complex geometry. As seen in Figure 80 earlier, there is a difference in the magnitude of the volume lost per cycle; however, the behaviour is consistent. Initially, an increase in viscosity causes a rise in the rate of the volume loss per cycle; however, with successive increments in viscosity, this rate diminishes.

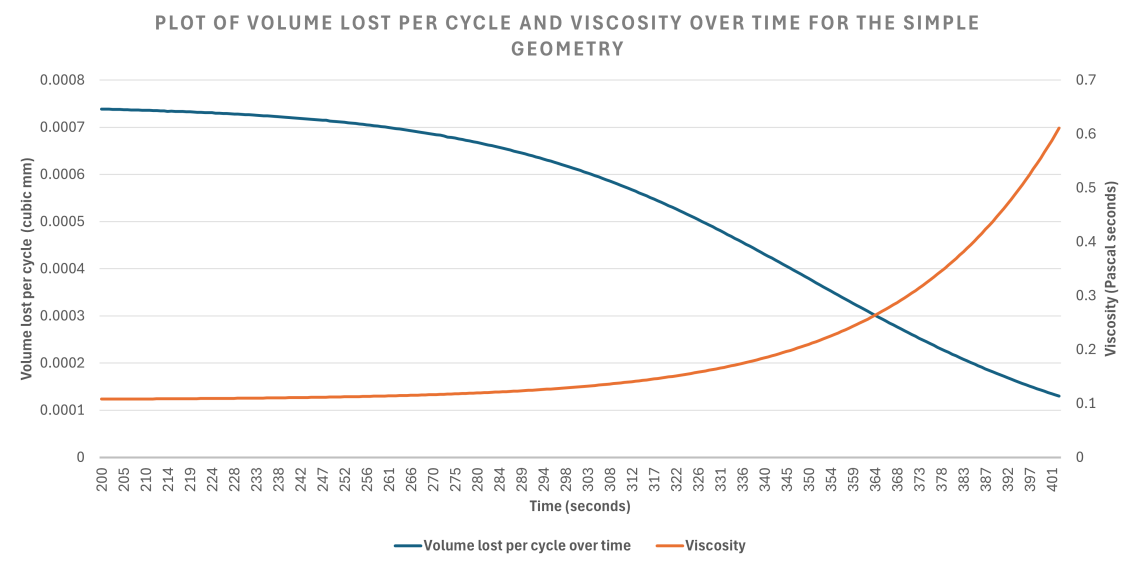

Figure 83: Plot of volume lost per cycle and viscosity change over time using BC1 and the simple geometry.

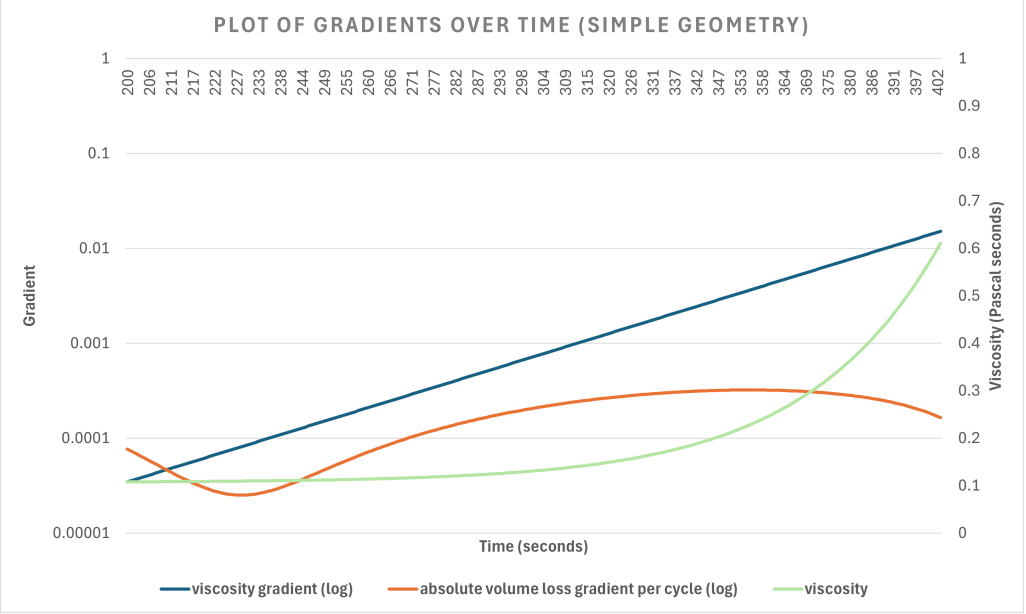

Figure 84: Plot of viscosity gradient and the volume loss gradient per cycle over time for the simpler geometry.

Recalling the analysis performed for the preceding case study, the gradients of each curve can be analysed. The curve representing the volume lost per cycle is again

approximated using a fourth-order polynomial. Its gradient can be computed and plotted alongside the viscosity gradient. Figure 84 above illustrates the gradients plotted on a logarithmic scale, and their behaviour aligns with the observations made in the previous case study.

The gradients can be plotted against one another, as illustrated in Figure 85. The results from the previous case study is included for comparative analysis. This particular behaviour proves to be consistent across various geometries. The peak magnitude differences in the volume loss gradient can be attributed to the initial gelation volume loss per cycle. The simple geometry starts with a lower volume than the complex geometry. A peak occurs at 357 s for the complex geometry and 355 s for the simple geometry. These peaks correspond to viscosities of 0.24 Pa·s and 0.23 Pa·s, respectively.

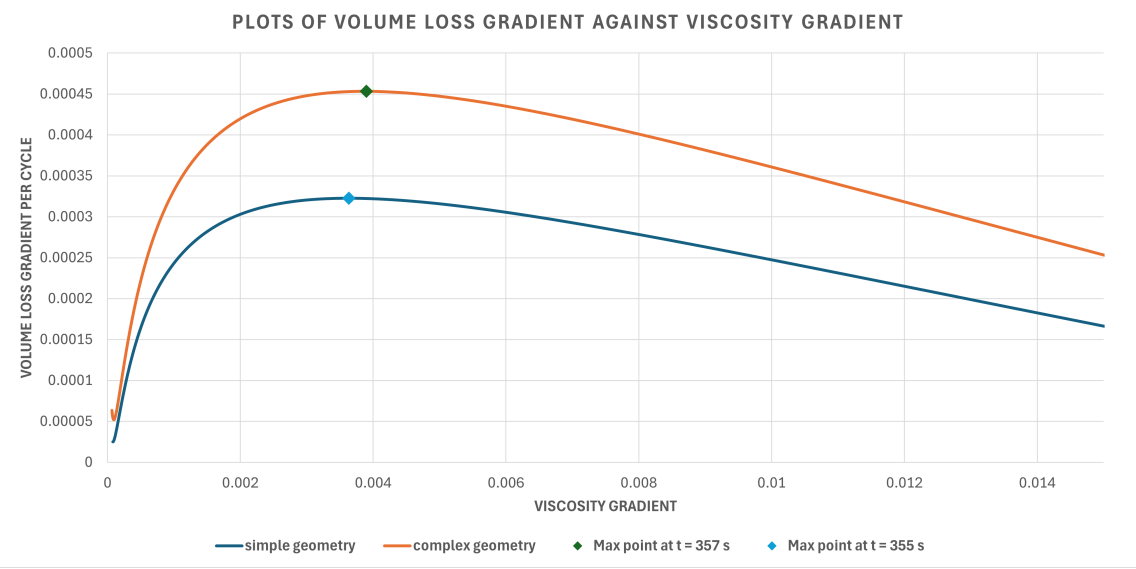

Figure 85: Plot of volume loss gradient against viscosity gradient for both geometries. The times at which the maximum occurs for both are also highlighted.

From this result, it can be deduced that during the gelation process, as the viscosity increases over time until it reaches 0.23 Pa.s, the volume lost per cycle decreases rapidly. After 0.23 Pa.s, the volume lost per cycle slows down regardless of the rapid increase in viscosity. Further investigation into this behaviour could aid efforts to improve understanding of mechanisms of loss. The findings from these two case studies provide valuable insights into the injection and gel development processes.

5 Conclusion and Recommendations

Reiterating the hypothesis and research aim articulated in the introduction:

- Hypothesis - Most significant PEG losses occur during the gelation phase following its injection.
- Research aim - To model the behaviour of PEG present in myocardial tissue as it undergoes a phase change due to gelation.

The outcomes presented in the preceding chapter provide the following brief insights:

- If the gel injected into the myocardium remains as a liquid at its starting viscosity for a long period of time, there are significant losses of it. While it is at its base viscosity, about 5% of the total domain volume flows per cardiac cycle. In a period of about 200 seconds, encompassing 300 cardiac cycles, this occurrence confirms the hypothesis stated above.

The results can be used in more detailed discussions than those presented above. These discussions can be outlined as follows: PEG gelling behaviour within the myocardium, gel development and administration methods, and recommendations for future modelling.

5.1 PEG gelling behaviour within the myocardium

The first case study shows that the volumetric flow rate results are consistent, irrespective of the BC used. Therefore, any of the results can be used for further discussion. The gelation of PEG can be broadly characterised into two distinct regions: a steady-state region and a transient region of viscosity change. In the steady-state region, the viscosity remains around 0.1 $Pa \cdot s$. During the transient region, the viscosity increases from 0.1 $Pa \cdot s$ to 1 $Pa \cdot s$.

The steady region occurs over a period of about 220 s. During this time, a considerable volume of PEG flows out of the domain relative to the total volume of the domain. Referencing the BC1 result in Table 17, the volume lost during the steady region is 0.31 mm^3 which is approximately **15** times the volume of the domain. The transient region occurs over a period of about 200 s, during which there is also a significant loss of PEG. The volume lost during the transient region is 0.18 mm^3 and this is approximately **9** times the volume of the domain.

Upon reviewing the plot of loss as a percentage of the domain volume in Figure 79, it can be observed that the volume lost per cardiac cycle remains approximately 5%. This consistency is maintained for about 275 s, encompassing 350 cardiac cycles.

During the period of transient viscosity change, the volume lost per cycle decreases from 5% to below 1%, indicating effective retention towards the end of gelation.

Analysing the rates of change in volume loss per cycle and viscosity change over time reveals that the rate of volume loss per cycle varies between a threshold viscosity. The results of the second case study confirm that this threshold viscosity is approximately 0.23 $Pa \cdot s$. Below this threshold, the volume lost per cycle decreases sharply as viscosity increases. Above this threshold, the volume lost per cycle slowly declines, even as viscosity continues to increase.

5.2 Gel development and administration methods

Considerations can be made to minimise the losses of PEG. In terms of gel development, gels could be designed to gel faster. As discussed in Section 5.1, as the viscosity increases from 0.1 $Pa \cdot s$ to 0.23 $Pa \cdot s$, the volume lost per cycle decreases rapidly. It is ideal to achieve this change as quickly as possible, but it currently occurs in approximately 130 seconds during the transient change in viscosity. Therefore, it is recommended to design the gel to undergo gelation faster.

Looking back again at the result in Figure 79, it can be posited that to minimise the overall loss of PEG, it should be injected when its viscosity is 0.5 $Pa \cdot s$. At this viscosity, the volume lost per cycle is approximately 1% of the total volume domain, which is ideal because the losses are minimal. However, in injectability studies ([65], [66]), the upper limit of viscosity is seen to be 0.1 $Pa \cdot s$ and this is the starting viscosity of the gelation of PEG. Therefore, it is still necessary to inject PEG while it is 0.1 $Pa \cdot s$.

Given that the gel must be injected at a viscosity of 0.1 $Pa \cdot s$, recommendations can be made regarding the administration method. The loss during the transient change in viscosity is unavoidable, as the gel needs to be injected at this specific viscosity. However, the injection can be optimally timed so that it is done closer to the onset of viscosity increase. This approach allows for the minimisation of losses during the phase when the viscosity remains constant. Injecting PEG 200 seconds after the onset of gelation results in a 55% reduction in the total volume lost during the gelation process.

5.3 Future modelling recommendations

The implemented methodology can be further extended to investigate different aspects related to PEG loss. An area of interest is the location of the injection site and its effect on the experienced losses. Referencing Section 3.8.1, the traction response is derived from the PEG present in the myocardium. As seen in Figure 40, there is

a variation in the magnitude of traction based on the location of the measurement. The region near the bottom exhibited greater traction than the region at the top.

Following this logic, it can be hypothesised that the flow rate of PEG will vary according to its location within the heart. The FSI model described in Section 3.7.1 can be used within the current methodology to examine the variation of flow rate in different areas of the heart. The flow rate result can be used to derive traction BCs, as detailed in Section 3.8, and to analyse the effect of gelation on flow rate in different regions of the heart.

Another area that can be explored is the incorporation of shear thinning in the gelation model. The results of the initial case study indicate that the volume lost per cycle remains consistent across various BCs. However, if a shear thinning material is used and varying shear rates are introduced because of different traction BCs, the flow rates would vary. This variation may ultimately result to differences when calculating the volume lost per cycle. Such an implementation could potentially be achieved in Ansys Polyflow by using the power law material model. The shear thinning index could be set to a constant value, while the consistency index can be assigned a time dependence to increase the viscosity over time as a result of gelation.

Lastly, another area that can be explored is the application of gelling material models within an FSI model. The FSI model discussed in Section 3.7.1 used a shear-thinning material model implemented in Ansys Fluent. The gelling material model can be configured in Fluent as outlined in Appendix C. This approach may yield improved insights into the flow rate behaviour during gelation, compared to the simplifications made using the rigid CFD model implemented in this project.

References

[1] "Coronary artery disease," [Online]. Available: https://my.clevelandclinic.org/health/diseases/16898-coronary-artery-disease, 2023, accessed: January 15, 2025.

[2] E. L. Ongstad and R. G. Gourdie, "Can heart function lost to disease be regenerated by therapeutic targeting of cardiac scar tissue?" *Seminars in Cell & Developmental Biology*, vol. 58, pp. 41–54, 2016, cardiac Regeneration Signaling in Cancer Initiation and Development. [Online]. Available: https://www.sciencedirect.com/science/article/pii/S1084952116301525

[3] W. H. Federation, "World heart report 2023," [Online]. Available: https://world-heart-federation.org/wp-content/uploads/World-Heart-Report-2023.pdf, accessed: January 15, 2025.

[4] W. H. O. (WHO), "Health data overview for the republic of south africa," [Online]. Available: https://data.who.int/countries/710, accessed: May 21, 2025.

[5] O. J. Mechanic, M. Gavin, S. A. Grossman, and K. Ziegler, *Acute Myocardial Infarction (Nursing)*. Treasure Island (FL): StatPearls Publishing, 2023, updated 2023 Sep 3. [Online]. Available: https://www.ncbi.nlm.nih.gov/books/NBK568759/.

[6] J. Leor, S. Tuvia, V. Guetta, F. Manczur, D. Castel, U. Willenz, Örs Petneházy, N. Landa, M. S. Feinberg, E. Konen, O. Goitein, O. Tsur-Gang, M. Shaul, L. Klapper, and S. Cohen, "Intracoronary injection of in situ forming alginate hydrogel reverses left ventricular remodeling after myocardial infarction in swine," *Journal of the American College of Cardiology*, vol. 54, no. 11, pp. 1014–1023, 2009. [Online]. Available: https://www.sciencedirect.com/science/article/pii/S0735109709020609

[7] S. M. Dorsey, J. R. McGarvey, H. Wang, A. Nikou, L. Arama, K. J. Koomalsingh, N. Kondo, J. H. r. Gorman, J. J. Pilla, R. C. Gorman, J. F. Wenk, and J. A. Burdick, "Mri evaluation of injectable hyaluronic acid-based hydrogel therapy to limit ventricular remodeling after myocardial infarction," *Biomaterials*, vol. 69, pp. 65–75, Nov 2015.

[8] K. Kadner, S. Dobner, T. Franz, D. Bezuidenhout, M. S. Sirry, P. Zilla, and N. H. Davies, "The beneficial effects of deferred delivery on the efficiency of hydrogel therapy post myocardial infarction," *Biomaterials*, vol. 33, no. 7, pp. 2060–2066, 2012. [Online]. Available: https://www.sciencedirect.com/science/article/pii/S0142961211013858

[9] N. Frey, A. Linke, T. Süselbeck, J. Müller-Ehmsen, P. Vermeersch, D. Schoors, M. Rosenberg, F. Bea, S. Tuvia, and J. Leor, "Intracoronary delivery of injectable bioabsorbable scaffold (ik-5001) to treat left ventricular remodeling after st-elevation myocardial infarction," *Circulation: Cardiovascular Interventions*, vol. 7, no. 6, pp. 806–812, 2014. [Online]. Available: https://www.ahajournals.org/doi/abs/10.1161/CIRCINTERVENTIONS.114.001478

[10] J. N. Anderl, T. E. Robey, P. S. Stayton, and C. E. Murry, "Retention and biodistribution of microspheres injected into ischemic myocardium," *Journal of Biomedical Materials Research Part A*, vol. 88A, no. 3, pp. 704–710, 2009. [Online]. Available: https://onlinelibrary.wiley.com/doi/abs/10.1002/jbm.a.31917

[11] K. Malliaras, M. Kreke, and E. Marbán, "The stuttering progress of cell therapy for heart disease," *Clinical Pharmacology & Therapeutics*, vol. 90, no. 4, pp. 532–541, 2011. [Online]. Available: https://ascpt.onlinelibrary.wiley.com/doi/abs/10.1038/clpt.2011.175

[12] M. Ngoepe, A. Passos, S. Balabani, J. King, A. Lynn, J. Moodley, L. Swanson, D. Bezuidenhout, N. H. Davies, and T. Franz, "A preliminary computational investigation into the flow of peg in rat myocardial tissue for regenerative therapy," *Frontiers in Cardiovascular Medicine*, vol. 6, 2019. [Online]. Available: https://www.frontiersin.org/articles/10.3389/fcvm.2019.00104

[13] A. Janse van Rensburg, "Heparinoid hydrogels for cardiovascular tissue regeneration," Ph.D. dissertation, University of Cape Town, 2015. [Online]. Available: https://open.uct.ac.za/bitstream/handle/11427/16695/thesis_hsf_2015_janse_van_rensburg_aliza.pdf?sequence=1&isAllowed=y

[14] WebMD, "Heart attack," [Online]. Available: https://www.webmd.com/heart-disease/heart-disease-heart-attacks, accessed: January 15, 2025.

[15] D. L. Kasper, A. S. Fauci, S. L. Hauser, D. L. Longo, J. L. Jameson, and J. Loscalzo, *Harrisons Manual of Medicine, 19th Edition.* McGraw Hill Professional, 2016.

[16] N. B. A. Ntusi and B. M. Mayosi, "Epidemiology of heart failure in sub-saharan africa," *Expert Review of Cardiovascular Therapy*, vol. 7, no. 2, pp. 169–180, 2009, pMID: 19210213. [Online]. Available: https://doi.org/10.1586/14779072.7.2.169

[17] B. J. North and D. A. Sinclair, "The intersection between aging and cardiovascular disease," *Circulation Research*, vol. 110, no. 8, pp. 1097–1108,

2012. [Online]. Available: https://www.ahajournals.org/doi/abs/10.1161/CIRCRESAHA.111.246876

[18] M. F. Ranthe, J. A. Petersen, H. Bundgaard, J. Wohlfahrt, M. Melbye, and H. A. Boyd, "A detailed family history of myocardial infarction and risk of myocardial infarction – a nationwide cohort study," *PLOS ONE*, vol. 10, no. 5, pp. 1–11, 05 2015. [Online]. Available: https://doi.org/10.1371/journal.pone.0125896

[19] N. H. S. (NHS), "Causes - coronary heart disease," [Online]. Available: https://www.nhs.uk/conditions/coronary-heart-disease/causes/, accessed: January 24, 2025.

[20] C. for Disease Control and P. (CDC), "Smoking and heart disease, stroke, and peripheral artery disease," [Online]. Available: https://www.cdc.gov/tobacco/campaign/tips/diseases/heart-disease-stroke.html, accessed: January 15, 2025.

[21] D. E. Warburton, C. W. Nicol, and S. S. Bredin, "Health benefits of physical activity: the evidence," *Cmaj*, vol. 174, no. 6, pp. 801–809, 2006.

[22] C. for Disease Control and P. (CDC), "About high blood pressure," [Online]. Available: https://www.cdc.gov/high-blood-pressure/about/?CDC_AAref_Val=https://www.cdc.gov/bloodpressure/about.htm, accessed: January 15, 2025.

[23] S. F. Vatner, J. Zhang, C. Vyzas, K. Mishra, R. M. Graham, and D. E. Vatner, "Vascular stiffness in aging and disease," *Frontiers in Physiology*, vol. 12, 2021. [Online]. Available: https://www.frontiersin.org/journals/physiology/articles/10.3389/fphys.2021.762437

[24] H. Marks, "The heart beats again," [Online]. Available: https://www.aiche.org/chenected/2012/02/heart-beats-again, 2012, accessed: January 15, 2025.

[25] W. J. Richardson, S. A. Clarke, T. A. Quinn, and J. W. Holmes, *Physiological Implications of Myocardial Scar Structure*. John Wiley & Sons, Ltd, 2015, pp. 1877–1909. [Online]. Available: https://onlinelibrary.wiley.com/doi/abs/10.1002/cphy.c140067

[26] D. L. Page, J. B. Caulfield, J. A. Kastor, R. W. DeSanctis, and C. A. Sanders, "Myocardial changes associated with cardiogenic shock," *New England Journal of Medicine*, vol. 285, no. 3, pp. 133–137, 1971.

[27] T. Kumanohoso, Y. Otsuji, S. Yoshifuku, K. Matsukida, C. Koriyama, A. Kisanuki, S. Minagoe, R. A. Levine, and C. Tei, "Mechanism of higher incidence of ischemic mitral regurgitation in patients with inferior myocardial

infarction: Quantitative analysis of left ventricular and mitral valve geometry in 103 patients with prior myocardial infarction," *The Journal of Thoracic and Cardiovascular Surgery*, vol. 125, no. 1, pp. 135–143, 2003. [Online]. Available: https://www.sciencedirect.com/science/article/pii/S0022522302733254

[28] E. M. Ahmed, "Hydrogel: Preparation, characterization, and applications: A review," *Journal of Advanced Research*, vol. 6, no. 2, pp. 105–121, 2015. [Online]. Available: https://www.sciencedirect.com/science/article/pii/S2090123213000969

[29] A. Gandin, Y. Murugesan, V. Torresan, L. Ulliana, A. Citron, P. Contessotto, G. Battilana, T. Panciera, M. Ventre, A. P. Netti, L. Nicola, S. Piccolo, and G. Brusatin, "Simple yet effective methods to probe hydrogel stiffness for mechanobiology," *Scientific Reports*, vol. 11, no. 1, 2021. [Online]. Available: https://doi.org/10.1038/s41598-021-01036-5

[30] A. V. Brikov, A. N. Markin, and S. V. Sukhoverkhov, "Rheological properties of polyethylene glycol solutions and gels," *Ind Chem*, vol. 1, p. 102, 2015.

[31] L. Shah and T. Rehman, "Synthesis of graphene oxide doped poly(2-acrylamido-2-methyl propane sulfonic acid) composite hydrogel with pseudo-plastic thixotropic behavior," *Polymer Bulletin*, vol. 77, 08 2020.

[32] C. Fruijtier-Pölloth, "Safety assessment on polyethylene glycols (pegs) and their derivatives as used in cosmetic products," *Toxicology*, vol. 214, no. 1, pp. 1–38, 2005. [Online]. Available: https://www.sciencedirect.com/science/article/pii/S0300483X05002696

[33] MERCK, "Polyethylene glycol," [Online]. Available: https://www.sigmaaldrich.com/ZA/en/substance/polyethyleneglycol1234525322683, accessed: January 15, 2025.

[34] P. Dontula, C. W. Macosko, and L. E. Scriven, "Model elastic liquids with water-soluble polymers," *AIChE Journal*, vol. 44, no. 6, pp. 1247–1255, 1998. [Online]. Available: https://aiche.onlinelibrary.wiley.com/doi/abs/10.1002/aic.690440603

[35] S. Baldursdottir, F. Tian, B. G. Santacruz, A. C. Jørgensen, and J. Rantanen, "The influence of thermal history on the physical behavior of poly(ethylene glycol) (peg)," *Pharmaceutical Development and Technology*, vol. 17, no. 2, pp. 195–203, 2012, pMID: 21077753. [Online]. Available: https://doi.org/10.3109/10837450.2010.531733

[36] B. P. Chan and K. W. Leong, "Scaffolding in tissue engineering: general approaches and tissue-specific considerations," *European Spine*

Journal, vol. 17, no. 4, pp. 467–479, 2008. [Online]. Available: https://doi.org/10.1007/s00586-008-0745-3

[37] L. E. Freed, G. C. Engelmayr Jr., J. T. Borenstein, F. T. Moutos, and F. Guilak, "Advanced material strategies for tissue engineering scaffolds," *Advanced Materials*, vol. 21, no. 32-33, pp. 3410–3418, 2009. [Online]. Available: https://advanced.onlinelibrary.wiley.com/doi/abs/10.1002/adma.200900303

[38] N. Davies, K. Goetsch, M. Ngoepe, T. Franz, and S. Lecour, "Cardiac stem cell therapy," in *Stem Cell Biology and Regenerative Medicine*, R. Madonna, Ed. Springer, 2016, pp. 165–190.

[39] M. Arnal-Pastor, J. C. Chachques, M. M. Pradas, and A. Vallés-Lluch, "Biomaterials for cardiac tissue engineering," in *Regenerative Medicine and Tissue Engineering*, J. A. Andrades, Ed. Rijeka: IntechOpen, 2013, ch. 12. [Online]. Available: https://doi.org/10.5772/56076

[40] A. Mathur and J. Martin, "Stem cells and repair of the heart," *The Lancet*, vol. 364, no. 9429, pp. 183–192, 2004. [Online]. Available: https://www.sciencedirect.com/science/article/pii/S0140673604166324

[41] F. J. O'Brien, "Biomaterials & scaffolds for tissue engineering," *Materials Today*, vol. 14, no. 3, pp. 88–95, 2011. [Online]. Available: https://www.sciencedirect.com/science/article/pii/S136970211170058X

[42] D. Saha and S. Bhattacharya, "Hydrocolloids as thickening and gelling agents in food: a critical review," *Journal of Food Science and Technology*, vol. 47, no. 6, pp. 587–597, 2010.

[43] S. K. H. Gulrez, S. Al-Assaf, and G. O. Phillips, "Hydrogels: Methods of preparation, characterisation and applications," in *Progress in Molecular and Environmental Bioengineering*, A. Carpi, Ed. Rijeka: IntechOpen, 2011, ch. 5. [Online]. Available: https://doi.org/10.5772/24553

[44] E. Budianto, S. Muthoharoh, and N. M. Nizardo, "Effect of crosslinking agents, ph and temperature on swelling behavior of cross-linked chitosan hydrogel," *Asian Journal of Applied Sciences*, vol. 03, pp. 581–588, 10 2015.

[45] F. Yang, C. Guo, M. Zhang, B. Bhandari, and Y. Liu, "Improving 3d printing process of lemon juice gel based on fluid flow numerical simulation," *LWT*, vol. 102, pp. 89–99, 2019. [Online]. Available: https://www.sciencedirect.com/science/article/pii/S0023643818310892

[46] T. Instruments, "Rheology: Basic theory & applications training,"

[Online]. Available: https://www.tainstruments.com/online-training-course-downloads/, accessed: January 15, 2025.

[47] M. Khan and Hashim, "Boundary layer flow and heat transfer to carreau fluid over a nonlinear stretching sheet," *AIP Advances*, vol. 5, no. 10, p. 107203, 10 2015. [Online]. Available: https://doi.org/10.1063/1.4932627

[48] I. Yu and R. Chen, "An experimental and numerical study on coaxial extrusion of a non-newtonian hydrogel material," *Journal of Manufacturing Science and Engineering*, vol. 143, no. 8, p. 081008, 03 2021. [Online]. Available: https://doi.org/10.1115/1.4050181

[49] HEC-RAS, "Herschel-bulkley parameters," [Online]. Available: https://www.hec.usace.army.mil/confluence/rasdocs/rasmuddebris/non-newtonian-user-s-manual/user-inputs-and-model-parameters/hershel-bulkley-parameters, accessed: January 15, 2025.

[50] S. Dobner, D. Bezuidenhout, P. Govender, P. Zilla, and N. Davies, "A synthetic non-degradable polyethylene glycol hydrogel retards adverse post-infarct left ventricular remodeling," *Journal of Cardiac Failure*, vol. 15, no. 7, pp. 629–636, 2009. [Online]. Available: https://doi.org/10.1016/j.cardfail.2009.03.003

[51] X.-J. Jiang, T. Wang, X.-Y. Li, D.-Q. Wu, Z.-B. Zheng, J.-F. Zhang, J.-L. Chen, B. Peng, H. Jiang, C. Huang, and X.-Z. Zhang, "Injection of a novel synthetic hydrogel preserves left ventricle function after myocardial infarction," *Journal of Biomedical Materials Research Part A*, vol. 90A, no. 2, pp. 472–477, 2009. [Online]. Available: https://onlinelibrary.wiley.com/doi/abs/10.1002/jbm.a.32118

[52] M. Morita, C. Eckert, K. Matsuzaki, M. Noma, L. Ryan, J. Burdick, B. Jackson, J. r. Gorman, M. Sacks, and R. Gorman, "Modification of infarct material properties limits adverse ventricular remodeling," *Annals of Thoracic Surgery*, vol. 92, no. 2, pp. 617–624, Aug 2011.

[53] J. F. Wenk, P. Eslami, Z. Zhang, C. Xu, E. Kuhl, J. H. G. III, J. D. Robb, M. B. Ratcliffe, R. C. Gorman, and J. M. Guccione, "A novel method for quantifying the in-vivo mechanical effect of material injected into a myocardial infarction," *The Annals of Thoracic Surgery*, vol. 92, no. 3, pp. 935–941, 2011. [Online]. Available: https://doi.org/10.1016/j.athoracsur.2011.04.089

[54] A. B. C. Dang, J. M. Guccione, J. M. Mishell, P. Zhang, A. W. Wallace, R. C. Gorman, J. H. Gorman, and M. B. Ratcliffe, "Akinetic myocardial infarcts must contain contracting myocytes: finite-element model study," *American Journal of Physiology-Heart and Circulatory Physiology*, vol.

288, no. 4, pp. H1844–H1850, 2005, pMID: 15604126. [Online]. Available: https://doi.org/10.1152/ajpheart.00961.2003

[55] J. Kortsmit, N. H. Davies, R. Miller, J. R. Macadangdang, P. Zilla, and T. Franz, "The effect of hydrogel injection on cardiac function and myocardial mechanics in a computational post-infarction model," *Computer Methods in Biomechanics and Biomedical Engineering*, vol. 16, no. 11, pp. 1185–1195, 2013, pMID: 22439799. [Online]. Available: https://doi.org/10.1080/10255842.2012.656611

[56] Y. D. Motchon, K. L. Sack, M. S. Sirry, M. Kruger, E. Pauwels, D. Van Loo, A. De Muynck, L. Van Hoorebeke, N. H. Davies, and T. Franz, "Effect of biomaterial stiffness on cardiac mechanics in a biventricular infarcted rat heart model with microstructural representation of in situ intramyocardial injectate," *International Journal for Numerical Methods in Biomedical Engineering*, vol. 39, no. 5, p. e3693, 2023. [Online]. Available: https://onlinelibrary.wiley.com/doi/abs/10.1002/cnm.3693

[57] *ANSYS Polyflow User's Guide*, 2023rd ed., ANSYS, Inc., July 2023, user's Guide.

[58] G. B. Sands, D. A. Gerneke, D. A. Hooks, C. R. Green, B. H. Smaill, and I. J. Legrice, "Automated imaging of extended tissue volumes using confocal microscopy," *Microscopy Research and Technique*, vol. 67, no. 5, pp. 227–239, 2005. [Online]. Available: https://analyticalsciencejournals.onlinelibrary.wiley.com/doi/abs/10.1002/jemt.20200

[59] V. A. Maluleke, "In silico fluid-structure interaction study of the dispersion of injectable hydrogels in acutely infarcted myocardium," Ph.D. dissertation, University of Cape Town, Cape Town, South Africa, 2023.

[60] *ANSYS Polymat User's Guide*, 2023rd ed., ANSYS, Inc., July 2023, user's Guide.

[61] H. M. Laun, "Prediction of elastic strains of polymer melts in shear and elongation," *Journal of Rheology*, vol. 30, no. 3, pp. 459–501, 06 1986. [Online]. Available: https://doi.org/10.1122/1.549855

[62] W. P. Cox and E. H. Merz, "Correlation of dynamic and steady flow viscosities," *Journal of Polymer Science*, vol. 28, no. 118, pp. 619–622, 1958. [Online]. Available: https://onlinelibrary.wiley.com/doi/abs/10.1002/pol.1958.1202811812

[63] S. Y. Ho, "Anatomy and myoarchitecture of the left ventricular wall in normal

and in disease," *European Journal of Echocardiography*, vol. 10, no. 8, pp. iii3–iii7, 12 2009. [Online]. Available: https://doi.org/10.1093/ejechocard/jep159

[64] M. Usman, E. A. Mendiola, T. Mukherjee, R. R. Mehdi, J. Ohayon, P. G. Alluri, S. Sadayappan, G. Choudhary, and R. Avazmohammadi, "On the possibility of estimating myocardial fiber architecture from cardiac strains," *Functional Imaging and Modeling of the Heart*, vol. 13958, pp. 74–83, Jun 2023, epub 2023 Jun 16. [Online]. Available: https://doi.org/10.1007/978-3-031-35302-4_8

[65] R. P. Watt, H. Khatri, and A. R. Dibble, "Injectability as a function of viscosity and dosing materials for subcutaneous administration," *International Journal of Pharmaceutics*, vol. 554, pp. 376–386, 2019. [Online]. Available: https://www.sciencedirect.com/science/article/pii/S0378517318308305

[66] C. Zhao, Z. Zhu, X. Cao, F. Pan, F. Li, M. Xue, Y. Guo, Y. Zhao, J. Zeng, Y. Liu, Z. Yang, Y. Liu, F. Ren, and L. Feng, "Evaluation the injectability of injectable microparticle delivery systems on the basis of injection force and discharged rate," *European Journal of Pharmaceutics and Biopharmaceutics*, vol. 190, pp. 58–72, 2023. [Online]. Available: https://www.sciencedirect.com/science/article/pii/S0939641123001704

[67] P. J. Roache, "Perspective: A method for uniform reporting of grid refinement studies," *Journal of Fluids Engineering*, vol. 116, no. 3, pp. 405–413, 09 1994. [Online]. Available: https://doi.org/10.1115/1.2910291

Appendices

Appendix A

A Methodology for using viable periodic functions to generate results for unusable periodic functions

The following methodology is used to generate a result for a function that leads to numerical instabilities in the solver. The instability is mentioned in Section 3.6.2.3. Using the results visualised in Figure 60, the result of one periodic traction can be scaled to match the result of the other periodic traction. This can be achieved by using the ratio between the periodic functions. Given the linear relationship between traction and velocity, the function ratio can scale one function's average velocity to match the other. Figure 86 below shows the average velocity results overlayed with the ratio between the periodic functions calculated over time.

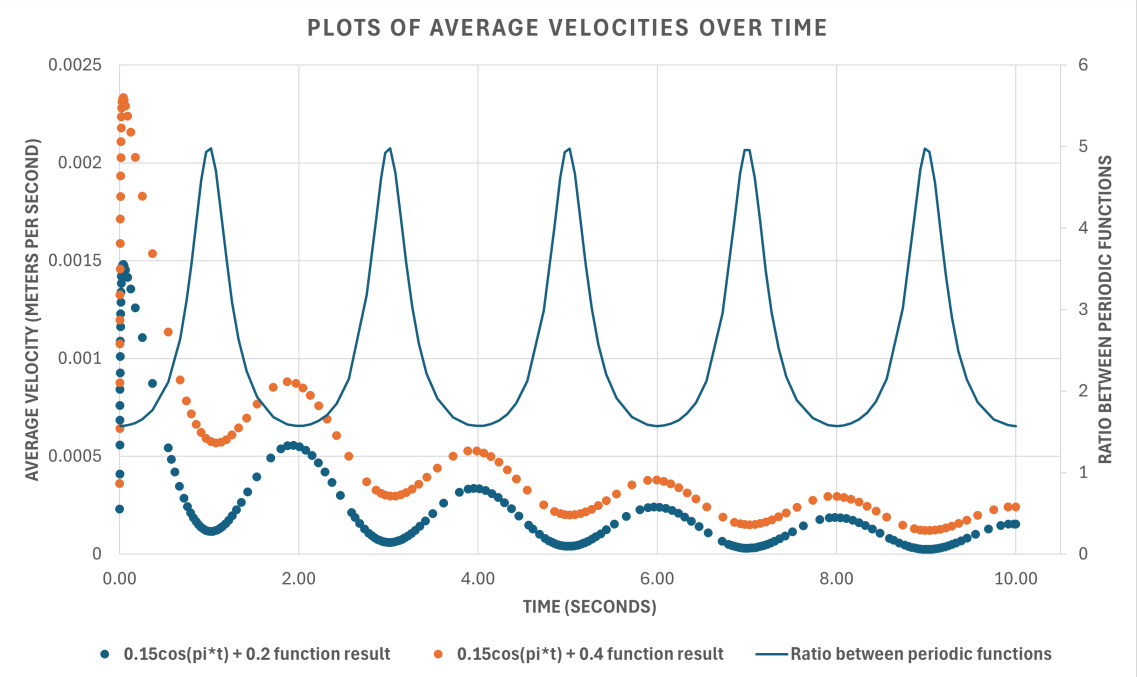

Figure 86: Plots of average velocity with an overlay of the ratio between the two periodic functions that were used to generate the results.

From Figure 86, the result obtained using $f_n = 0.15cos(\pi \cdot t) + 0.4\ Pa$ is scaled using the ratio at each time step. Figure 87 shows the comparison between an original

solution and a scaled solution. The result shows a near-perfect match between the solutions. The area under each curve was computed and compared. The areas were within 0.04% of each other. This method can be used confidently to extrapolate the results for a function that previously led to a failed simulation.

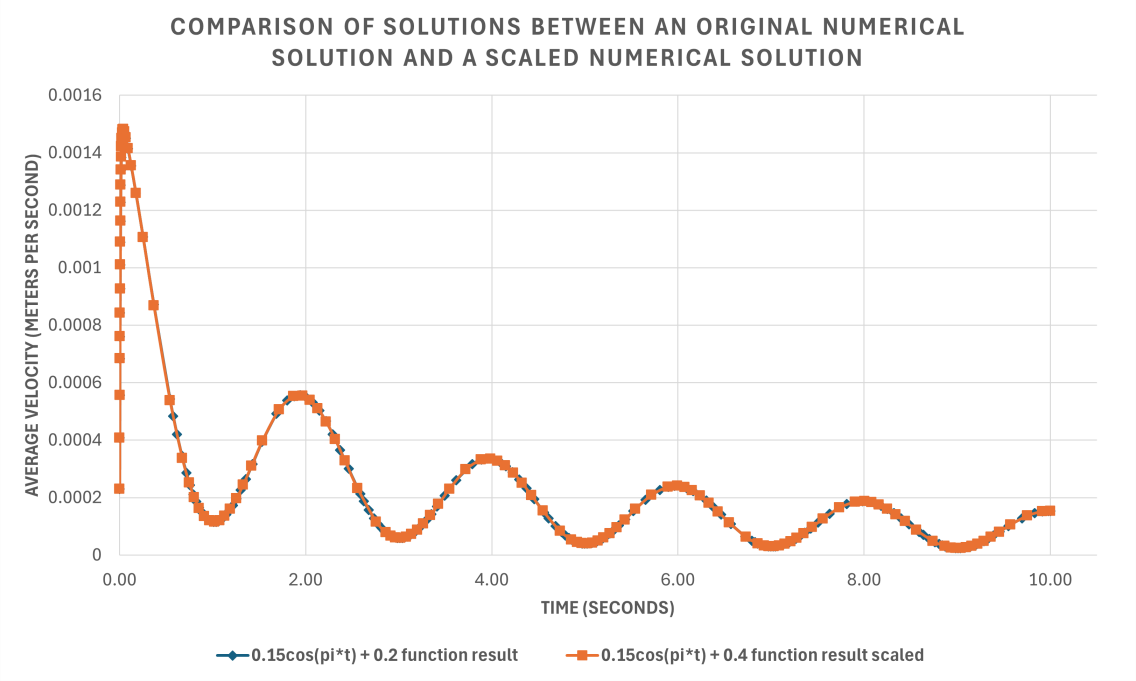

Figure 87: Plots of average velocity comparing the original solution and the scaled solution.

This can be extended to generate a result for a function that led to an instability. In Section 3.6.2.3, it was discovered that using the function $f_n = 0.15cos(\pi \cdot t) + 0.15\ Pa$ led to a failed simulation. Using the result of the function $f_n = 0.15cos(\pi \cdot t) + 0.2\ Pa$, the ratio between the two functions can be calculated and used to scale the existing solution to obtain the desired solution. This can be seen in Figure 88. The average velocity can be seen to approach 0 as the periodic function approaches 0 as well.

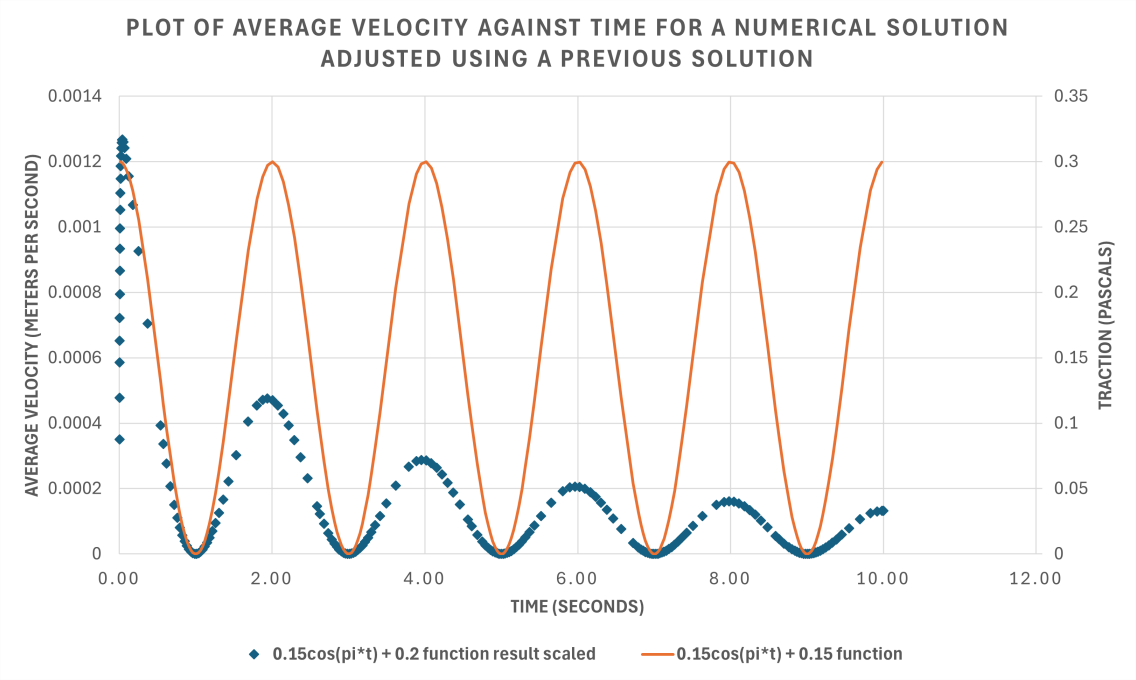

Figure 88: Plot of a scaled average velocity result for a periodic function that causes solver instability. Includes an overlay of the periodic function.

Appendix B

B Supporting calculations for proof of concept simulation

For a Hagen-Poiseuille flow, the pressure gradient between the inlet and the outlet is a constant value that is denoted by α. This pressure gradient can be related to the maximum velocity observed as follows:

$$v_{max} = \frac{\alpha d^2}{16\mu}, \tag{12}$$

where d is the diameter of the pipe and μ is the dynamic viscosity.

The viscosity, which is a function of time, is modelled as a ramp function that follows the equation:

$$\mu = 0.09t + 0.1Pa \cdot s\ . \tag{13}$$

In the simulation, the average velocity is maintained at 1 m/s and therefore, for a fully developed flow, the maximum velocity is maintained at 2 m/s. Maintaining this velocity requires the pressure difference to increase in line with viscosity, as pushing thicker fluid demands more effort. The relationship between viscosity and pressure difference is linear, as can be seen in equation 12.

Using the viscosity at the end of the simulation, α at the end of the simulation can be theoretically calculated as:

$$\alpha = \frac{v_{max} \cdot 16\mu}{d^2} = \frac{2 \cdot 16(1)}{0.004^2} = 2 \times 10^6 \text{ Pa/m}\ . \tag{14}$$

It is important to note that α is negative as the pressure drops from the inlet to the outlet. The "inlet" pressure is taken at a point 5 mm away from the inlet where the flow is fully developed as shown in Figure 89. The distance between this point and the outlet is 35 mm and the inlet average pressure can then be calculated as:

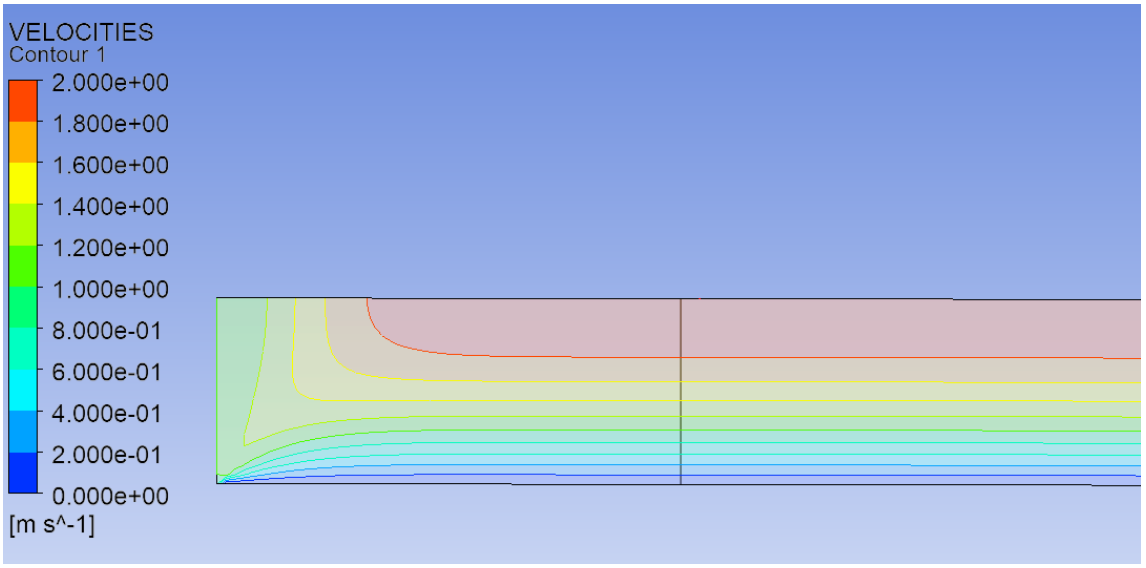

Figure 89: The line at which the average pressure is calculated. It can be seen that the flow is fully developed at this point.

$$\alpha = 2 \times 10^6 = -\frac{dP}{dz} = -\frac{outlet\ pressure - inlet\ pressure}{0.035}, \tag{15a}$$

$$inlet\ pressure = 2 \times 10^6 \times 0.035 = 70\ \text{kPa}\ . \tag{15b}$$

This can be compared with the numerical solution calculated in Polyflow for the average pressure at the end of the simulation, where $\mu = 1Pa \cdot s$. Figure 90 shows that at a point 5 mm away from the inlet, the average pressure is 70 kPa. This matches perfectly with the analytical solution at this point. The plot of average pressure across the length of the domain is also consistent with what was calculated in Fluent.

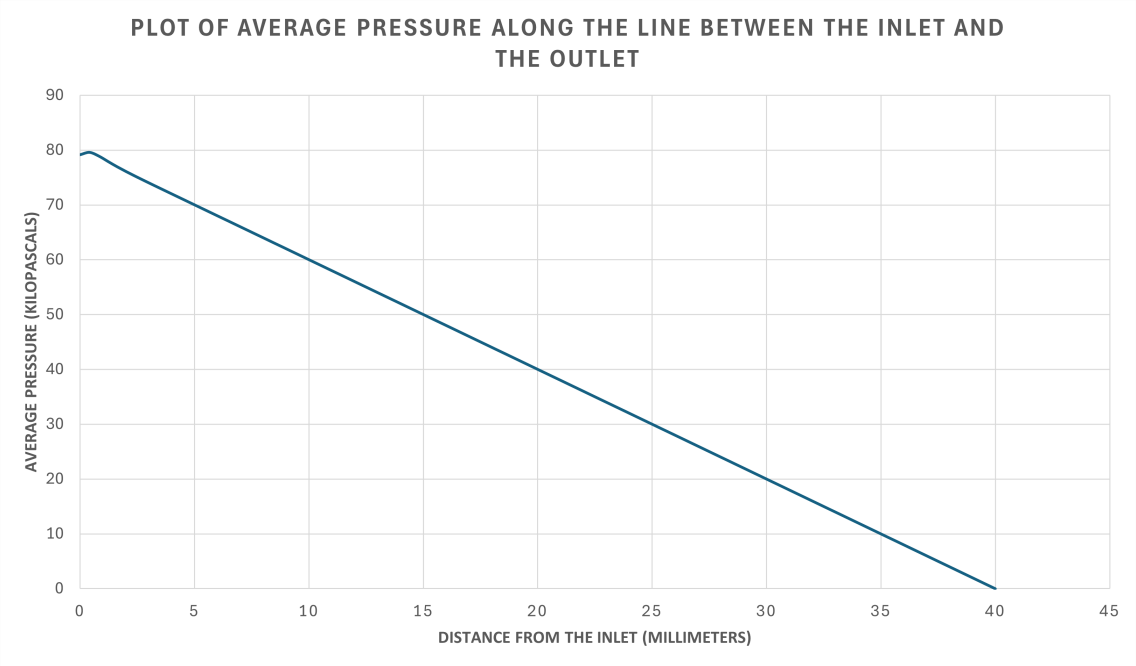

Figure 90: Plot of average pressure between the inlet and outlet, calculated in Polyflow.

Looking at equations 14 and 15a, the relationship between inlet pressure and viscosity is linear (as can be seen in equation 16). Therefore, a fluid with an increasing viscosity will cause the inlet pressure to increase linearly to maintain the same velocity.

$$inlet\ pressure = 2 \times 10^6 \times 0.035 \times \mu\ . \tag{16}$$

In equation 16, μ can be replaced by equation 13. This can be used to calculate the inlet pressure analytically for a Hagen-Poiseuille flow, while the viscosity increases with time and the inlet velocity is kept constant.

Appendix C

C Gelation done in Fluent

This code was interpreted in Fluent to implement a time-dependent viscosity model.

```
#include "udf.h"

DEFINE_PROPERTY(cell_viscosity,c,t)
{
real mu = 0.1;
real current_time = CURRENT_TIME;
mu =0.09*current_time + 0.1;
return mu;
}
```

Appendix D

D Further comparison of solutions computed in Polyflow and Fluent (RV-POC-ramp, RV-POC-per)

Following the analysis in Section 3.6.5, the complexity of the simulation is increased by implementing a time-dependent velocity. The simulation parameters are described in Table 18.

Simulation Parameter	Value / Condition
Simulation type	2D Transient, Axisymmetric
Material Data	
Viscosity	$\mu = 0.09t + 0.1\ Pa \cdot s$
Boundary conditions	
Inlet	Inflow, normal velocity = t + 1 m/s
Outlet	Outflow
Traction Boundary	Zero wall velocity
Axisymmetric Boundary	Symmetry

Table 18: Simulation Parameters for the study that validates a time-dependent viscosity model for a velocity that is increased linearly.

Building on the supporting calculations in Appendix B, the inlet pressure expression can be rewritten to include the time-dependent velocity.

$$\alpha = \frac{v_{max}(t) \cdot 16\mu(t)}{d^2} = -\frac{outlet\ pressure - inlet\ pressure}{0.035}\,. \tag{17}$$

The maximum velocity expression is simply the doubled inlet velocity expression. It is then possible to use this expression to compute the analytical solution for the inlet pressure, where both the velocity and the viscosity change over time. Figure 91 shows this analytical solution against the numerical solutions obtained using both solvers. The results show that Polyflow performs better and immediately converges onto the analytical solution. This is in contrast to the Fluent solution that has greater relative differences compared to the analytical solution seen in Figure 92.

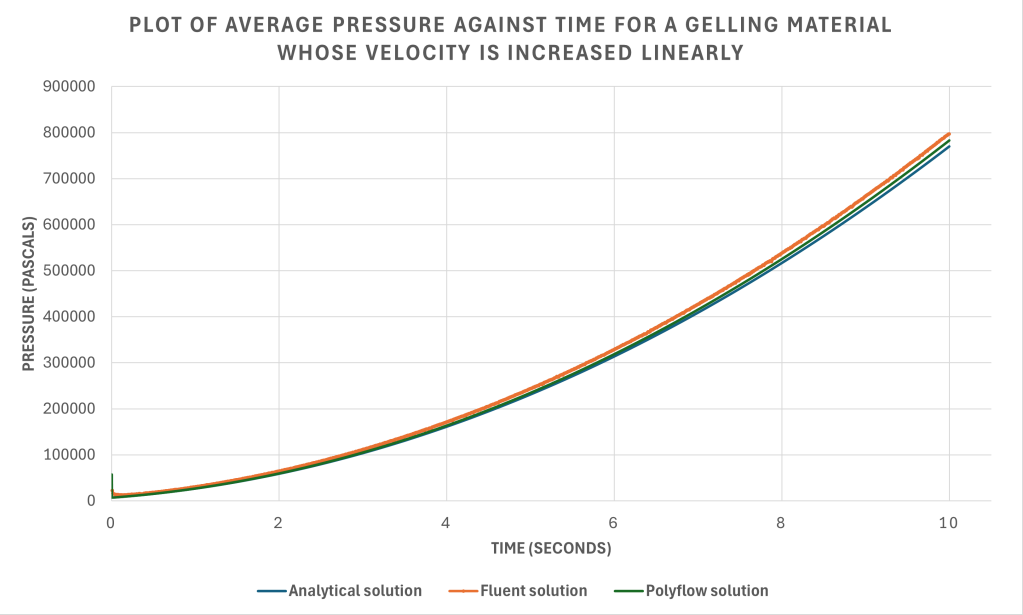

Figure 91: Plot of average pressure against time for a gelling material for analytical and numerical solutions. Here the velocity is increased linearly.

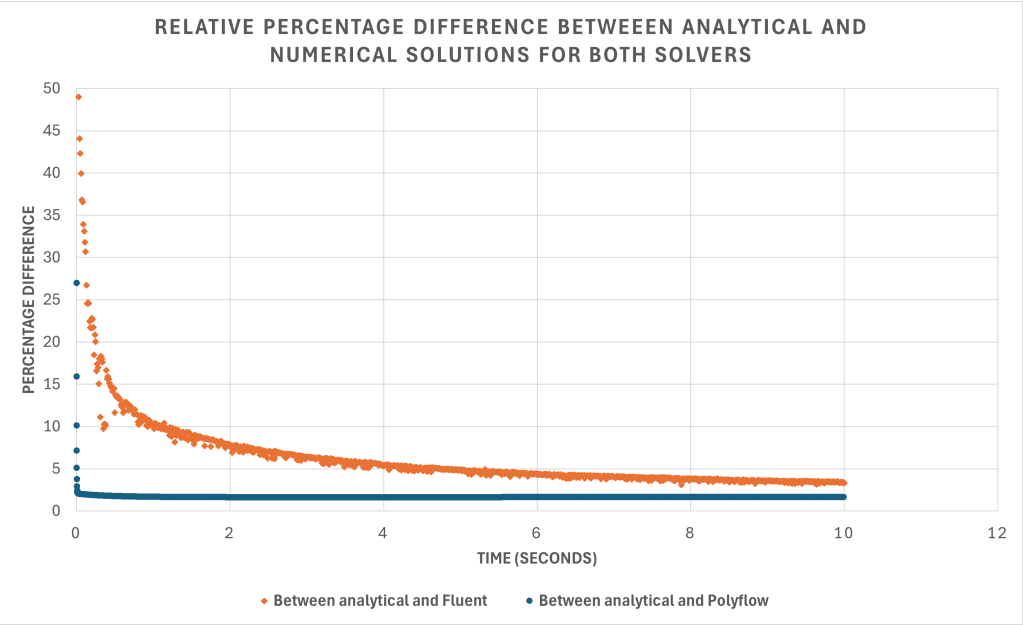

Figure 92: Relative differences between the analytical solution and each numerical solution. Here the inlet velocity increases linearly.

The analysis is further extended to test the performance of the solvers when a periodically varying velocity is implemented. The frequency of variation is chosen to match the frequency of the periodic boundary functions developed in Section 3.8. The analytical solution is computed using equation 14. The simulation parameters are detailed in Table 19.

Simulation Parameter	Value / Condition
Simulation type	2D Transient, Axisymmetric
Material Data	
Viscosity	$\mu = 0.09t + 0.1\ Pa \cdot s$
Boundary conditions	
Inlet	Inflow, normal velocity = cos(7t) + 1.1 m/s
Outlet	Outflow
Traction Boundary	Zero wall velocity
Axisymmetric Boundary	Symmetry

Table 19: Simulation Parameters for the study that validates a time-dependent viscosity for a velocity that is varied periodically.

Transient iterative parameters	Polyflow
Initial time	0 s
Final time	10 s
Initial value of timestep	0.001 s
Minimum value of the timestep	0.0001 s
Maximum value of the timestep	0.1 s
Transient iterative parameters	Fluent
Time step size	0.01 s
Number of time steps	1000

Table 20: Timestep settings for periodic velocity for both solvers for both cases

Figure 93 shows the numerical solutions plotted against the analytical solution. Again, Polyflow performs better and tracks the analytical solution more closely. In the simulations RV-POC-cons and RV-POC-ramp, the Fluent solution was quite close to the analytical solution. In this simulation, the Fluent solution tracks the analytical solution poorly, and this is further shown in Figure 94.

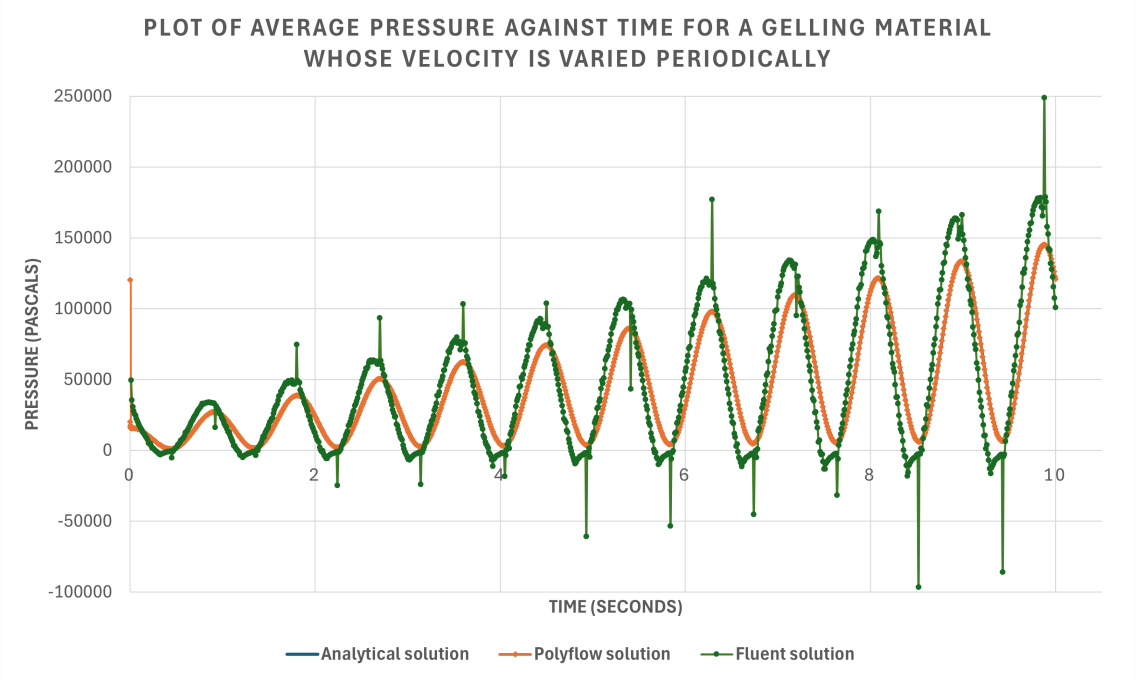

Figure 93: Plot of average pressure against time for a gelling material for analytical and numerical solutions. Here the velocity is varied periodically.

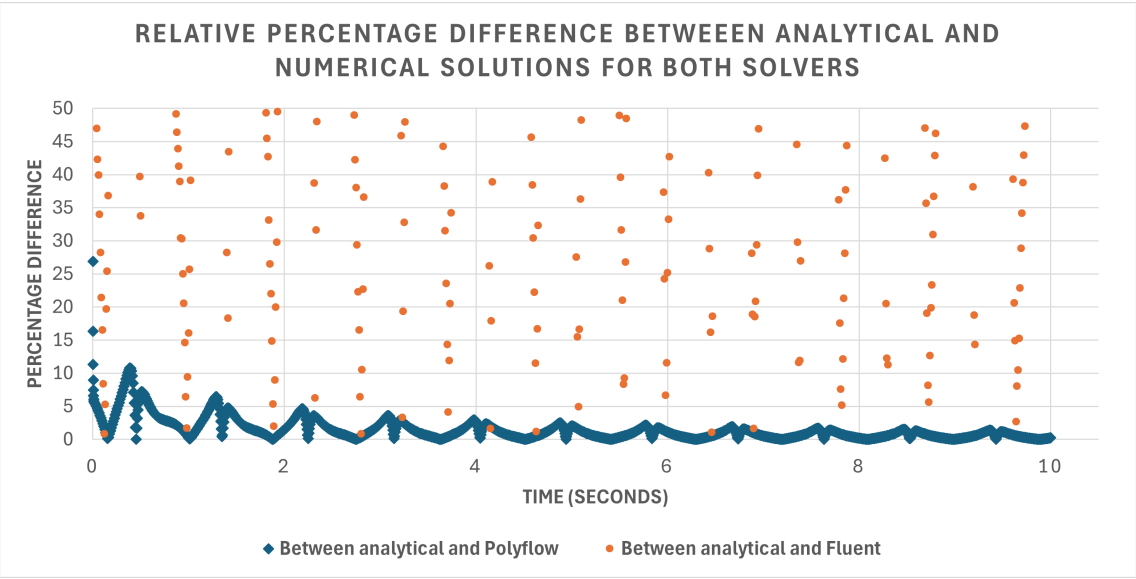

Figure 94: Relative differences between the analytical solution and each numerical solution. Here the inlet velocity varies periodically.

Appendix E

E Traction BC functions

UDFs implemented in Polyflow written in CLIPS language

E.1 Traction BC1

```
(deffunction UDF1 (?t)
  (/
     (+ 9228
        (* -1377.8 (cos (* 1 8.0652 ?t)))
        (* 8024 (sin (* 1 8.0652 ?t)))
        (* -2319.6 (cos (* 2 8.0652 ?t)))
        (* 1830.6 (sin (* 2 8.0652 ?t)))
        (* -1265.2 (cos (* 3 8.0652 ?t)))
        (* 594.3989 (sin (* 3 8.0652 ?t)))
        (* -800.718 (cos (* 4 8.0652 ?t)))
        (* 185.974 (sin (* 4 8.0652 ?t)))
        (* -501.9896 (cos (* 5 8.0652 ?t)))
        (* 25.9299 (sin (* 5 8.0652 ?t)))
        (* -322.6564 (cos (* 6 8.0652 ?t)))
        (* 4.9197 (sin (* 6 8.0652 ?t)))
     )
     42176
  )
)
```

E.2 Traction BC2

```
(deffunction UDF1 (?t)
  (* 14.59
     (+
        0.015
        (* -0.0059 (cos (* 1 8.0556 ?t)))
        (* 0.0017 (sin (* 1 8.0556 ?t)))
        (* -0.003 (cos (* 2 8.0556 ?t)))
        (* -0.009 (sin (* 2 8.0556 ?t)))
        (* 0.0053 (cos (* 3 8.0556 ?t)))
        (* 0.0034 (sin (* 3 8.0556 ?t)))
```

```
          (* -0.0032 (cos (* 4 8.0556 ?t)))
          (* 0.0013 (sin (* 4 8.0556 ?t)))
          (* 0.0006 (cos (* 5 8.0556 ?t)))
          (* -0.0028 (sin (* 5 8.0556 ?t)))
          (* 0.0014 (cos (* 6 8.0556 ?t)))
          (* 0.0014 (sin (* 6 8.0556 ?t)))
          (* -0.0021 (cos (* 7 8.0556 ?t)))
          (* 0.0015 (cos (* 8 8.0556 ?t)))
          (* -0.001 (sin (* 8 8.0556 ?t)))
      )
   )
)
```

E.3 Traction BC3

```
(deffunction UDF1 (?t)
  (/
    (+
      (abs
        (+
          (* 1.00662352 (sin (* 3.9077 ?t)))
          (* -0.64047203 (cos (* 3.9077 ?t)))
          (* 25.7673738 (sin (* 7.8154 ?t)))
          (* -2.0280963 (cos (* 7.8154 ?t)))
          (* -2.64238674 (sin (* 11.7231 ?t)))
          (* -1.50876297 (cos (* 11.7231 ?t)))
          (* -12.94073 (sin (* 15.6308 ?t)))
          (* -1.62404012 (cos (* 15.6308 ?t)))
          (* 2.10820415 (sin (* 19.5385 ?t)))
          (* -0.89681715 (cos (* 19.5385 ?t)))
          (* 2.56501428 (sin (* 23.4462 ?t)))
          (* 5.87561772 (cos (* 23.4462 ?t)))
          (* 1.30204564 (sin (* 27.3539 ?t)))
          (* -2.48099873 (cos (* 27.3539 ?t)))
          (* 5.01436064 (sin (* 31.2616 ?t)))
          (* -3.87018608 (cos (* 31.2616 ?t)))
        )
      )
      4
    )
```

```
26          99.76
27      )
28  )
```

Appendix F

F Traction boundary condition curve fitting

The curve fitting shown here is used to support the methodology described in Section 3.8.

F.1 Traction BC1

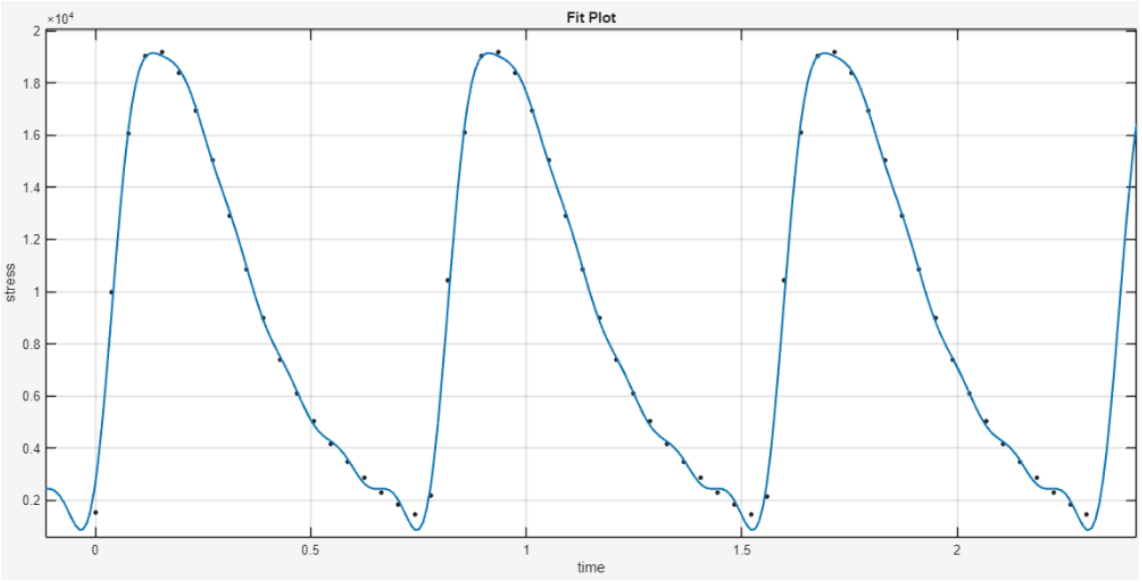

Figure 95: Curve fitting for traction BC1.

A 6-term fourier series is used and the R-sqaure value of the fit is 0.998. Equation 18 below shows the equation used for the fit.

$$\begin{aligned} f(t) = {} & 9228.0 - 1377.8\cos(8.0652t) + 8024.0\sin(8.0652t) \\ & - 2319.6\cos(2 \cdot 8.0652t) + 1830.6\sin(2 \cdot 8.0652t) \\ & - 1265.2\cos(3 \cdot 8.0652t) + 594.3989\sin(3 \cdot 8.0652t) \\ & - 800.7180\cos(4 \cdot 8.0652t) + 185.9740\sin(4 \cdot 8.0652t) \\ & - 501.9896\cos(5 \cdot 8.0652t) + 25.9299\sin(5 \cdot 8.0652t) \\ & - 322.6564\cos(6 \cdot 8.0652t) + 4.9197\sin(6 \cdot 8.0652t). \end{aligned} \tag{18}$$

F.2 Traction BC2

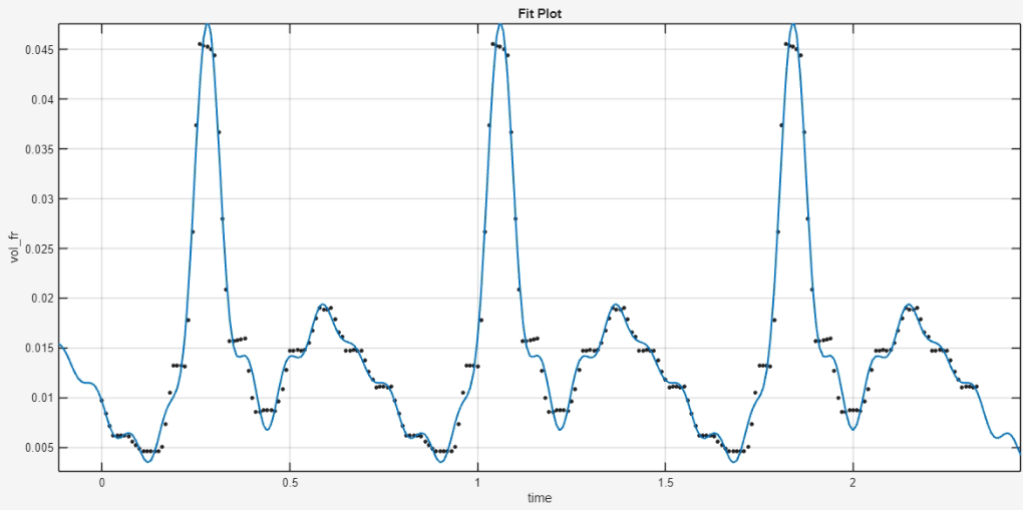

Figure 96: Curve fitting for traction BC2.

An 8-term fourier series is used and the R-sqaure value of the fit is 0.983. Equation 19 below shows the equation used for the fit.

$$\begin{aligned} f(t) = {} & 0.015 - 0.0059\cos(8.0556t) + 0.0017\sin(8.0556t) \\ & - 0.003\cos(2 \cdot 8.0556t) - 0.009\sin(2 \cdot 8.0556t) \\ & + 0.0053\cos(3 \cdot 8.0556t) + 0.0034\sin(3 \cdot 8.0556t) \\ & - 0.0032\cos(4 \cdot 8.0556t) + 0.0013\sin(4 \cdot 8.0556t) \\ & + 0.0006\cos(5 \cdot 8.0556t) - 0.0028\sin(5 \cdot 8.0556t) \\ & + 0.0014\cos(6 \cdot 8.0556t) + 0.0014\sin(6 \cdot 8.0556t) \\ & - 0.0021\cos(7 \cdot 8.0556t) \\ & + 0.0015\cos(8 \cdot 8.0556t) - 0.001\sin(8 \cdot 8.0556t). \end{aligned} \tag{19}$$

F.3 Traction BC3

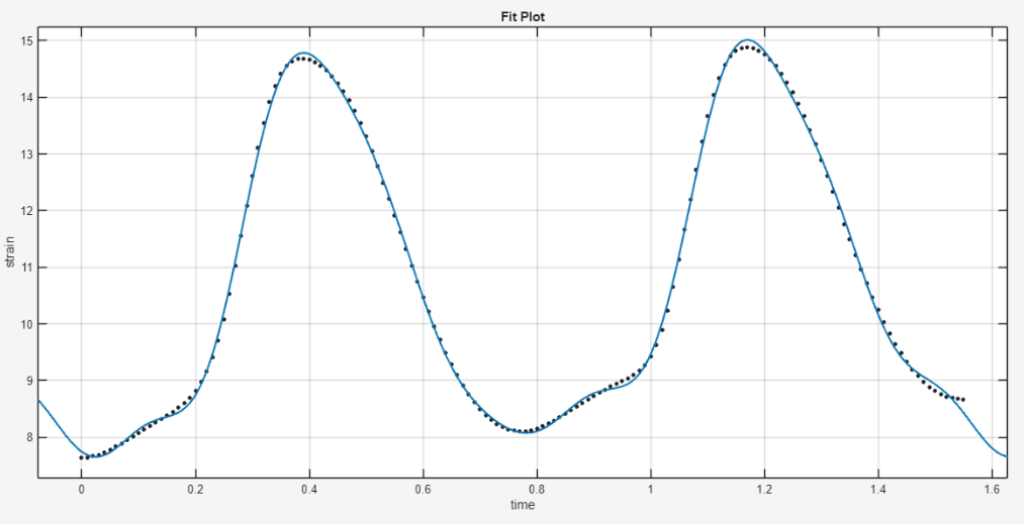

Figure 97: Curve fitting for traction BC3.

An 8-term fourier series is used and the R-sqaure value of the fit is 0.999. Equation 20 below shows the equation used for the fit. The derivative of this equation is used to model the traction BC.

$$\begin{aligned} f(t) = 10.6696 &- 0.2576\cos(3.9077t) - 0.1639\sin(3.9077t) \\ &- 3.297\cos(2\cdot 3.9077t) - 0.2595\sin(2\cdot 3.9077t) \\ &+ 0.2254\cos(3\cdot 3.9077t) - 0.1287\sin(3\cdot 3.9077t) \\ &+ 0.8279\cos(4\cdot 3.9077t) - 0.1039\sin(4\cdot 3.9077t) \\ &- 0.1079\cos(5\cdot 3.9077t) - 0.0459\sin(5\cdot 3.9077t) \\ &- 0.1094\cos(6\cdot 3.9077t) + 0.2506\sin(6\cdot 3.9077t) \\ &- 0.0476\cos(7\cdot 3.9077t) - 0.0907\sin(7\cdot 3.9077t) \\ &- 0.1604\cos(8\cdot 3.9077t) - 0.1238\sin(8\cdot 3.9077t). \end{aligned} \tag{20}$$

Appendix G

G Supplementary Analysis using the Grid Convergence Index

As multiple refinements are made, one may want to use a slightly courser mesh as it is refined sufficiently for the analysis. Therefore, it is essential to assess the error for the coarser grid. This is done using the Grid Convergence Index for a course grid [67] and is given as:

$$GCI_{coarse} = \frac{F_s \left|\epsilon\right| r^p}{r^p - 1}, \tag{21}$$

where F_s is the factor of safety, ϵ is the relative error between the course mesh and the fine mesh, r is the grid refinement ratio, and p is the order of convergence. The factor of safety is a conservative multiplier that accounts for uncertainties in grid independence studies. The value of F_s is set to 3 to ensure that the error estimates are reliable. This is especially important for a solution obtained using first-order methods, and using this value makes their error estimates appear larger. Furthermore, when using two meshes, the recommended F_s value is 3. The grid refinement ratio, r, is given as:

$$r = \frac{h_2}{h_1}, \tag{22}$$

where h_2 and h_1 are grid spacings for both meshes considered, with h_1 being the spacing for the finer mesh.

G.1 Grid Independence Study

The GCI is obtained using two meshes with the outlets being refined. The GCI_{coarse} is computed to justify using the courser mesh for the model. The meshes and their respective solutions can be seen in Table 21. It should be noted that these results were obtained using steady-state simulations. Therefore, convergence depends on the spatial discretization scheme. The meshes used are generated using linear elements and therefore, the order of convergence is set to 1.

Mesh count (refined) $\times 10^3$	**Element Size** (μm)	**Volumetric flow rate** $(\times 10^{-3} \frac{mm^3}{s})$
977	4.0	6.7967
2000	2.3	6.7728

Table 21: Grid independence study results taken from Table 15.

Using these values, the GCI value can be calculated as:

$$r = \frac{4}{2.3} = 1.739, \tag{23a}$$

$$|\epsilon| = \left| \frac{6.7728 - 6.7967}{6.7967} \right| = 3.516 \times 10^{-3}, \tag{23b}$$

$$GCI_{coarse} = \frac{3 \cdot 3.516 \times 10^{-3} \cdot 1.739}{1.739 - 1} = 0.0248. \tag{23c}$$

A GCI value of 2.5% indicates that the courser mesh in this case is reasonably refined and can be used for further analysis.

G.2 Time Step Independence Study

Adopting this method for the time-step independence study, a temporal convergence index can be defined. Here, r is the time-step refinement ratio. Table 22 are the values obtained using traction BC1 from Section 4.2.4. Since a variable time-stepping regime is used, the average time step size is obtained to calculate the value of r. These results are obtained using a transient simulation and therefore the convergence depends on the temporal discretization scheme. These solutions are obtained using the implicit Euler method for integration, which is 1st-order accurate.

Time Steps	**Average Time Step Size** $(\times 10^{-3} s)$	**Volume Lost** $(\times 10^{-4} mm^3)$
238	8.4346	3.85175
807	2.4814	3.85621

Table 22: Time step independence results for traction BC1 taken from Section 4.2.4.

Therefore, to justify using the courser time step setting, it is again essential to assess its error compared to the finer time-step solution. This is accomplished using the

same method as in Section G.1 above. The temporal convergence index (TCI) for a course time step size can be defined using the same formulation as in Equation 21. Using the values in Table 22, the TCI can be calculated as:

$$r = \frac{8.4346}{2.4814} = 3.399, \tag{24a}$$

$$|\epsilon| = \left| \frac{3.85621 - 3.85175}{3.85175} \right| = 1.1579 \times 10^{-3}, \tag{24b}$$

$$TCI_{coarse} = \frac{3 \cdot 1.1579 \times 10^{-3} \cdot 3.399}{3.399 - 1} = 0.00492. \tag{24c}$$

A value of 0.49% for the convergence index indicates good convergence and justifies using the courser time-step setting. Looking at the time-step independence results of traction BC2 and BC3, the trend continues. Therefore, it can be reasonably inferred that their respective convergence index values will also fall within a similar range.

Appendix H

H Validation studies

H.1 Investigation of the fluid domain during the cardiac cycle (3D-card-cycl)

Earlier in Section 3.7, it is outlined that the model is simplified to a rigid CFD model so that it can be used in Polyflow with an appropriate traction boundary. This simplification is justified by performing an analysis of the fluid domain using the original results of the FSI model. The analysis aims to demonstrate that the fluid domain does not change significantly during the cardiac cycle. The data is available in discrete DAT files for each time step during the entire simulation. Four points are chosen for the analysis: peak diastole, mid-systole, peak systole, and mid-diastole.

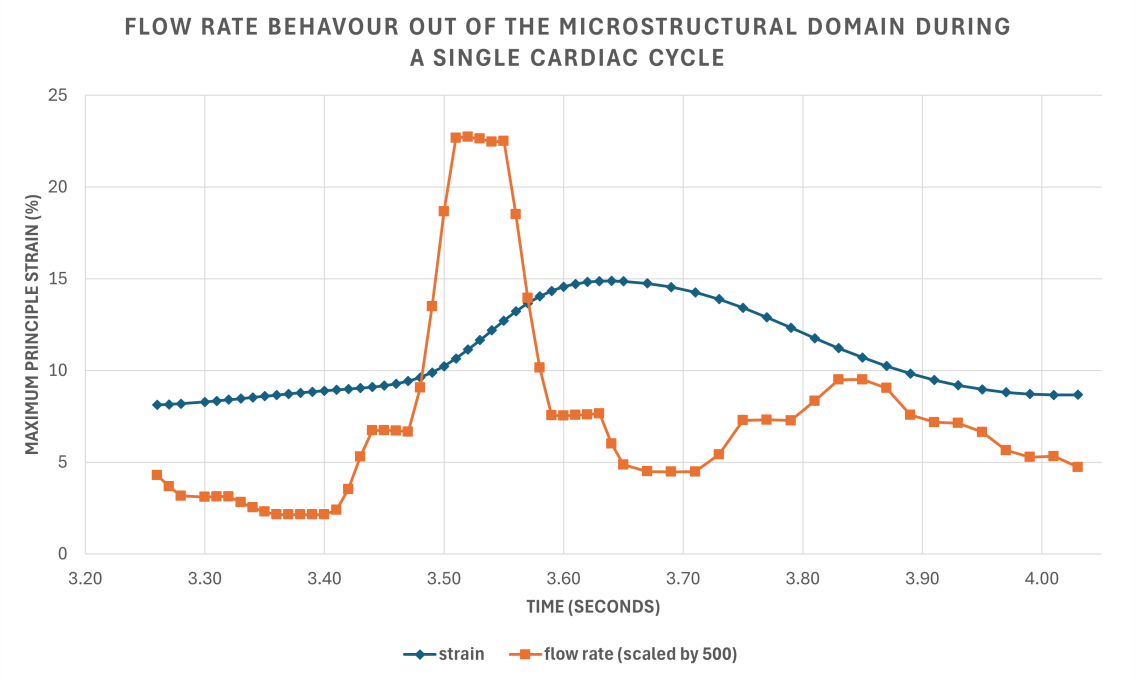

Figure 98: Visual comparison of the flow rate of PEG with the strain response of the tissue block. The flow rate response is scaled for visual purposes.

The peak values can be chosen simply by selecting the DAT files for the times when the strain is at its maximum and minimum. The midpoints are chosen based on a different logic, rather than selecting the time halfway between systole and diastole.

The logic is explained in conjunction with Figure 98 above. It shows the variation in the total flow rate of PEG along with the variation in strain during a cardiac cycle. The midpoints are selected when the flow rate peaks between systole and diastole and vice versa. It is assumed that the greatest deformation of the fluid domain occurs when the flow rate peaks. This can then be compared with the domain at peak diastole to note any differences. The times selected from the FSI results are as follows: 3.26 s, 3.52 s, 3.64 s, and 3.85 s for diastole, mid-systole, systole, and mid-diastole, respectively. The DAT files related to these are then chosen and analysed.

Initially, these DAT files are analysed using CFD Post to visually compare the differences in domain shape and orientation. Figure 99 illustrates the variation in the fluid domain during different stages of the cardiac cycle. Visually, there are no significant differences in the shape and orientation of the domains. A quantitative analysis examines parameters influencing traction BC application and flow rate behaviour. In this context, the relevant parameters include the areas of the distinct regions within the fluid domain.

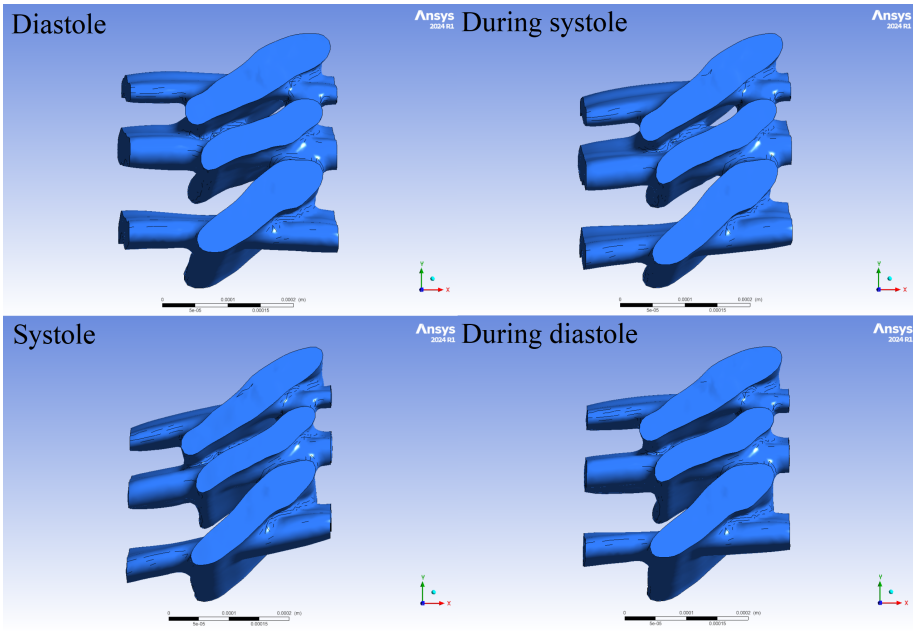

Figure 99: Visualization of the changing shape of the fluid domain during the cardiac cycle. The changes can be noticed easily in two locations. The left-most outlets can be seen to change orientation. The center outlet in the front-facing outlets can be seen to change shape.

When traction is applied, the outer surface area where the traction is applied influ-

ences the flow rate. The outlet area also influences the flow behaviour, affecting the flow rate. The areas for each outlet and the outer surface are calculated for the fluid domain in each phase of the cardiac cycle. These values are presented in Table 23.

	Point during cardiac cycle				
Boundary	**Diastole**	**During systole**	**Systole**	**During diastole**	**Final mesh**
Outer surface	0.771	0.793	0.819	0.789	0.856
$Z_{positive}$	0.0341	0.0339	0.0348	0.0345	0.0348
$Z_{negative}$	0.0360	0.0345	0.0346	0.0356	0.0348
$X_{positive}$	0.0299	0.0298	0.0286	0.0292	0.0272
$X_{negative}$	0.0297	0.0305	0.0294	0.0293	0.0272

Table 23: Respective areas of all relevant boundaries during the cardiac cycle. The areas are in mm^2. The relevant parameters for the final mesh used in this project are also included for further discussion.

The relative differences for each parameter are calculated with respect to the values recorded during diastole. These differences are presented in Table 24, which indicates that the areas exhibit minimal variation throughout the cardiac cycle. This provides the justification for assuming that the relevant areas are constant during the cardiac cycle, allowing one to make a rigid CFD assumption for the model.

	Relative percentage difference			
Boundary	**Diastole**	**During systole**	**Systole**	**During diastole**
Outer surface	0	2.77	5.86	2.28
$Z_{positive}$	0	0.590	2.01	1.16
$Z_{negative}$	0	4.35	4.05	3.45
$X_{positive}$	0	0.336	4.55	2.40
$X_{negative}$	0	2.62	1.02	1.37

Table 24: Relative percentage differences of the areas when compared with the areas taken at diastole.

An important distinction must be made with respect to the areas accounted for during the cardiac cycle compared to the mesh generated for this study. Table 23 also presents the parameters obtained using the 977 $\times 10^3$ element mesh. In contrast,

the mesh used in the FSI simulation has around 70,000 elements. The differences in areas can be attributed to the surface approximation that occurs when refining a mesh. A finer mesh uses more elements to closely approximate the shape of a geometry. This approach allows the mesh to capture details that a coarser mesh would otherwise smooth over.

Building on the findings that boundary areas remain largely unchanged during the cardiac cycle, the focus shifts to analysing the domain's overall shape. Figure 99 also illustrates that the shape of the domain varies slightly throughout the cardiac cycle. This variation may influence the manner in which applied traction affects flow behaviour. To investigate this, the meshes from the DAT files are extracted and used in Polyflow. This process involves using Fluent Mesher to read a case file, after which the mesh can be exported. This was performed for the relevant case files associated with the aforementioned time steps.

The meshes are subsequently used with Polyflow to conduct a type of parametric study. In this analysis, a constant traction is applied to the boundary, while the variable parameter is the domain shape during different stages of the cardiac cycle. Output parameters for the analysis include the average velocities at each outlet and the total flow rate exiting the domain. The final mesh, comprising 977 $\times 10^3$ elements, is also incorporated in the analysis. The results are presented in Section H.2.

H.2 Rigid CFD results

The results presented in this section are related to the analysis conducted in Section H.1. Table 25 summarises the total flow rate and the average velocity results throughout the cardiac cycle for each mesh. Table 26 summarises the relative differences for each parameter compared to the values recorded during diastole.

	Point during cardiac cycle				
Parameter	**Diastole**	**During systole**	**Systole**	**During diastole**	**Final mesh**
Total flow rate $\times 10^{-4} \frac{mm^3}{s}$	3.61	3.39	3.19	3.41	4.76
$Z_{positive}$ average velocity $\frac{mm^2}{s}$	3.39	3.18	3.01	3.25	4.45
$Z_{negative}$ average velocity $\frac{mm^2}{s}$	3.43	3.21	2.91	3.18	4.46
$X_{positive}$ average velocity $\frac{mm^2}{s}$	2.03	1.95	1.88	1.94	3.00
$X_{negative}$ average velocity $\frac{mm^2}{s}$	2.04	2.04	2.04	2.02	3.08

Table 25: Flow rate and average velocity results during the cardiac cycle (final mesh included for further discussion).

	Relative percentage difference			
Parameter	**Diastole**	**During systole**	**Systole**	**During diastole**
Total flow rate $\times 10^{-4} \frac{mm^3}{s}$	0	6.49	13.16	5.87
$Z_{positive}$ average velocity $\frac{mm^2}{s}$	0	6.60	12.6	4.31
$Z_{negative}$ average velocity $\frac{mm^2}{s}$	0	6.85	17.9	7.86
$X_{positive}$ average velocity $\frac{mm^2}{s}$	0	4.10	7.98	4.64
$X_{negative}$ average velocity $\frac{mm^2}{s}$	0	0	0	0.990

Table 26: Relative differences between average velocity and flow rate when compared with the values taken at diastole.

Table 26 demonstrates greater variability in the parameters throughout the cardiac cycle compared to the analysis focusing on the areas. These results exhibited significant variations compared to those derived from the final mesh, as indicated above in Table 24. This discrepancy can be attributed to the surface approximation that

occurs during mesh refinement. This study highlights the importance of accurately accounting for the domain shape at all stages. While accounting for shape changes is important, accurately capturing fluid behaviour was the primary goal of this work. Incorporating myocardial motion and the corresponding volume changes will be the subject of future work.

To validate the rigid CFD model approximation, the modelling approach has been suitably developed. The objective of this project is to quantify the overall losses during the gelation process. Consequently, it is crucial to accurately match the total volume loss per cycle across multiple cycles. The boundary conditions developed in Section 3.8 have been suitably optimised. For a mesh utilised with the traction boundary condition, the total volume lost per cycle aligns with the FSI results. This supports the rationale for disregarding changes in domain shape throughout the cardiac cycle.

H.3 Constant viscosity assumption (Gel-const-visc)

Earlier in Section 3.7, it is stated that the time interval for the overall analysis ranges from 0 to 417 s. This represents a relatively large time domain to simulate computationally. Simulating the gelling process in Polyflow typically takes around 4 to 5 hours for each second of gelation time. At this rate, simulating 417 s of gelation would require roughly 2085 hours (87 days) of continuous run time using a single solver. Although the run time can be reduced using the analysis conducted later in Section H.5, it remains computationally expensive. Additionally, it is important to consider that multiple case studies of gelation require simulation. Therefore, identifying effective strategies for reducing computational expense is of interest.

This can be achieved by simulating gelation exclusively during a phase with more dynamic viscosity changes. Initially, during the gelation process, the viscosity remains fairly constant, as shown in Figure 52. During this stage, the viscosity is in a pseudo-steady state, increasing more slowly than in later gelation stages. Therefore, one may simulate a single cycle within the pseudo-steady state region and extrapolate that result to approximate multiple cycles. This approach significantly reduces the simulation time frame and decreases computational expense.

In Figure 52, the viscosity appears constant during the initial 250 s based on visual inspection. To substantiate the assumption of constant viscosity, a quantitative analysis is conducted. This analysis compares the volume lost during a single cardiac cycle across different regions within the first 250 s. The analysis is done specifically using BC2. Entering start and end times with multiple significant figures for the traction BC functions proves challenging for accurately capturing a single cycle. Traction BC2 exhibits a distinct peak between two minima during each cycle, as

illustrated in Figure 100. Thus, rather than defining each cycle precisely, a rough 1-second interval containing the peak is used. The area under this peak is calculated and used as a metric to compare different regions where the viscosity is assumed to be constant. The results are presented in Section H.4.

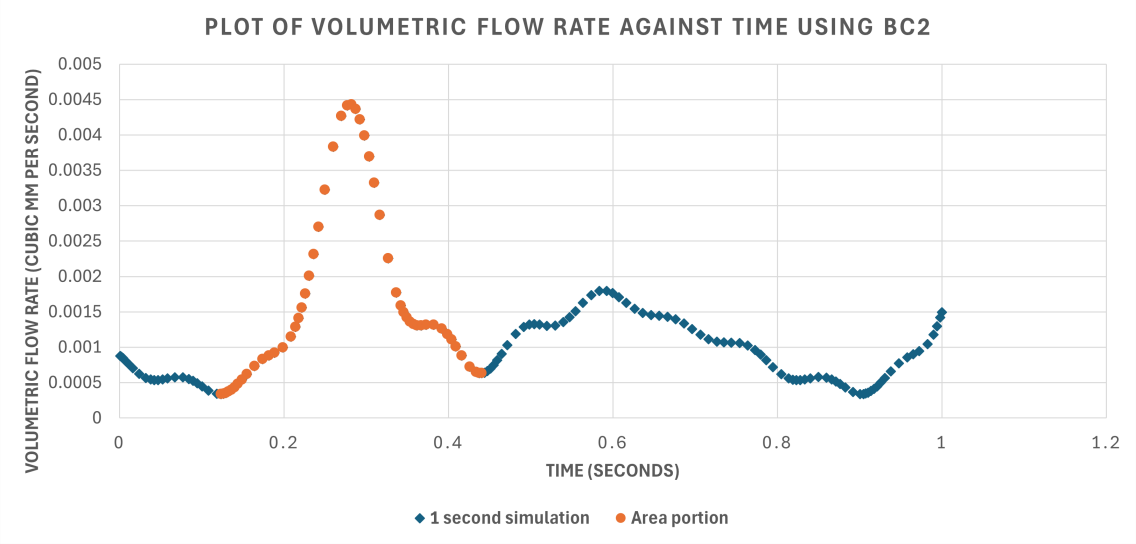

Figure 100: Plot of flow rate over time using traction BC2 with the distinctive peak highlighted. The area under this peak is used as the measure for the analysis.

H.4 Constant viscosity assumption results

The results in this section are related to the analysis conducted in Section H.3. Table 27 presents the volumes obtained during various one-second simulations. The volumes are obtained by computing the area under the curve for the region discussed in Figure 100 earlier. Relative differences are computed relative to the volume calculated in the first second from 0-1 s. The preliminary analysis revealed that during the initial 190 s, the volume differences remained within 1%. Therefore, the viscosity can be considered constant for this interval, using the viscosity at t=0. However, as depicted in Figure 52, it is evident that even after 190 s, there exists a region where the viscosity can be kept constant.

Time interval *seconds*	**Volume** $\times 10^{-4} mm^3$	**Relative difference** %
0-1	5.72	0
50.5-51.5	5.73	0.18
100.5-101.5	5.73	0.16
150.5-151.5	5.71	0.12
180-181	5.69	0.45
190-191	5.67	0.86
200.4-201.4	5.65	1.3

Table 27: Results of the analysis which shows the time domains simulated, the area under the distinctive peak representing volume, and the relative difference between the volumes when compared to the first cycle.

Time interval *seconds*	**Volume** $\times 10^{-4} mm^3$	**Relative difference** %
190-191	5.67	0
200.4-201.4	5.65	0.41
210.4-211.4	5.64	0.49
220.5-221.5	5.60	1.2
230.5-231.5	5.57	1.7

Table 28: Similar results to Table 27 with different regions analysed. Here, the relative differences are calculated with respect to the volume obtained from 190-191 s.

To this end, a subsequent analysis investigates the volumes and their relative differences over a time beyond 190 s. Table 28 presents the volumes and relative differences for one-second simulations conducted up to an upper limit of 230 s. The subsequent analysis demonstrates that the viscosity can be held constant from 190 to 220 s. Thus, the viscosity at t = 190 s can be used in this interval. Further analysis reveals that volumes exhibit significant variation within shorter ranges. Consequently, the decision was made to maintain the viscosity constant for only two time intervals: 0-190 s and 190-220 s. There are 245 cycles within the range 0-190 s and 40 cycles within the range 190-220 s. A single cycle can be simulated within each range and multiplied by the number of complete cycles to determine the total volume lost in that region.

From 220 s onwards, the gelation process is simulated rather than approximated. This approach significantly reduces computational expense. Using the previously

outlined measurement, the simulation time decreases from 417 s to 197 s. With this reduction, the solver still requires 41 days of continuous run time to simulate the rest of gelation. Although the time is halved, this duration remains impractical to obtain a single result.

H.5 Strategy for simulating a large time domain (Gel-splt-domn)

The analysis presented in this section outlines a method for minimising the time required to obtain results from a large time-domain simulation. However, this approach requires a corresponding increase in computational resources. The method uses multiple cores to run several solvers simultaneously instead of using all cores for one solver. The analysis in Appendix I details the run times for various solver configurations. It was determined that **four** cores were the optimal number of cores to use when running the model. This configuration varies depending on the machine utilised to solve the problem. In the case of a standard 8-core PC, it is beneficial to run four solvers with two cores each. This is preferable to using two solvers with four cores each or a single solver using all eight cores.

The advantage of using multiple solvers lies in the ability to divide the time domain for simulation among multiple solvers. These simulations can be run simultaneously and combined to reconstruct the original time-domain solution. Although assigning fewer cores to a solver results in a slight decline in performance, executing multiple solvers leads to an overall improvement. This depends on the nature of the solution that is being generated. If a solver takes considerable time to reach the final solution, it may be inefficient to use many shorter simulations. In the case of the current model, the analysis conducted in Section 3.6.5 indicates that it converges onto an analytical solution almost instantaneously. Therefore, this method of using multiple solvers can be used to quickly obtain results. An investigation is performed to analyse the accuracy of such a solution.

To start with, a single simulation is run from 400 to 404 s. Subsequently, two sets of simulations are conducted. One simulation runs from 400 to 402 s, and another runs from 401.9 to 404 s. The specific time frame is chosen because the viscosity change is more pronounced during this period. This transient viscosity change may place greater demands on the solver to achieve convergence compared to other intervals where the viscosity change is minimal. The reason for increasing the second domain by 0.1 s is to allow the solver to comfortably converge onto the final solution. Once the solver achieves convergence, the solution is extracted from the 402 to 404 s interval and merged with the solution of 400 to 402 s. These solutions can then be compared, and the results are presented in Section H.6.

H.6 Supporting results for simulating a large time domain

The results presented in this section are related to the analysis conducted in Section H.5. The findings indicate a close match between the complete solution and the combined solution. Figure 101 visually illustrates the convergence of the two solutions.

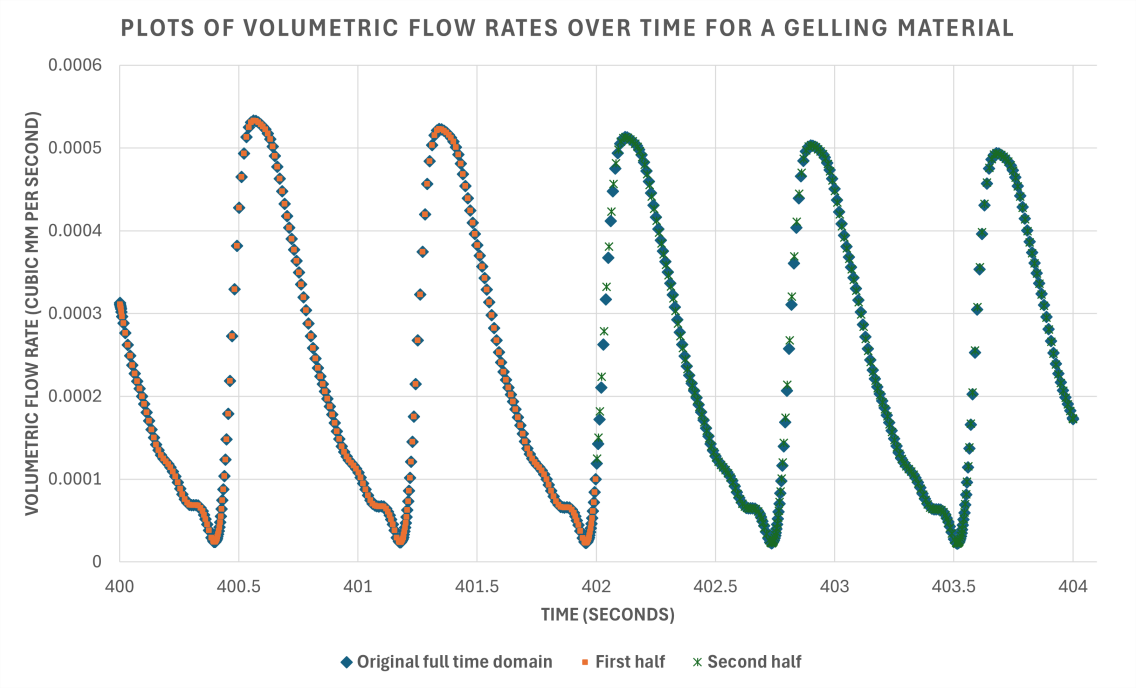

Figure 101: Plot of flow rate against time for a solution that is run using one solver and for another solution that is run using two solvers.

To further assess the accuracy of the solutions, the area under the graph was computed for both solutions. The area under the original solution and the combined solution yields volumes of 9.88 $\times 10^{-4} mm^3$ and 9.88 $\times 10^{-4} mm^3$, respectively. This result is accurate to three significant figures. However, when more significant figures were used and the solutions were compared, the combined solution was within 0.03% of the original solution. This provides a justification for partitioning the time domain into smaller intervals and using multiple solvers simultaneously to solve each smaller time domain.

Using this method, the time required to achieve a complete solution for the simulation can be significantly reduced. The available hardware is configured with 40 compute cores, enabling the operation of 10 solvers, each assigned 4 cores. Thus, the run time is reduced from 41 days of continuous operation on a single solver to 4 days

of continuous operation using 10 solvers. This reduction in wait time for simulation results is deemed satisfactory, and this strategy can be used to investigate multiple cases of gelation.

H.7 Solver convergence over multiple cycles during gelation (Gel-solv-convg, 3D-solv-convg)

The previous analysis in Section H.3 uses the fact that the solver immediately converges onto a solution. This immediate convergence provides the basis for breaking it into smaller sections and putting the results together. Another aspect to consider is the convergence of the solution produced by the solver during rapid fluctuations in traction. With consistently varying traction, the observed flow rate decreases as viscosity increases. While the solver generates a solution, it is essential to determine if the reduction in flow rate is solely caused by a change in viscosity and not influenced by the time the solver takes to reach convergence.

The extended validation study in Appendix D highlights an important result which provides the basis for conducting this current analysis. Figure 94 illustrates the relative difference between an analytical solution and a numerical solution that is generated using a periodic input boundary condition. Looking at the performance of the solver, it can be seen that the relative difference takes some time to decrease compared to the other validation studies in Appendix D and Section 3.6.5. To investigate this, a single simulation is run with gelation over an extended period during which the viscosity changes rapidly. Subsequently, two simulations with constant viscosity were performed, using times closer to the upper and lower bounds of the preceding simulation. Flow rates can then be compared at specific points within the extended simulation. The constant viscosities used are chosen using the gelling model and the times at 400 s and 410 s. The rationale for choosing the times used to calculate constant viscosities is explained as follows. After the extended gelling simulation is run, two maximums for the flow rate are chosen closer to the start and end times. The times when these maxima occur are noted and used to calculate the constant viscosity at that time. These values are used to determine the flow rate without gelation, enabling a direct comparison of flow rates. The results are detailed in Section H.8.

H.8 Solver convergence for gelation results

The results presented in this section are related to the analysis conducted in Section H.7. Figure 102 illustrates the convergence between solutions.

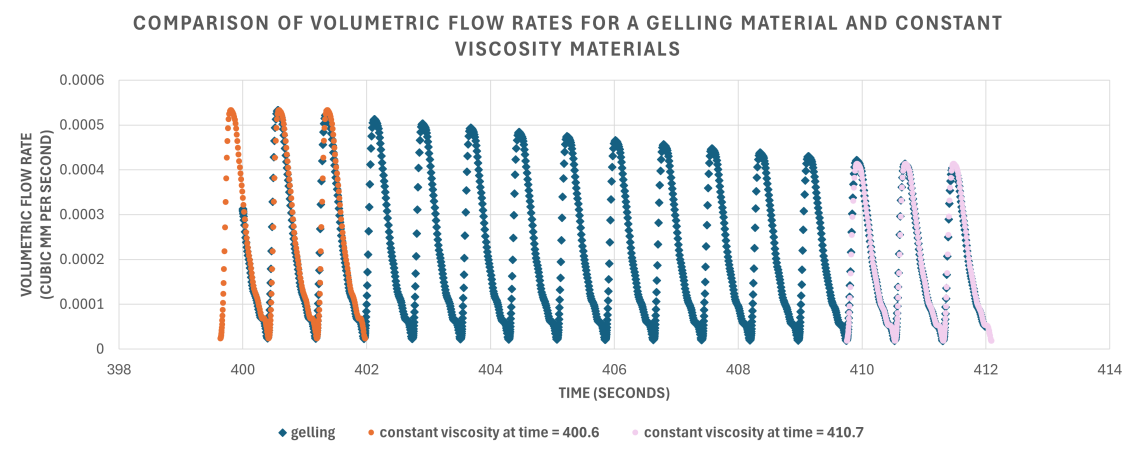

Figure 102: Plot of flow rates over time for all three studies conducted. The constant viscosity study results are shifted in the x-axis to visually compare the different results.

To further evaluate the accuracy of the extended gelling simulation, the flow rate peaks were compared. At times 400.6 and 410.7 s, the extended simulation had flow rates of 5.33 $\times 10^{-4} mm^3$ and 4.13 $\times 10^{-4} mm^3$, respectively. For viscosity at time 400.6 s, the flow rate peaked at 5.33 $\times 10^{-4} mm^3$. For viscosity at time 410.7 s, the flow rate peaked at 4.13 $\times 10^{-4} mm^3$. These results are presented with three significant figures; however, when additional figures were included, the results remained within 1% of each other. This result proves that the drop in flow rate is solely due to the change in viscosity.

Appendix I

I Solver performance (Gel-solve-perfm)

Table 29 details the simulation parameters used to measure the computational performance for different instances.The first instance measures solution time for the final 3D mesh with 977 $\times 10^3$ elements, varying solver core setups. In the second instance, it measures solution time for different meshes using a 4-core solver setup.

Simulation Parameter	Value / Condition
Simulation type	3D Transient
Material Data	
Viscosity	**gelation model**
Boundary conditions	
$Z_{negative}, Z_{positive}$ $X_{positive}, X_{negative}$	outflow
Outer surface	Normal traction and tangential velocity $f_n = \mathbf{BC1}$ $v_s = 0\,\mathrm{m/s}$
Transient iterative parameters	
Initial time	415
Final time	416
Initial value of timestep	0.001
Minimum value of the timestep	0.001
Maximum value of the timestep	0.01

Table 29: Simulation Parameters for the study that investigates solver performance.

The run times are highlighted for a workstation and the UCT HPC system. The workstation features an AMD Ryzen 7 2700X Eight-Core processor operating at a base clock speed of 3.70 GHz with 64GB of RAM. Table 30 and Table 31 detail the number of cores used for the solver and the resulting time taken to obtain a solution for the workstation and HPC, respectively. Table 32 details the run times for the same simulation performed on a 4-core setup of the HPC system. Meshes with increasing refinement are used, and their respective run times are recorded.

Cores used	Run time (hours)
1	10.0
2	7.11
4	5.53
8	5.27

Table 30: Run times using a workstation with increasing number of cores used for the setup.

Cores used	Run time (hours)
1	8.57
2	5.29
4	3.66
8	3.31

Table 31: Run times using the HPC with increasing number of cores used for the setup.

Mesh count	Run time (hours)
626,000	2.22
819,000	3.05
977,000	3.67
1,200,000	4.49
2,000,000	7.90

Table 32: Run times using the HPC with increasingly refined meshes with a 4-core setup.

Appendix J

J Instability in BC3 flow rate solution

When computing the volume lost per cycle in the analysis done in Section 4.3.1, there is an instability in the solution shown graphically in Figure 78. The volume lost per cycle using BC3 shows rapid fluctuations per cycle. Further investigating the flow rate behaviour shows that it varies slightly per cycle. This can be highlighted in Figure 103, which shows the flow rate behaviour slightly changing per cycle. This can be attributed to the fact that BC3 is derived from the strain gradient. A function is fitted to the strain response, and its derivative is used to model the traction BC. This contrasts with the other two BCs, which use their functions after curve fitting and linear scaling, without any differentiation.

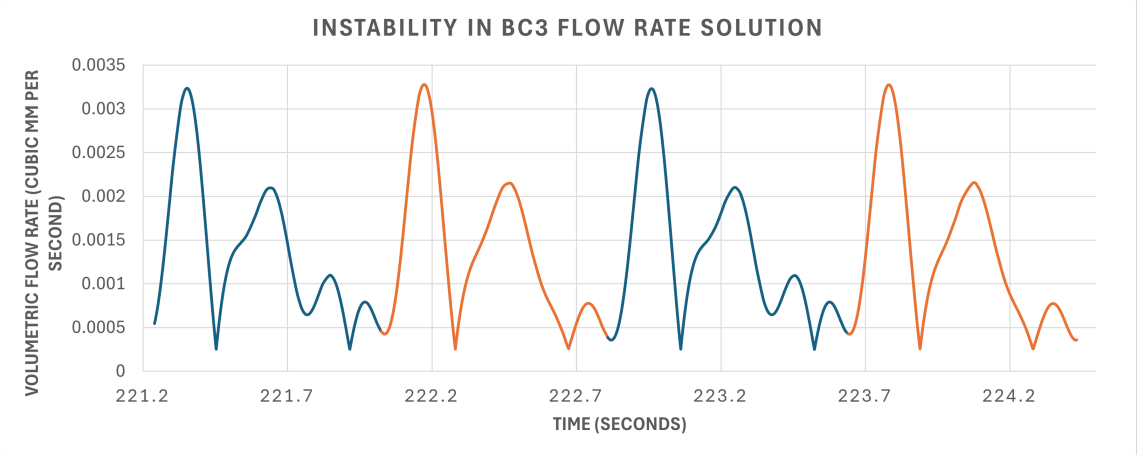

Figure 103: Plot of volumetric flow rate against time using BC3. Each cardiac cycle is highlighted in a different colour.

Figure 103 shows how the flow rate behaviour changes every cycle, with the same pattern repeating over time. When the flow rate solution is used to compute the volume lost per cycle, this results in slight variations in the volumes.

Appendix K

K Simplified 3D geometry

The following geometry is developed in Design Modeller for use in the case study described in Section 3.10.2. It is designed on a scale similar to the 3D microstructural domain described in Section 3.3.2. It has a length of 3.5 $\times 10^{-4}$ m and a diameter of 1.5 $\times 10^{-4}$ m. The length and diameter are chosen to match the dimensions of the microstructural domain. The diameter is selected to correspond with the hydraulic diameter of one of the faces of the microstructural domain.

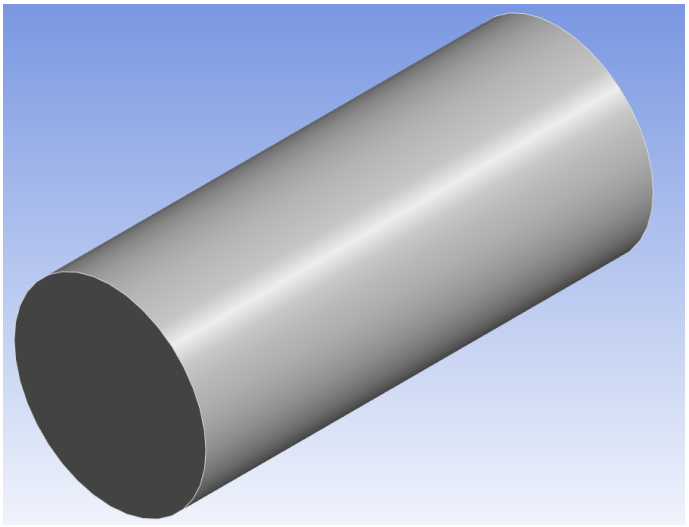

Figure 104: Simple 3D microstructural domain developed for the second case study.

The meshing is done in Ansys Meshing. The meshing strategy follows the methodology outlined in Section 3.6.1 and Section 3.9.1, where the outlets are refined more than the rest of the domain. The mesh refinement utility is used in Meshing with a refinement level of 1 specified on the outlets. An arbitrary traction is specified on the outer surface of the domain and the total flow rate is observed. The mesh is successively refined until the flow rate converges and this final mesh can be seen in Figure 105.

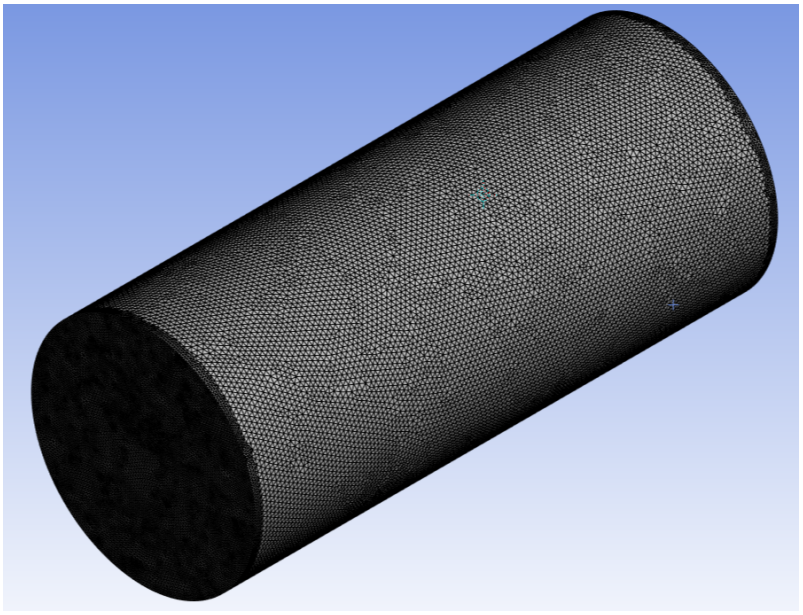

Figure 105: Final mesh of the simple geometry showing the finely refined outlets.

The final statistics of the mesh are as follows:

- Element size of 3 μm
- 934768 elements

The number of elements of this mesh is close to the mesh used for the original microstructural domain.

Appendix L

L Curve fitting for the volume lost per cycle behaviour

The curve fitting shown here is used to support the discussion in Section 4.3.1, where a curve is fit to the plot of the volume lost per cycle.

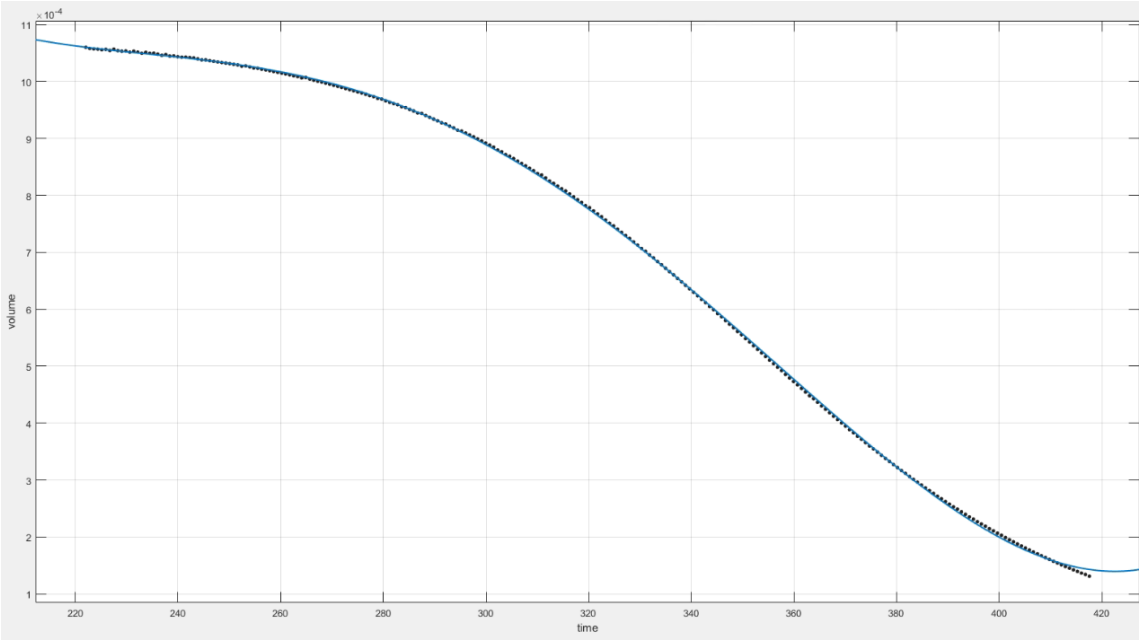

Figure 106: Curve fitting for the volume lost per cycle behaviour.

A 4th order polynomial is used and the R-square value of the fit is 0.99. Equation 25 below shows the equation used for the fit.

$$f(t) = 1.9441 \times 10^{-5} \cdot t^4 + 3.3268 \times 10^{-5} \cdot t^3 - 1.1684 \times 10^{-4} \cdot t^2 - 3.6496 \times 10^{-4} \cdot t^1 + 7.7716 \times 10^{-4}. \quad (25)$$

Where t is normalised by mean 319.5 and std 56.7.